High Strain Rate Characterisation of Composite Materials

Eriksen, Rasmus Normann Wilken

Publication date:
2014

Document Version
Publisher's PDF, also known as Version of record

High Strain Rate characterisation of Composite materials

PhD Thesis

$$(EIv'')'' = q - \rho A\ddot{v}$$

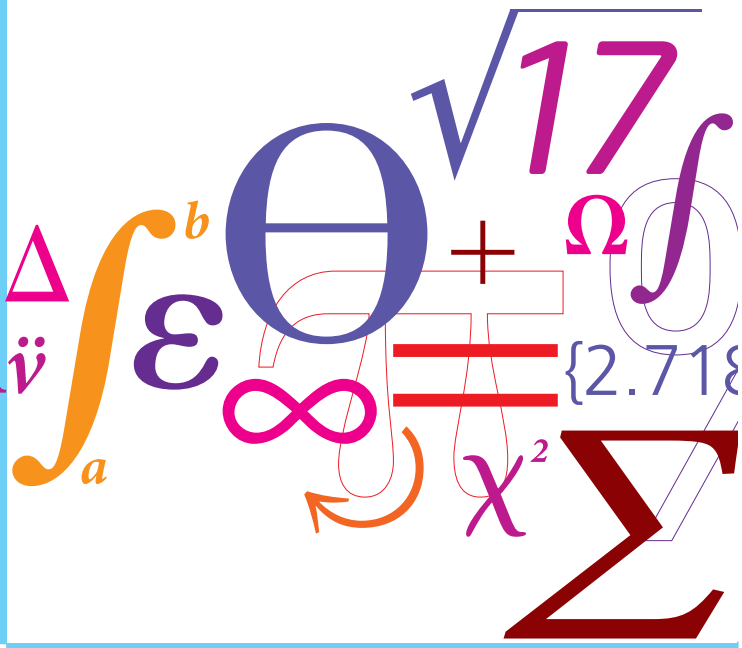

Rasmus Normann Wilken Eriksen
DCAMM Special Report No. S179
March 2014

DTU Mechanical Engineering
Department of Mechanical Engineering

High Strain Rate characterisation of Composite materials

Rasmus Normann Wilken Eriksen 31/03/2014

Table of contents

Preface

This thesis is submitted as a partial fulfilment of the requirements for the Danish Ph.D. degree. The work was performed in the Structural Light Weights Group, Department of Mechanical Engineering, Technical University of Denmark, during the period of August 2010 to March 2014. The project was supervised by Associate Professor Christian Berggreen and co-supervised by Professor Janice Barton, University of Southampton, and Senior Researcher Helmuth Toftegaard, DTU Wind energy.

The study was part of an overall project, RESIST, which involved the participation of the Danish Army, Falck Schmidt Defence Systems, COMFIL® and DTU Wind Energy. The RESIST project encompassed another Ph.D. concerning blast testing and simulation of fibre reinforced polymer composite panels. Test data obtained throughout this work was used as input data for the simulation of the composite panels.

Acknowledgement

I would like to thank my Co-Supervisor Professor Janice Barton for hosting me at her university during my external stay and for her motivating inputs. I would also like to thank my Co-Supervisor Helmuth Toftegaard for many fruitful discussions and his help of organising test specimens at the DTU Wind energy fibre lab. In addition, a great thanks to the skilled technician at the DTU Wind energy fibre lab who produced all the test specimens with great care through the project.
There is a *very* special thanks to Robert Swan, technician in building 119. Without him, it would have been impossible to construct a complete test machine and install it in the lab! The same hold for Jonathan Schwartz for his extraordinary time investment in designing and installing the pump that pressurised the test machine. There is also a special thanks to all the skilled technician in the workshop in building 119, building 413, and building 427, who made this very heavy experimental project possible!
… And my very good friend and colleague Søren Giversen needs a special thanks for his endless support, funny moment and fruitful inputs!
Special thanks to my supervisor Christian Berggreen who supported me through the hard times of the project and encouraged me go on. A special thanks to Stina Jensen for her support and time through the first part of the project.

…And of course the girlfriend! – Thanks to my lovely girlfriend Josefine for her patience – always understanding when I was working in the night times, in the evenings, and when a good idea pop up and I disappeared for the next three day to pursue my idea…

Østerbro 2014

Rasmus ☺

Abstract

The high strain rate characterisation of FRP materials present the experimenter with a new set of challenges in obtaining valid experimental data. These challenges were addressed in this work with basis in classic wave theory. The stress equilibrium process for linear elastic materials, as fibre-reinforced polymers, were considered, and it was first shown that the loading history controls equilibrium process. Then the High-speed servo-hydraulic test machine was analysed in terms its ability to create a state of constant strain rate in the specimen. The invertible inertial forces in the load train prevented a linear elastic specimen to reach a state of constant strain rate before fracture. This was in contrast to ductile materials, which are widely tested with for the High-speed servo-hydraulic test machine. The development of the analysis and the interpretation of the results, were based on the experience from designing and constructing a high-speed servo-hydraulic test machine and by performing a comprehensive test series. The difficulties encountered in the test work could be addressed with the developed analysis. The conclusion was that the High-speed servo-hydraulic test machine is less suited for testing fibre-reinforced polymers due to their elastic behaviour and low strain to failure. This is problematic as the High-speed servo-hydraulic test machine closes the gap between quasi-static tests rates and lower strain rates, which are achievable with the Split Hopkinson Pressure Bar.

The Split Hopkinson Pressure Bar was addressed in terms of a new wave mechanics model for a linear elastic specimen in the Split Hopkinson Pressure Bar. The model was formulated without any assumption of stress equilibrium, constant strain rate, or equal bars and thus provided a useful tool to analyse the equilibrium process. The model showed that whichever stress equilibrium of constant strain rate happen first, depended on the combination of impedance mismatch between the specimen and the bars. The model was compared to a series of tests, and the model correctly indicated when a test set-up was problematic in terms of reaching stress equilibrium and constant strain rate. As shown in literature the incident wave should be linear rising pulse to facilitate stress equilibrium and constant strain rate. The common pulse shaping technique with copper disc's between the Striker bar and Incident bar were addresses and was concluded the method could create the required Incident waves. However, there was an upper limit in the generated stress rates due to frictional problems and this limited the maximum achievable strain rates. The maximum strain rate was also found to be independent of the specimen gage length, which only controlled the time to maximum strain rate.

The Split Hopkinson Pressure Bar proved able to reach a state of stress equilibrium and constant strain rate, but the key to valid data was found in the control of the Incident wave.

Abstrakt

Materiale karakterisering af fiberforstærket plast materialer ved høje tøjningshastigheder er udfordrende på grund af de hurtige belastninger, og for at opnå valide data skal testen være designet så prøveemnet opnår en homogen deformation- og spændingstilstand inden brud. I dette arbejde blev problem stillingen først beskrevet ved den klassiske bølgemekanik for elastiske emner. Det blev vist at deformation hastigheden og accelerationen en er styrende for om emnet opnår en homogen deformations og spændingstilstand inden brud. Udfordringerne var derfor at styre deformationen af emnet korrekt. Højhastighedstrækprøvemaskinen har åbnet op for mulighed for at testes ved middel tøjningshastigheder og dens evner til at opnå en homogen deformations og spændingstilstand blev analyseret. Det blev fundet at inertikræfterne i last toget på maskinen forhindrede emnet i at opnå en konstant tøjningshastighed før brud. Dette blev verificeret via en række forsøg med en højhastighedstrækprøvemaskine der blev udviklet og bygget på Danmark Tekniske Universitet. Dette stod i kontrast til test af metaller en der en standardiseret test på højhastighedsmaskinen og hvor konstant tøjningshastighed kan opnås. Konklusionen blev at de testmetoder der er succesfulde for metaller ikke var gældende for fiberforstærket materialer, på grund af deres elastiske opførsel og lave brudtøjning. Dette er problematisk da højhastighedsmaskinen kunne teste ved tøjningshastigheder hvor andre metoder var praktisk umulige.

Ved højere tøjningshastigheder anvendes der en Split Hopkinson Pressure Bar. Denne metode blev analyseret ved formulering af en ny bølgemekanik model for test emnet. Modellen muliggjorde analyse af ligevægtsprocessen op til den homogene spændingstilstand uden antagelser om en homogen spændingstilstand eller en konstant tøjningshastighed. Yderligere kunne modellen håndtere stødstænger af forskellige materialer og diametre og indeholdte derfor ikke de begrænsning som de modeller der eksisterede i litteraturen. Modellen viste at hvorvidt om den konstant tøjningshastighed eller den homogene spændingstilstand indtræffer først, afhænger af impedans forholdet mellem testemnet og stødstængerne. Det blev også vist at testemnet længde ikke er styrende for den maksimalt mulige tøjningshastighed, men kun styre tiden det tager at opnå den. Modellen blev sammenlignet med en række test udført på en Split Hopkinson Pressure Bar ved University of Southampton. Litteraturen har vist at test emnet i en Split Hopkinson Pressure Bar skal belasted med en konstant acceleration for at opnå en homogen spændingstilstand og konstant tøjningshastighed før brud. I dette arbejde blev det vist at en bredt anvendt ”pulse shaping” metode til at genere den konstant acceleration var begrænset i hvor høj en acceleration der kunne opnås og derved var metoden begrænset. Det blev dog konkluderet at så længe acceleration kunne styres tilfredsstillende så var det muligt at opnår en konstant tøjningshastighed og homogen spændingstilstand før brud.

1 Introduction

The stress-strain behaviour of fibre reinforced polymeric (FRP) composites materials, can be highly strain rate dependent. Typically, the stiffness and strength increases with increasing applied strain rate and the overall behaviour becomes more brittle. FRP materials are becoming more widely used in primary and secondary structures in engineering applications, where weight is a critical factor. These applications include both military and civilian structures such as vehicles and airplanes, and often the applications are exposed to dynamic and transient impact that causes damage at high strain rates. Some parts of the structure are exposed to very high strain rates, whereas others are subjected to lower strain rates. Simulation of the events incorporates materials models that describe the material behaviour at different strain rates and they are calibrated from material tests performed at elevated strain rates.

The established high strain rate test methods are aimed at metallic materials[1], however, no dedicated high strain test methods and procedures exist for fibre reinforced polymeric composite materials. The field remains a research task, which adapts methods from the metallic materials testing to testing of FRP materials.

The anisotropic behaviour of FRP materials makes it a cumbersome and costly task to measure all material parameters at elevated strain rates. Strain rate effects can be divided into a viscous elastic effect and a strength effect. The viscous elastic effects are a change of the elastic response with strain rate, and, it is not given that all constitutive parameters has the same strain rate sensitivity. The strength effect is a change in failure stress and failure strain with strain rate and it is not either given that the failure properties possess the same strain rate sensitivity. The experimental procedures are often tailored to the specific material parameter(s) to be estimated [2] and further specialisation of the equipment is needed when the strain rate is increased. The test set-ups become highly complex and factors such as inertia come into play, which complicates the data interpretation and validation. Figure 1.1 shows a classic overview of strain rates, prevailing test methods, and considerations. At strain rates up to 0.1 /s, the range covered by standard test machines, the process is considered Isothermal, and inertia forces can be ignored. Above 0.1/s, inertial force must be taken into consideration in the experimental set-up and the test equipment becomes specialised. Heavily modified servo-hydraulic test machines are used to access the strain rate range. Further, the deformation process becomes adiabatic and the test specimens may experience severe heating. The Split Hopkinson Pressure Bar (SHPB) is the preferred method from 200/s and up to 10^4 /s dependent on the test material. If higher strain rates are to be achieved, the specimen must be brought into a unidirectional strain state, instead of the unidirectional stress state normally used at lower strain rates[3].

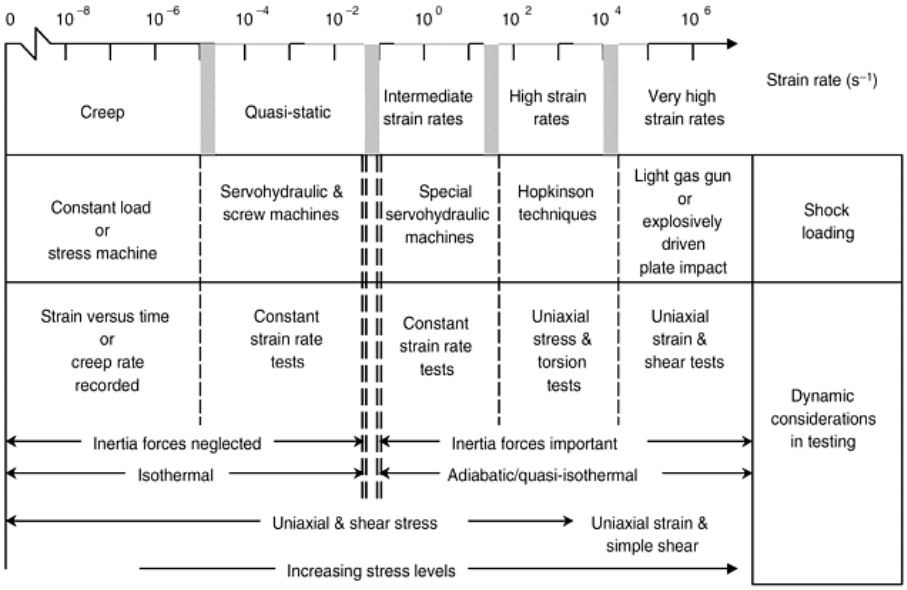

Figure 1.1 Dynamics aspects of mechanical testing [4]

A list of test methods sorted by test type is given in Table 1.1. Reviews of FRP material testing at high strain rate showed that the Split Hopkinson Pressure Bar and the high-speed servo-hydraulic test machine were the preferred methods for testing FRP materials [4-6]. The combination of these methods covers a strain rate regime from 0.1 all the way up to more than 1000 /s. Further, these are also the standardised methods for testing metallic materials [7-9]. The car industry particularly has driven the standardisation of high strain rate testing of metallic materials in the high-speed servo-hydraulic test machine [7, 10-13].

Table 1.1 Strain rates and different testing techniques adopted from [14]

Applicable strain rate, /s	Testing Technique
Compression tests	
<0.1	Conventional load frames
0.1 - 500	High speed servo hydraulic test machine
0.1 - 500	Cam plastometer
$200 – 10^4$	Split Hopkinson Pressure Bar
$10^3 – 10^5$	Taylor impact test
Tension test	
<0.1	Conventional load frames
0.1 - 500	High speed servo hydraulic test machine
$200 – 5x10^3$	Split Hopkinson Tension Bar
10^4	Expanding ring
$>10^5$	Flyer plate
Shear and multi axial tests	
<0.1	Conventional load frames
0.1 - 500	High speed servo hydraulic test machine
$10 – 10^3$	Torsional impact
$100 – 10^4$	Split Hopkinson Pressure Bar (Shear/Torsion)
$10^3 – 10^4$	Double notch shear and punch
$10^4 – 10^7$	Pressure-shear plate impact

It is reasonable to take already established methods and transfer them to other materials such as FRP. However, in high strain rate testing, there is a great interaction between the test specimen and the test machine and method, which may work for one type of material, but may not work for another. In this work, only advanced FRP materials with highly aligned fibres and fibre volume content above 50 % are considered. These types of material behave in many cases elastic up to

fracture, and do not exhibit plasticity before fracture as with metallic materials. Further, the absorbed deformation before failure is very slight compared to metallic materials, due to low failure strains. Depending on the lay-up of the fibres, FRP materials are also highly orthotropic, which complicates the specimen design compared to the isotropic metallic materials. The differences entail that the standards for metallic materials cannot be used as direct guidelines for designed high strain rate testing of FRP materials and modification has to be applied. Hamouda et al. [14] listed the important issues for dynamic testing of FRP materials:

1. Devising launch mechanism to produce the desired deformation state
2. Fixing the specimen in the test set-up
3. Selection of specimen geometry
4. Test duration and equilibrium time
5. Measuring transient parameters accurately
6. Data collection, management, and interpretation.

The launch mechanism may need a different set-up to produce the desired deformation state, since FRP materials react differently than metallic materials. Fixing the specimen is also more complicated due the orthotropic behaviour of FRP materials and the weak polymers around the fibres. This is also connected to the specimen design, which is significantly altered compared to metallic materials. Stress and strain are normally measured as average quantities over the specimen, and that implies that the specimen is assumed to be in a homogenous stress state. In a high strain rate test there may not be time to reach a homogenous stress state and this is more pronounced for FRP materials due to low failure strains and low wave velocities compared to metallic materials. The measurement itself of stress and strain on the specimen is complicated and inertia forces may corrupt the recorded signals and this depends on how close the sensors can be put to the specimen. The data interpretation may be different for FRP materials as they response differently to deformation.
This work has focused on establishment of robust experimental test methods with the high-speed servo-hydraulic test machine and the SHPB test rig. The high-speed servo-hydraulic test machine was used for tensile testing whereas the SHPB was used in compression.

1.1 Thesis structure and novelty

The next sections of this chapter describe the concepts of strain and strain as used throughout the work. Then the basic concept of dynamic deformation and wave mechanics is introduced, as well as a brief overview of results from literature of high strain rate testing of FRP materials.

- Chapter 2 describes the high-speed servo-hydraulic test machine in depth. Then, to examine the interaction between the test specimen, the machine, and the limitations of the method, a new model of the load train of the machine is presented.
- Chapter 3 describes the design and construction of a high-speed servo-hydraulic machine, which was done as a part of this work.
- Chapter 4 describe a test series carried out at the constructed test machine. Parallels are drawn to the work in chapter 3.
- Chapter 5 describes the Split Hopkinson Pressure bars. A new method for calibration of the bars is proposed in this chapter. Further, a new examination of the widely used pulse shaping technique is given together with its limitations.
- Chapter 6 describes a new generalised analytical wave mechanics model of the specimen response for linear elastic materials in the SHPB. The model was used to set up a design algorithm for specimen design, and to assess the limitation in achievable strain rates.
- Chapter 7 presents a new momentum trap method for the SHPB test rig. The method

was easier to implement in an existing SHPB test rig than known methods from the literature.

- Chapter 8 presents a set of tests on an SHPB test rig performed with the methods described in chapters 5, 6 and 7.
- Chapter 9 summarise the work and draws a perspective.
- Appendix A is a description of high-speed imaging. High-speed imaging has been employed throughout the work together with Digital Image Correlation where possible for verification of the measurement.

References to the remaining appendixes are given throughout the thesis.
The sequence of the chapters does not represent the chronological order of the work. The work in Chapter 2 was first completed after chapters 3 and 4, as this work gave the necessary experience to finalize the model in chapter 2. The work in chapter 6, especially that dealing with specimen design, was first fully completed after the test in chapter 8 was completed.
The work in chapters 7 and 8 was carried out on an SHPB test rig at the University of Southampton, whereas the work in chapters 5 and 6 was partly carried out at the University of Southampton. The remaining work was carried out at the Technical University of Denmark.

1.2 Strain

Strain is the relative measure of deformation. An example is a bar with original length L deformed by dL to final length L_f as in Figure 1.2. The common methods for calculating strain from this deformation are listed in Table 1.2 along with their equations.

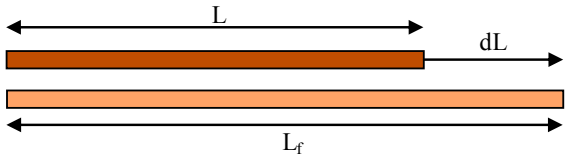

Figure 1.2 Bar deformed from initial length L to final length L_f with the increment dL

Table 1.2 Formulas for average strain measures after deformation dL

Engineering strain	Stretch ratio	True strain	Green strain	Almansi strain
$\varepsilon_{tech} = \frac{dL}{L}$	$\lambda = \frac{L_f}{L}$	$\varepsilon_{True} = ln\left(\frac{L_f}{L}\right)$	$\varepsilon_{Green} = (\lambda^2 - 1)$	$\varepsilon_{Almansi} = \frac{1}{2}\left(1 - \frac{1}{\lambda^2}\right)$

Using the engineering strain as a reference, the differences in strain measures were examined. L was set to 1 and L_f was varied between 0 and 0.05. The different strain measures were calculated and plotted in Figure 1.2A. The relative deviations of the strain measures were calculated and plotted in Figure 1.2B as a function of dL.

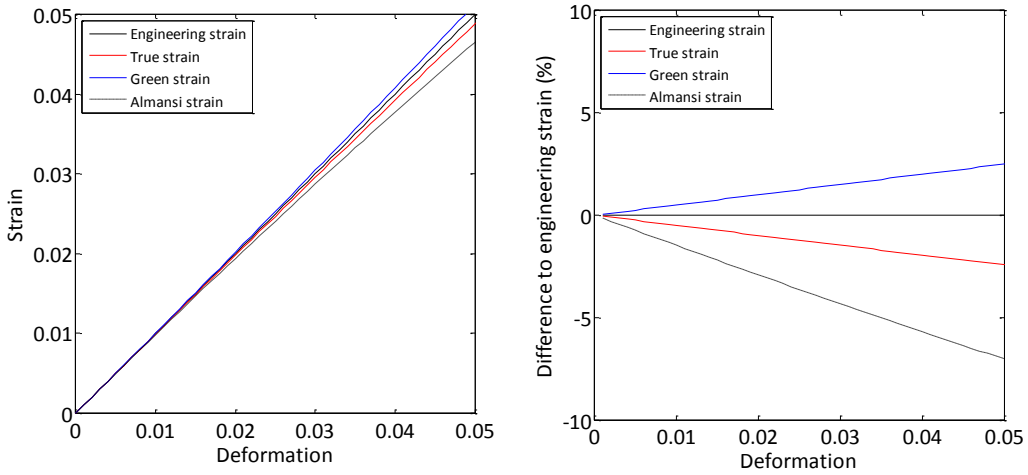

A) Strain measure as function of the deformation dL for a bar of length L=1.

B) Relative deviation of strain compared to the engineering strain measure.

Figure 1.3 Strain measures and relative deviation compared to the engineering strain measure.

1.3 Strain rate

Strain rate is defined as the rate of change of strain with respect to time written as

$$\dot{\varepsilon} = \frac{d\varepsilon}{dt} \tag{1.1}$$

If dL is applied during a time period dt, the deformation velocity is $V_0 = \frac{dL}{dt}$. It follows from the definition of engineering strain and equation (1.1) that the engineering strain rate is

$$\dot{\varepsilon}_{eng} = \frac{V_0}{L} \tag{1.2}$$

In terms of engineering strain, the strain rate is proportional to the deformation velocity. The differences in strain rate measures were examined by applying the deformation dL in Figure 1.2 with a constant velocity V such that the engineering strain rate equalled 1. The corresponding strain rates for the other strain measures were calculated from equation (1.1) and Figure 1.4A shows the result. The engineering strain rate was used as reference, and the relative deviation was calculated. Figure 1.4B shows that within an applied deformation of 5% engineering strain, the engineering and true strain rates will deviate less than 5%. FRP materials deform up to 5-7% technical strain [15] but will likely fail at less strain, especially for UD materials in the fibre direction. Thus, the engineering strain can be used as a measure for strain and strain rate without deviating substantially from the true strain and strain rate. The engineering strain and strain measures are used throughout this work.

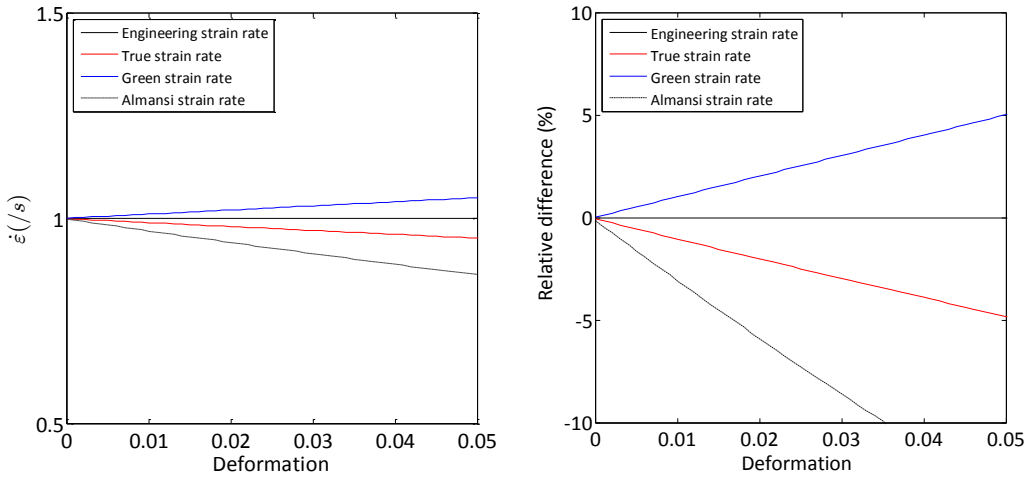

A) Strain rate as function of the applied deformation *B) Deviation of strain rate compared to the engineering strain rate*

Figure 1.4 Calculated strain rate as function of the applied deformation

1.4 Dynamic deformation

Equation (1.2) assumes implicitly equilibrium conditions over the specimen as the deformation per time is averaged over the length L. When a dynamic approach is used instead, the strain rate depends on how the deformation velocity is applied. The concept of stress waves in solids is used to establish a closer look at the development of deformation in an elastic solid. 1D stress wave motion in a slender elastic homogenous bar is described by the wave equation [3, 16]

$$\frac{\partial^2 u}{\partial t^2} = C_0^2 \frac{\partial^2 u}{\partial x^2} \tag{1.3}$$

C_0 is the 1D wave propagation velocity calculated as

$$C_0 = \sqrt{\frac{E}{\rho}} \tag{1.4}$$

E is the elastic modulus along the propagation direction and ρ is the density of the bar material. D'Alembert's solution applies [3, 16] so the displacement u, velocity V, acceleration a and stress σ -measures are given by

$$\begin{aligned} u(x,t) &= F(x - C_0 t) + G(x + C_0 t) \\ V(x,t) &= \frac{\partial u(x,t)}{\partial t} = C_0\big(-F'(x - C_0 t) + G'(x + C_0 t)\big) \\ a(x,t) &= \frac{\partial^2 u(x,t)}{\partial t^2} = C_0^2\big(F''(x - C_0 t) + G''(x + C_0 t)\big) \\ \sigma(x,t) &= \frac{\partial u(x,t)}{\partial x} = E\big(F'(x - C_0 t) + G'(x + C_0 t)\big) \end{aligned} \tag{1.5}$$

F and G are non-harmonic functions that describe the wave shape. F describes a wave that travels in the positive defined direction of the bar whereas G describes a wave traveling in the negative direction. If the deformation dL in Figure 1.2 is applied as an impact with a velocity V_0, the deformation will propagate through the bar at the elastic wave velocity as illustrated in Figure 1.5, and the stress associated with the deformation propagating is [3]

$$\sigma = \rho C_0 V_0 \tag{1.6}$$

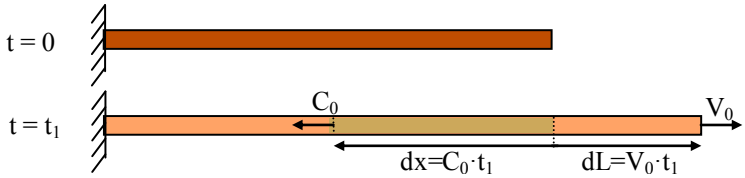

Figure 1.5 Deformation of bar – distribution of wave deformation

At time a arbitrary time $t_1 > t_0$ the velocity change is distributed over the distance $dx = C_0 \cdot t_1$ into the material and the deformation simultaneously reaches a value of $dL = V_0 \cdot t_1$. The deformation has then been distributed over a distance dx and the technical strain in this region is

$$\varepsilon_0 = \frac{dL}{dx} = \frac{V_0}{C_0} \tag{1.7}$$

The strain in equation (1.7) can also be found directly from equation (1.6) using Hook's law

$$\varepsilon_0 = \frac{\rho C_0 V_0}{E} = \frac{V_0}{C_0} \tag{1.8}$$

Thus, in the event of an instantaneous acceleration of one end of the bar to a constant velocity V_0, the velocity will distribute through the bar at a finite velocity C_0 and leave a strain field with constant amplitude behind its front. V_0 is called the particle velocity. The strain rate is very high at the passages of the wave front through the un-deformed material, but elsewhere the strain rate is zero. The wave interacts with the interface at the clamped end. An interface is any change in the total impedance where impedance is defined as [16]

$$Z = \rho C = \rho \sqrt{\frac{E}{\rho}} = \sqrt{\rho E} \tag{1.9}$$

The total impedance is defined as

$$Z_T = \rho C A = \sqrt{\rho E} A \tag{1.10}$$

A is the cross sectional area of the bar. To describe the interaction with the interface, basic reflection theory is introduced. A stress wave in an elastic solid will reflect and transmit across an interface. Three waves are defined:

- σ_I is the Incident wave
- σ_R is the Reflected wave
- σ_T is the Transmitted wave

Figure 1.5 shows the interface with waves defined.

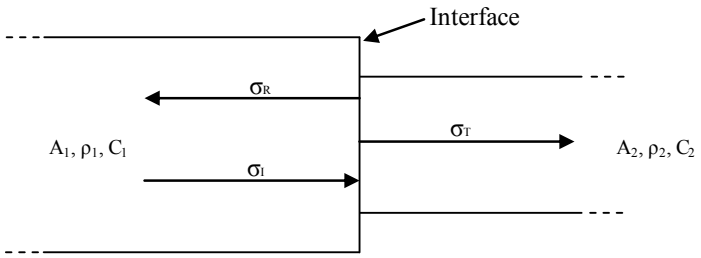

Figure 1.6 Interface between two slender bars

If no material is superimposed or gaps are created, the interface must be in equilibrium in terms of forces and particle velocities. From this the basic reflection and transmission equation is derived. The transmission and reflection coefficients can be calculated as [3, 16]

$$\frac{\sigma_T}{\sigma_I} = \frac{2A_1\rho_2C_2}{A_1\rho_1C_1 + A_2\rho_2C_2} \tag{1.11}$$

$$\frac{\sigma_R}{\sigma_I} = \frac{A_2\rho_2C_2 - A_1\rho_1C_1}{A_2\rho_2C_2 + A_1\rho_1C_1} \tag{1.12}$$

When the wave reaches the clamped end, the wave reflects and transmits. If the clamped end is completely rigid (E = ∞) such that complete reflection occurs the strain (and stress) doubles to $2\cdot\varepsilon_o$ in the reflection and propagates back to the other end. This is seen by rewriting equation (1.12) as

$$\frac{\sigma_R}{\sigma_I} = \frac{1 + A_1\rho_1C_1/A_2\rho_2C_2}{1 + A_1\rho_1C_1/A_2\rho_2C_2} \cong 1 \Rightarrow \sigma_R = \sigma_I \tag{1.13}$$

Using equation (1.5), the stress sum of two waves that travel in each direction but overlap each other becomes

$$\sigma = \sigma_R + \sigma_I = 2\sigma_I \tag{1.14}$$

At a materials point the strain rate will be very high when the wave front passes, but zero at all times during the deformation. Therefore, equation (1.2) is not representative for the strain rate destribution in the bar, as only the average strain rate is given. The equilibrium process is visualised in Figure 1.7 with a LS Dyna simulation of a slender bar with rigid boundaries at both ends. The plot shows strain at different points in the bar as function of time. The strain rises quickly when the wave passes, and then comes to a stable level before the wave passes again. The shown material point (elements) only feels a high strain rate when the wave passes. During the remaining time, the strain rate is zero, or close to zero. Furthermore, when both ends of the bar are connected to rigid barriers, stress equilibrium will never be acquired if stress equilibrium is taken as no stress difference between the ends of the bar. The stress difference is always the stress given by equation (1.6). However, if the definition of stress equilibrium is relaxed, such that the stress equilibrium is calculated as the stress difference divided by the average stress, a "dynamic" equilibrium can be reached. The relative stress difference is calculated as in equation (1.15) with S_a and S_b representing the stresses at the end of the bar.

$$R = 2\left|\frac{s_a - s_b}{s_a + s_b}\right| \tag{1.15}$$

The equilibrium is well established within the split Hopkinson Pressure Bar (SHPB) community and commonly used with R = 0.05 as the acceptance criteria for stress equilibrium [17-22].

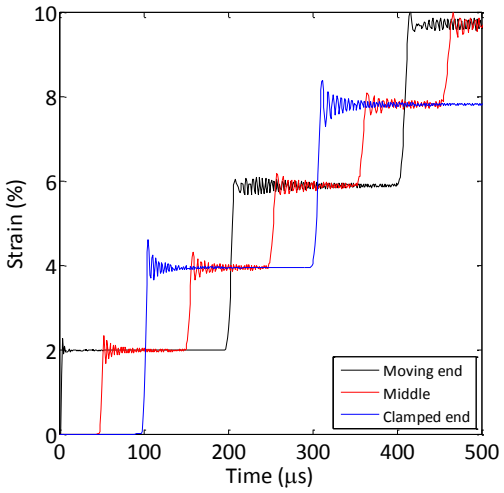

Figure 1.7 Simulation with LS Dyna of a 0.2m long and 0.02m wide bar. The nodes are rigidly clamped in one end and in the other end the nodes are given an initial velocity of 20m/s which is maintained through how the entire simulation. E = 1GPa, ρ=1000kg/m^3. Poisson's ratio is set to zero to remove dispersion noise from the plot.

Equation (1.6) gives some interesting observations about the maximum impact velocity for a given material. Shifting σ to σ_{tu}, the ultimate tensile strength for linear elastic materials the maximum velocity becomes

$$V_{0max} = \frac{\sigma_{tu}}{\rho C} \tag{1.16}$$

At $V_{0\ max}$ the material fails instantaneously upon loading at the loaded end. Equation (1.16) is also appropriate for materials with a yield point if σ_{tu} is changed to the yield stress σ_y. Then the material is predicted to yield instantaneously [3]. Table 1.3 compares the maximum $V_{0\ max}$ for steel and aluminium with the same yield strength. The steel is penalised by its higher density and requires three times higher yield strength than the aluminium to handle the same $V_{0\ max}$ as aluminium. The yield strength has to scale with the density to maintain the maximum impact velocity as seen in equation (1.16).

Table 1.3 Maximum impact velocity $V_{0\ max}$ for steel and aluminium with the same yield strength

	Steel	**Aluminium**
Yield strength	500MPa	500MPa
Wave velocity	5000 m/s	5000 m/s
Density	7900 kg/m^3	2800 kg/m^3
$V_{0\ max}$	**13 m/s**	**36 m/s**

For FRP materials, the stiffness and density depends on the fibre type(s), the lay-up, and the matrix. Figure 1.8 gives an overview of impact velocities for different material systems listed in the CSE Edupack material database [23]. The database gives a range of values for each material parameter for each material and height of the bars reflect the range of the parameters going into equation (1.16) which is used for Figure 1.8.

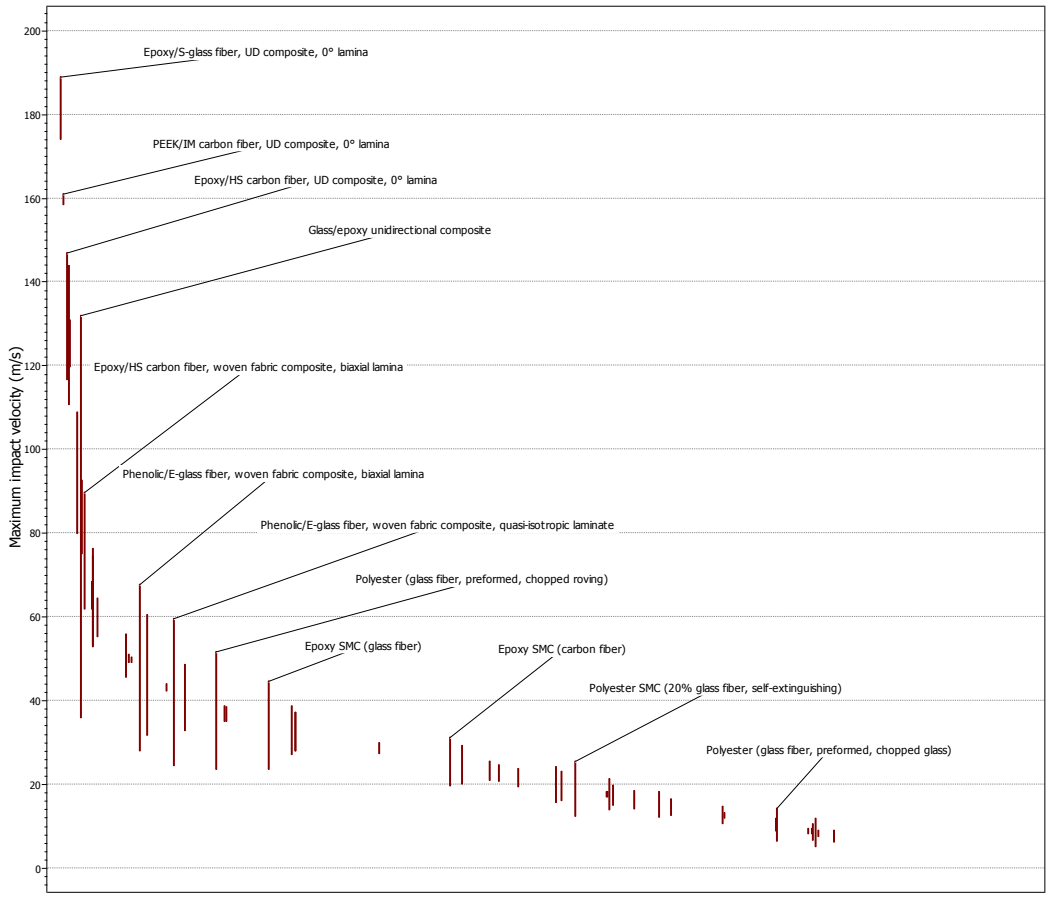

Figure 1.8 Maximum impact velocity for FRP material systems. X-axis is material systems.

This maximum impact velocity is only an upper limit at which the material will fracture immediately on impact. It does not help to explain if homogenous stress state can be reached before the specimen fractures at impact velocities lower than the maximum velocity. In practice, the impact velocity is almost never instantaneously applied; a gradual change of velocity is always applied. One key point in high strain rate testing is to control the acceleration to the test specimen so that a "dynamic" homogenous stress state is reached before specimen failure. Further, the velocity should also be applied in order that the average strain rate approaches a constant level before specimen fracture. This is a major concern of both chapters 2 and 5, which describe the two test methods considered in this work.

1.5 Strain rate sensitivity of FRP materials

FRP materials have multiple factors that influence the strain rate sensitivity. The factors include the fibre type, the fibre lay-up, the volume fraction, and the matrix type. It is difficult to compare the data in the literature since these factors vary from paper to paper. Instead, to give an overview, the methods from Barre et al. and Jacob et al. [5, 6] are adopted, where the effect of strain rate is denoted as "Increase", "Decrease" and "No effect". Only results for FRP materials obtained with the split Hopkinson pressure bar and a high servo-hydraulic test machine were considered. The emphasis was put on the elastic modulus E, the ultimate failure stress and failure strain. The data are presented in Table 1.4.

Table 1.4 Collected material data from literature

Abbreviations

SHPB Compressive Split Hopkinson tests
SHTB Tensile Split Hopkinson tests
VHS High-speed servo-hydraulic test machine.
(Static properties was obtained with standard methods)

E Elastic modulus
σ^u Ultimate failure stress
ε^u Ultimate failure strain

PP Polypropylene
PE Polyethylene
Pol Polyester
Vin Vinyl ester
PPTA Polyphenylene terephthalamide
HMPE High Modulus Polyethylene fibre

Material	Test	Strain rates /s	Results	Reference
Crossply Carbon /Epoxy	SHPB	Static – 817	Increase in E and σ^u Decrease in ε^u	[24]
UD 0° & 90° Carbon /Epoxy	SHPB	Static – 817	Small increase in E and σ^u Small decrease in ε^u	[24]
UD 0° Carbon/Epoxy	SHTB	Static - 450	No effect on E and σ^u	[25]
Quasi Isotropic Carbon /Epoxy	SHTB	Static - 145	Increase in σ^u Decrease in ε^u	[26]
Satin Weave Carbon/Pol	SHPB	Static-1000	Increase in E and σ^u No effect on ε^u	[27]
Plain Weave Carbon/epoxy	SHTP	Static – 2000	σ^u Unchanged	Ref. 16&17 in [6]
UD Carbon/Epoxy	VHS	Static - 45	Increase in σ^u	[28]
Carbon Fibres	SHTP	Static – 1300	E, σ^u and ε^u Unchanged	[29]
3D braided Glass/ epoxy	SHTP	Static - 2800	Increase in E and σ^u Decrease in ε^u	[30]
Plain weave - Aramid/PP	SHTP	Static - 1000	Increase in σ^u Decrease in ε^u	[31]
Plain weave - Aramid/PET1	SHTP	Static - 1000	Increase in σ^u Decrease in ε^u	[31]
Plain weave - Aramid/PET2	SHTP	Static - 1000	Increase in σ^u Decrease in ε^u	[31]
Plain weave - PE/PE	SHTP	Static - 1000	Increase in σ^u Decrease in ε^u	[31]
UD - PE/PE	SHTP	Static - 1000	Increase in σ^u Decrease in ε^u	[31]
Satin Weave Aramid/Pol	SHPB	Static-1000	Increase in E and σ^u No effect on ε^u	[27]
PPTA fibres a and b (Aramid)	SHTP	Static- 850	Decrease in E and increase in σ^u Increase in ε^u	[32]
PPTA fibres (Aramid)	SHTP	Static - 850	Decrease in E and Decrease in σ^u Decrease in ε^u	[32]
HMPE Fibres	SHTP	Static– 800	Decrease in E and increase in σ^u Increase in ε^u	[32]
HMPE fibres (Spectra900)	SHTP	Static -300	Decrease in E and increase in σ^u Decrease in ε^u	[33]
Spectra1000 laminate shield	SHTP	Static-850	Increase in σ^u below 400/s Increase above 400/s	[34]

PPTA fibres (Aramid)	SHTP	Static – 400	Increase in E and increase in σ^u Increase in ε^u	[35]
Plain/ Satin weave /UD Glass/Pol	SHTP	Static – 2000	Increase in σ^u	Ref. 16&17 in [6]
Plain/ Satin weave /UD Glass/Epoxy	SHTP	Static – 2000	Increase in σ^u	Ref. 16&17 in [6]
Plain weave Glass/Epoxy	SHPB	Static -1000	Increase in E and σ^u	[36]
UD Glass/Epoxy	VHS	Static - 500	Increase in E and decrease in σ^u and ε^u	[37]
UD Glass/Epoxy	VHS	Static -100	Increase in σ^u	[28]
UD Glass/Pol	VHS	Static -100	Increase in E and σ^u	[38]
Plain Weave Glass/Epoxy	SHTP	Static -400	Increase in σ^u	[39]
Commingled plain weave E-glass/polypropylene	Drop test (Tension/ Comp)	Static - 120	Increase in E and σ^u Increase in ε^u	[40]
S-2 Glass/Epoxy SC-15	SHPB	Quasi-1100	Increase in E and σ^u Slight decrease in ε^u	[41]
Plain weave S2-Glass/Vin	SHPB	Quasi - 800	Increase in E and σ^u Increase in ε^u	[42]
Crossply Glass Epoxy	VHS	Quasi - 100	Slight increase in E and σ^u Increase in ε^u	[43]

The most commonly studied materials in the literature are the glass/epoxy (GFRP) and carbon/epoxy (CFRP) in different configurations. Based on the data in Table 1.4 GFRP appears to be more rate sensitive in all considered parameters than CFRP, a conclusion also reached by Barre et al. [6]. In addition, Barre et al. concluded that weaved fibre structures for GFRP were more rate sensitive than UD. Furthermore, plain weave was more sensitive than a five satin weave. This indicates that the rate sensitivities are related to the elastic interactions between the matrix and fibre, since a satin weave has less elastic interaction than a plain weave. Zhou et al. [29] presented a comparison of fibre bundles and found the carbon fibres were insensitive to strain rate whereas the glass fibres were highly sensitive as shown in Figure 1.9.

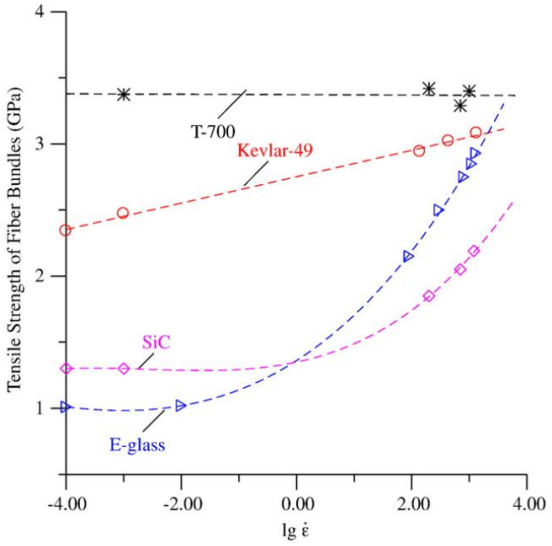

Figure 1.9 Comparison of fibre bundle tensile strength (T-700 = Carbon fibre) [29]

The specific type of fibre and Matrix can have a great influence on the behaviour as shown in Figure 1.10.

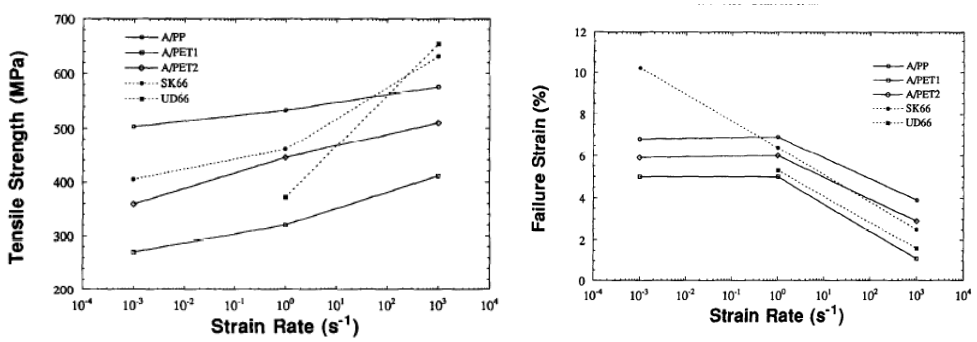

A) Rate sensitivity of tensile strength *B) Rate sensitivity of failure strength*

Figure 1.10 Tensile strength and failure strain for Aramid and polyethylene fibres (SK66 and UD66) [31]

The brief overview of data given here indicates that many factors affect the rate sensitivity of FRP materials. An examination of Table 1.4 shows that contradictions exist in some of the obtained results in the literature, a conclusion also reached by others [4-6]. For example, do PPTA fibres and UD CRFP materials have the ability to both increase and decrease in strength? These contradictions highlight the importance of examining the test methods to identify potential improvements and to understand their limitations.

2 Examination of the servo-hydraulic test-machine as a high speed loading device

High-speed servo-hydraulic test machines are becoming widely used in the automotive industry to test sheet metals at strain rates between 1-500/s [7], and a standardised test method was developed based on years of research [9]. This work has spread to other types of materials and a test standard was developed for pure polymers [44], but not to fibre-reinforced polymers. Several papers reported the use of high-speed servo hydraulic machines [6, 38, 45-49] for testing FRP materials at elevated strain rates. However, different specimen geometry, different gripping methods, and different load measurements methods were used. The variety of methods demonstrated the lack of a standard in the field and gives space for an examination of the high-speed servo hydraulic test machine for FRP material testing at elevated strain rates.
This chapter describes the working method of the high-speed servo-hydraulic test machine. Then a set of ordinary second order differential equations is used to model the "load train" for testing FRP materials and conclusion is drawn about the influence of the load train to the measured data. Comparisons are made to real tests for validating the models.

2.1 Description of the high servo hydraulic machine

A servo-hydraulic test-machine consists of a hydraulic cylinder mounted into a steel frame. The test specimen is mounted to the frame, and the piston rod of the hydraulic cylinder. The specimen is deformed in either tension or compression by moving the piston rod. Pressurised oil is used as medium to transfer kinetic energy to the piston rod. The oil is pressurised by a hydraulic pump and a servo valve is used to control the oil flow to- and from the hydraulic cylinder and controlling the deformation of the specimen. Figure 2.1 shows a schematic overview of a high-speed hydraulic test machine.

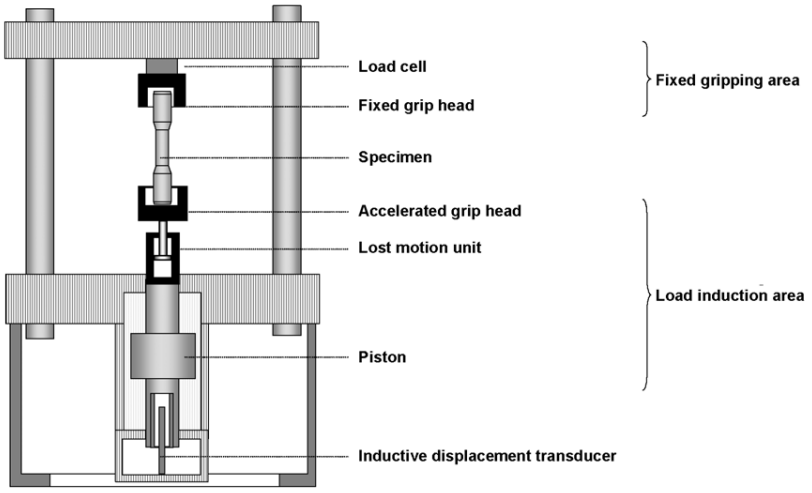

Figure 2.1 Schematic overview of the servo hydraulic test machine [1]. *The addition of a "Lost motion unit" in the load train is a major different to standard one axis hydraulic test machines. The lost motion unit allows the piston rod to accelerate to a given velocity before the specimen is loaded.*

The maximum oil flow rate of the hydraulic system determines the maximum piston rod velocity. Big hydraulic pumps delivers a flow rate of hundreds of litres per minute, but for velocities above 1 – 5 m/s, several thousand litres per minute is required dependent of the machine setup. Only a small volume of oil is required at the high flow rates and normally hydraulic accumulators are used for supplying the oil at these high flow rates. A hydraulic bladder accumulator consists of a combined oil/gas cylinder with a bladder inside which separate the oil from the gas. The gas is pre-set to a given pressure and during operation, the oil will flow into the accumulator until the gas is compressed to the same pressure as the oil. The compression happens with a low oil flow rate, but when the system pressure decreases the gas expand at rates up to its sonic speed and forces the oil into the system.

The hydraulic cylinders are normally double acting with equal pressurised areas, and oil flow to and from the cylinder is controlled with a (4/3)[1] way servo valve. Oil flows to one side of the cylinder while oil is allowed to escape from the other side, when the valve opens. Both the in- and outgoing oil flow is going through the servo valve and the flow rate is controlled by the valve opening and the pressure drop over the valve. As the oil start to flow into the cylinder the oil pressure drops and the gas in the accumulator starts to expand and forcing oil into the system. As the oil is flowing through the valve, a pressure drop occurs over the valve due to the flow resistance that increases with flow rate. Valves are normally rated to a given flow for a given pressure drop at a given opening of the valve. Flows for other pressure drops are calculated with the square root function for sharp edged orifices [50]:

$$\frac{Q}{Q_N} = \sqrt{\frac{P}{P_N}} \tag{2.1}$$

Q_N and P_N are the rated flow and rated pressure drop and Q is an arbitrary flow with its associated pressure drop P. When the oil flows out of the cylinder, it goes through the valve and directly to tank on the pump. The tank is depressurised so there is no pressure on the outlet side of the valve and a pressure must be build up to force the oil fast enough through the valve. Then, the pressure

[1] (4/3) means four ports and three positions. The four ports are Pressure, Return, Channel A, and Channel B. In first position Pressure is connected to Channel A, and Return to Channel B. In second position the Pressure is connected to Channel B and Return connected to Channel A. The last position is no connections.

differential over the piston rod is the gas pressure in the accumulators, minus the pressure loss in the ingoing side of valve, and minus the pressure build-up before the outgoing side of the valve. Other hydraulic resistance and internal mechanical friction in the cylinder also reduces the pressure differential over the piston rod. However, the main loss is over the valve for a high quality system. This pressure differential is driving the acceleration of the piston rod and/or the force, which deform the test specimen in the test machine. The piston rod velocity is first constant when the pressure differential is zero and all pressure is lost in the valve and friction. Figure 2.2 shows the pressure losses when the valve opens, and when the piston rod has obtained constant velocity.

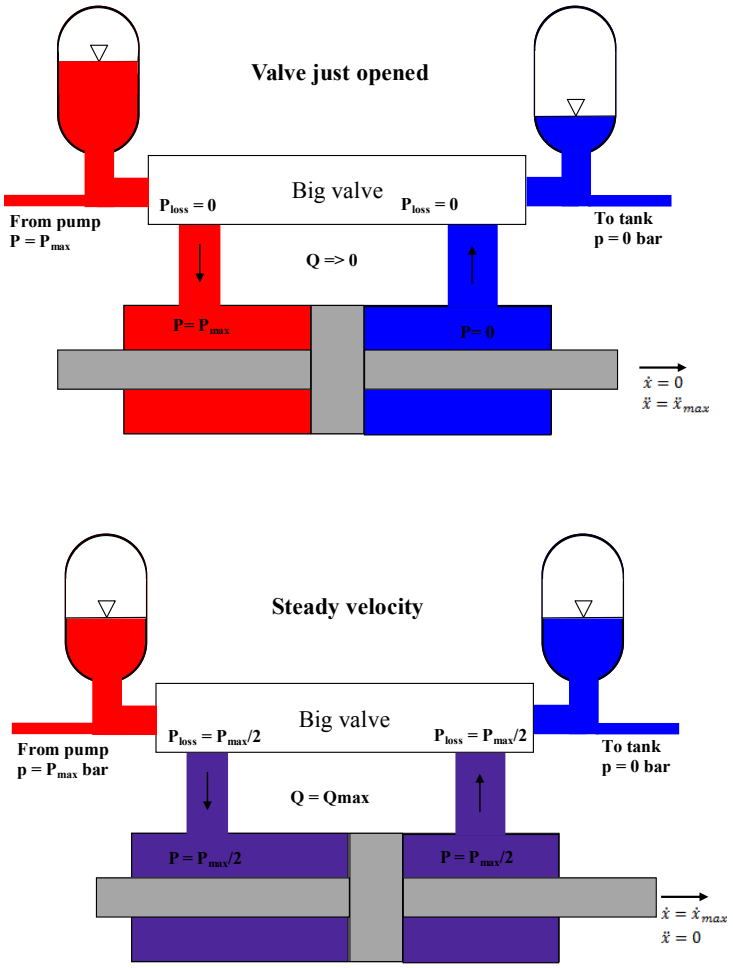

Figure 2.2 Pressure drop at valve during opening and at steady piston rod velocity. $P_{max}/2$ is lost when oil passes the valve into the cylinder and a pressure of $P_{max}/2$ is build up in the cylinder as the oil has to pass out of the valve. $\ddot{x}$ is the piston rod acceleration and $\dot{x}$ is the piston rod velocity.

Commercial high-speed hydraulic test-machines reach 20 – 25m/s in piston rod velocity, utilizing this principle of accumulator driven oil flow. Since the pressure differential is zero at constant velocity, there is no force to deform the specimen upon impact with the specimen. Deformation is only achieved through the kinetic energy of the piston rod and by deacceleration of the piston rod. However, a pressure differential builds up as soon the the piston rod deaccelerates.

Hydraulic test-machines normally operate with oil pressures ranging from 210 – 280 bars where high-speed servo-hydraulic machines tend to utilize 280 bars pressure. The machine can be designed with smaller moving components at this pressure, while maintaining the performance

comparing to using 210 bar oil pressure.
Standard test machines operate with a closed loop controller, which uses a feedback signal from the test machine to adjust the piston rod movement. For high-speed servo-hydraulic test machines, the closed loop control principle cannot be used, since the electrical and mechanical dynamics are not sufficient at the high piston rod velocities [7]. Instead, open loop control is used where the valve is opened and left at some constant opening until the test is over. There is no adjustment of the opening during test and the system is unable to adapt to external forces, such as the impact of the specimen.

2.1.1 Lost motion unit - Slack adapters

Material testing at quasi static rates is performed with piston rod velocities of 0.1-5mm/min [51]with an acceleration length of few micrometres, whereas high-speed servo hydraulic test machine requires 100 – 300 mm acceleration length to reach 20 – 30m/s (1.8e6 mm/min). This acceleration length is far above the 1-3mm displacement to failure for a UD GFRP test specimen, with a gage length of 50-150mm and a fracture strain of about 2%.
Devices as "slack adapters/lost motion units" allow the piston rod to accelerate before impact of the specimen [1, 10, 12, 45, 47, 52]. The slack adapter converts the long acceleration length of the piston rod to a short acceleration length for the specimen, thus aiming to accelerate the moving end of the specimen to the test velocity before the specimen fractures. Figure 2.3 shows three designs of slack adapters.

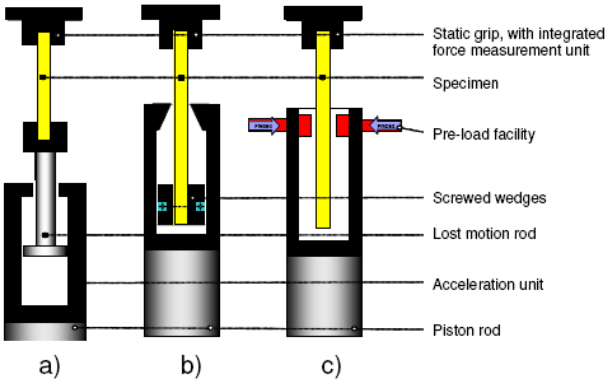

Figure 2.3 Different concepts for the slack adapter [12]

In (a) the piston rod accelerates to the desired velocity and impacts the lost motion rod (LMR). Typically, a piece of soft material as rubber is put between the contact faces to avoid too high contact forces. The thickness of the rubber layer will influence the acceleration length of the specimen. The LMR is not rigidly connected to the piston rod and can bump between the impact velocity and velocity higher than this [7, 13]. Approach (a) also adds extra mass to the specimen, which causes inertial damping. Approach (b) is optimized with wedges to avoid rebounds but is sensitive to matching geometries and alignment. Approach (c) is a preloaded unit, which moves with the piston rod along an extended test specimen. The unit releases and grip the specimen when the test velocity is reached. The benefit from this design is the absence of a lower grip, which damp the accelerations of the specimen. This approach is widely used for testing sheet metals in the car industry [7, 10, 53]. The specimen for approach (c) has a special design with an elongated end, which is stronger than the gage area, and the required specimen design is shown in Figure 2.4, along with straight test specimens used for FRP materials. The straight sided coupon has a very long effective gage length in this configuration, which results in a low strain rate for high impact velocities.

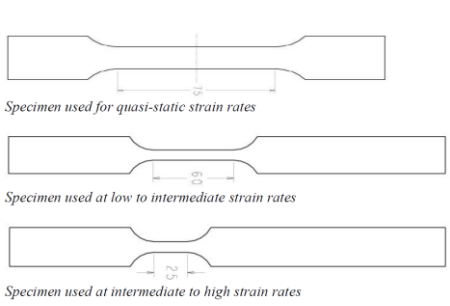

A) specimen designs for metallic materials[7]

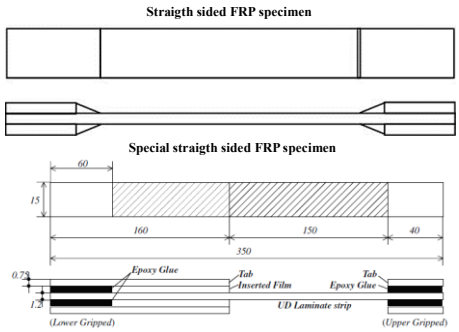

B) Specimen designs for FRP. The special specimen design for FRP materials is taken from [28].

Figure 2.4 Specimen design used with approach (c) in Figure 2.3.

Approach (c) in Figure 2.3 is developed of Instron ltd under the name "Fast Jaws" and this name is used throughout this work.

2.1.2 Load measuring

Load can be measured with a strain gage based load cell, a piezo electric based loadcell, with a dynamometer, a strain gage directly on the test specimen, or with a strain gage directly on the grip(s). The following recommendation is reported in literature with respect to test of metallic materials [1]:

1. Conventional strain gage instrumented load cell — Strain rate < 10/s.
2. Piezoelectric load cell — Strain rate < 100/s.
3. Strain gages mounted on specimen or static grip — For all strain rates.

A rapidly changing load will cause the load cell to oscillate at its resonance frequency known as ringing. For metallic materials, the oscillations are introduced at the yield point while for elastic brittle materials they may appear from the beginning of the loading. Figure 2.5 shows this behaviour together with qualitative guidelines for acceptance or rejection of load data with oscillations.

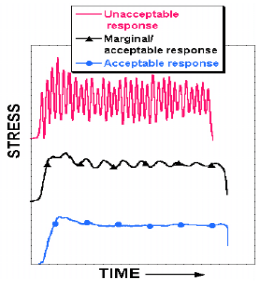

A) Acceptance guidelines for ringing in tests of metallic materials [44]

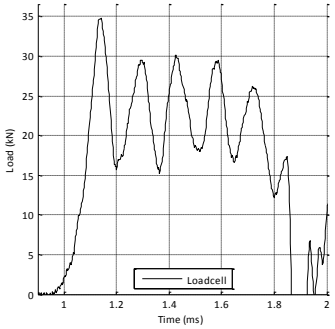

B) Output from a piezo electric loadcell for a test of steel at 10m/s (150/s) [43]

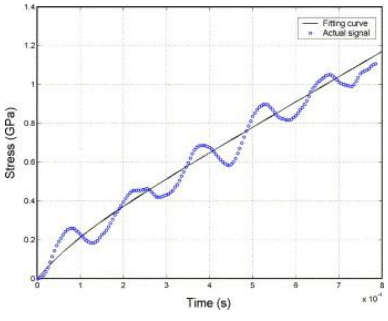

C) Test of GFRP at 10m/s with ringing in the load signal [28]

Figure 2.5 Examples of ringing and guideline for acceptance of ringing.

Some researches removes the oscillations by filtering of the data [28, 54], but filtering distorts the underlying load response of the specimen, and instead,

the oscillations should be minimized by other means before applying filtering [11]. Oscillations happen to all load cells with a mass. The piezo electric load cells are in favour due to their high resonance frequency. They can be used at high rates of loading without obscuring the load measurement too much, but the performance depends on the grip mass attached to the load cell [9, 52, 55]. The resonance frequency of the load-measuring device can be maximized for metallic materials by turning the test specimen into a load cell itself called a dynamometer. This arrangement also benefits from the close position to the strain measuring as it reduces the phase lag between the signals [1]. The dynamometer consists of a pair of strain gages mounted on an area on the specimen, which deform with a known calibrated elastic behaviour during the entire loading of the specimen. For metallic materials, the dynamometer is only calibrated in a load range up to the yield load of the specimen. Load measuring above the yield load relies on extrapolation of the calibration curve [1, 7]. Design recommendations for a dynamometer on dogbone specimens for metallic materials are given by Wood et al. [53]. The dynamometer is difficult to implement on FRP test specimens, since they are made as straight side specimens, which leaves no part of the specimen to be undamaged all the way up to fracture.

2.2 Numerical model

The entire setup with load cell, grips, slack adapter, rubber layers etc. and the piston rod constitutes the “load train”. For this work, the load train was viewed as a simple finite element system consisting of a connected set of masses and springs. Approach (a) and (c) in Figure 2.3 constitute the two main types of slack adapters and they were modelled to examine the influence of the mass distribution on the deformation rate of the test specimen. Figure 2.6 shows a schematic overview of the two systems along with the terms of concentrated masses (nodes) and the forces. Distributed masses were lumped to the concentrated masses.

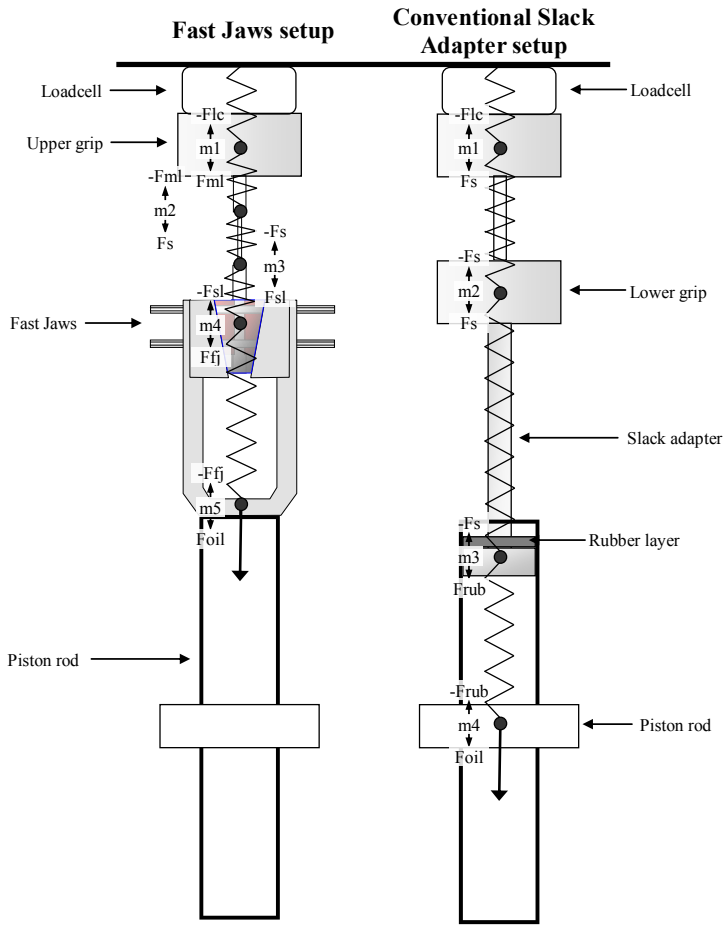

Figure 2.6 Schematic overview of slack adapters. Note the slack adapter is running inside the piston rod for the conventional slack adapter.

The systems were modelled as one-dimensional dynamic system with the following assumptions:

- A rubber layer was used to damp the impact between the two parts of the slack adapter (Only for the Conventional slack adapter).
- The piston rod was moving at constant velocity when the specimen was impacted.
- The entire oil pressure was lost over the valve at constant velocity.
- The piston rod had infinitely stiffness compared to the remaining parts of the load train.
- The load cell was mounted rigidly to the frame of the test machine.
- All masses were lumped.
- Grips were infinitely stiff.
- The specimen was rigidly connected to the grips.
- The fast Jaws frame was rigidly connected to the piston rod and moved with the piston rod as one unit.
- The Fast Jaws frame was deformable.

Each mass node had a displacement x, a velocity $\dot{x}$ and acceleration $\ddot{x}$. Newton second law were used to set up force equilibrium for each node and Table 2.1 gives the system of equations, which describe the movement of the individual nodes.

Table 2.1Mass distribution and equation systems for the slack adapter systems

Fast Jaws	Conventional slack adapter
m1 = Mass of upper grip and load cell m2 = Mass of mini load cell and specimen m3 = Mass of slack length of specimen m4 = Mass of preloading unit of the Fast Jaws m5 = Mass of Fast Jaws frame and piston rod	m1 = Mass of upper grip and load cell m2 = Mass of lower grip m3 = Mass of Slack adapter end m4 = Mass of piston rod
$m_1\ddot{x}_1 = F_{ml} - F_{lc}$ $m_2\ddot{x}_2 = F_s - F_{ml}$ $m_3\ddot{x}_3 = F_{sl} - F_s$ $m_4\ddot{x}_4 = F_{fj} - F_{sl}$ $m_5\ddot{x}_5 = F_{oil} - F_{fj}$	$m_1\ddot{x}_1 = F_{ml} - F_{lc}$ $m_2\ddot{x}_2 = F_{sla} - F_{ml}$ $m_3\ddot{x}_3 = F_{rub} - F_{sla}$ $m_4\ddot{x}_4 = F_{oil} - F_{rub}$

F_{lc} = Force of the load cell
F_{ml} = Force of local dynamometer
F_s = Force of specimen
F_{sl} = Force of slack end of specimen
F_{sla} = Force of slack adapter
F_{fj} = Force of Fast Jaws frame
F_{Rub} = Force of Rubber damper
F_{oil} = Force on the piston rod from the hydraulic oil

Parameters

K_{lc} = Stiffness of the load cell
A_s = Cross sectional area of the specimen
E_s = Elastic modulus of the specimen
L_s = Gage length of the specimen
K_{ml} = Stiffness of the dynamometer
K_{sl} = Stiffness of the slack length of specimen
K_{sla} = Stiffness of the slack adapter
K_{sl} = Stiffness of the Fast Jaws frame
σ_y = Yield stress
ε_y = Yield strain
n = Hardening parameter
V = Piston rod velocity
A_p = Piston rod pressurised area
Q = Flow rate
P = Pressure drop
Q_N = Rated flow rate
P_N = Rated pressure drop
σ_R = nominal stress in rubber
C = Neo Hookian law – material constant
λ = Stretch ratio
L_R = Thickness of rubber damper
A_R = Cross sectional area of rubber damper

A Kistler 9071 Piezo electric load cell were considered as load cell which had a stiffness in the loading direction of K_{LC} = 26e9 N/m. The force in the load cell was calculated solely from the displacement of node 1 as the load cell was rigidly connected to the test machine. The force became

$$F_{LC} = K_{LC}x_1 \tag{2.2}$$

Two types of specimens were considered: linear elastic, and an elasto-plastic material. The linear elastic force response of both types of specimens were calculated with

$$Fs = K_s(x_2 - x_1) \tag{2.3}$$

Where K_s is defined as

$$K_s = \frac{A_s E_s}{L_s} \tag{2.4}$$

The plastic force response of the elasto-plastic specimen were calculated by a rate independent

power law

$$Fs = A_s \sigma_y \left(\frac{\varepsilon}{\varepsilon_y}\right)^n \tag{2.5}$$

Equation (2.5) is only valid for a monotonic rising load. The non-reversible process in the specimen, which occurs during an unloading phase, was represented with the algorithm in Appendix D.

F_{ml},F_{sl},$F_{sla\ and}$ F_{fj} were formulated as the linear elastic response in equations (2.3) and (2.4). The rubber damping were described with a one dimensional Neo Hookian law (Hyper elastic material) formulated as

$$F_{Rub} = A_R C \left(\lambda - \frac{1}{\lambda^2}\right) \tag{2.6}$$

The deformation measure for this law was the stretch ratio calculated as

$$\lambda = \frac{l}{L_R} \tag{2.7}$$

l is the length after deformation and L_R is the original length. In terms of node displacement for the conventional slack adapter, equation (2.7) yield

$$\lambda = \frac{L_R - (x_4 - x_3)}{L_R} \tag{2.8}$$

Since the slack adapter is running inside the piston rod as shown in Figure 2.6 the rubber becomes compressed when $(x_4 - x_3)>0$. To create a compressive force in the rubber when $(x_4 - x_3)>0$, $(x_4 - x_3)$ were subtracted from the initial thickness instead of added as given in equation (2.8). The rubber damper is not rigidly connected to the piston rod or the slack adapter so the rubber could only exert compressive forces to the system. In the model this was imposed by setting F_{Rub} to 0 when $(x_4 - x_3)<0$. As explained later, the system of equation were solved with a explicit time stepping algorithm and in some occasion the step forward in time could result in $(x_4 - x_3)>L_R$ which corresponded to a final negative thickness. In this case the system were penalised by setting λ in equation (2.6) to

$$\lambda = 0.001 \tag{2.9}$$

The force exerted to the system by the oil pressure over the piston rod was calculated from the assumption of complete pressure loss in the actuator at constant velocity. The oil flow Q into the cylinder was related to the piston rod velocity V by:

$$V = \frac{Q}{A_p} \tag{2.10}$$

Inserting equation (2.10) into (2.1) yields

$$P = \frac{P_N}{{V_N}^2} V^2 \tag{2.11}$$

The high-speed servo-hydraulic test machine was operated in open loop so the valve was opened and kept open. The oil flow would then change until the pressure differential over the piston rod was zero. When the specimen was impacted at constant velocity the piston rod was slowed down and the flow rate decreased. The resulting net differential pressure over the piston rod then exerted a force on the system. When the valve was set to a given opening, a constant velocity V_N was obtained with the pressure drop P_N corresponding to the system pressure. The pressure drop at any velocity V could be calculated from equation (2.11). If the velocity was $V_{x1,}$ equation (2.11) gives a pressure drop P_{x1} and if the velocity is V_{x2} the associated pressure drop is P_{x2}. Changing the

velocity from V_{x1} to V_{x2} gives the following pressure drop over the valve

$$dP = P_{x1} - P_{x2} \tag{2.12}$$

This dP was the differential pressure over the piston rod, causing a force to the system as

$$dF_{oil} = A_p dP \tag{2.13}$$

Combining equations (2.11), (2.12) and (2.13) yields

$$dF_{oil} = A_p \frac{P_N}{{V_N}^2}\left({V_{x1}}^2 - {V_{x2}}^2\right) \tag{2.14}$$

In a simulation the impact velocity V_{x1} would be the initial constant velocity of the piston rod before the specimen impact such that

$$V_{x1} = V_N \tag{2.15}$$

Combining equations (2.14) and (2.15) and exchanging V_{x2} to the piston rod velocity $\dot{x}_i$ yields

$$dF_{oil} = A_p \frac{P_N}{{V_N}^2}\left({V_N}^2 - {\dot{x}_i}^2\right) \tag{2.16}$$

When $\dot{x}_i$ is negative, the piston rod moves in the opposite direction of the initial movement and oil would be forced backward in the system. The full pressure will build up quickly, and and in this case F_{oil} is set to $A_p P_N$.

The explicit ODE45 solver in MatLab was used to solve the differential equations for displacement, velocities and accelerations.

2.3 Verification of models

The conventional slack adapter model was used for verification. A modified MTS high-speed machine equipped with a conventional slack adapter was used for comparison. The test machine is described in chapter 3.

First, a hypothetically case was simulated. Figure 2.7A shows the simulation where the slack adapter impacts an infinitely strong linear elastic specimen at 20 m/s. The piston rod was given an acceleration length of 230mm and a maximum velocity of 20m/s. First, the piston rod accelerated and at point 1 the piston rod impact the slack adapter, and the slack adapter and lower grips moved along with it. At point two, the specimen had stopped the piston rod, but the momentum of the piston rod forced the specimen to a strain where the specimen exerted a larger force than the force of the oil. The piston rod was pulled back and when the specimen reached zero strain at point 3 it went to compression and stopped applying force to the piston rod. The piston rod continued due to the non-rigid connection between the piston rod and slack adapter, and the force of the rubber damper was set to zero. The piston rod was then deaccelerated by the oil pressure and bounces back again. This process continued as damped oscillations until equilibrium between the force and oil force was reached. The damping occurred due to the constant force of the oil when the velocity of the piston rod was negative Figure 2.7B shows a comparison between a simulated acceleration curve of the piston rod and a measured curve. The comparison showed good agreement between the final velocities before impact of the slack adapter. However, the path to the final velocities differed. The difference was accounted to the effect of internal friction in the cylinder and the opening time of the valves. The valves used here was two Moog D665 with a valve opening time of 10-15ms [50]. None of these two effects were taken into account.

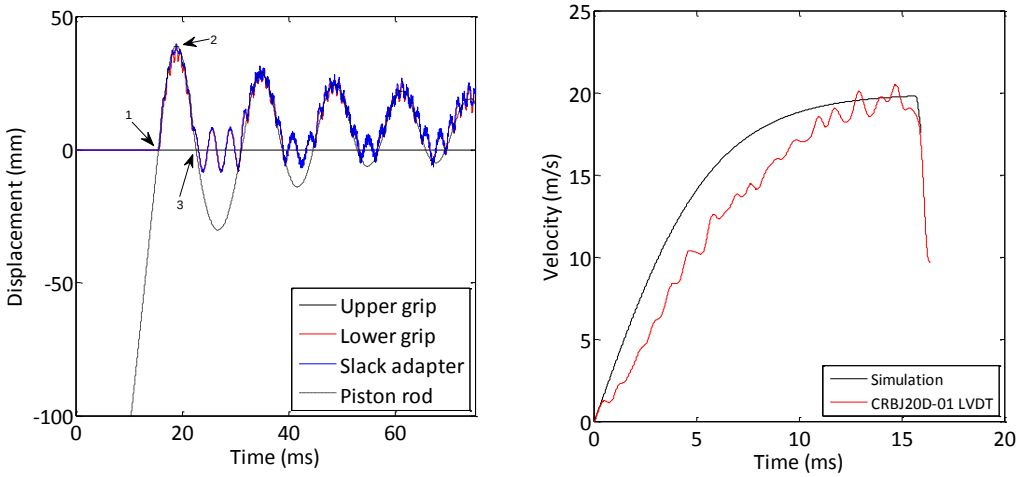

A) Simulation of conventional slack adapter. 1 is the impact between the piston rod and the slack adapter. At 2 the piston rod was brought to zero velocity by the infinitely strong test specimen. At 3 the contact between the specimen and piston rod is lost.

B) Comparison of simulated and measured velocity of the piston rod.

Figure 2.7 Simulation of the conventional slack adapter.

The model was compared to a series of test of UD Eglass/Epoxy specimens tested at 7.5 and 20 m/s. The specimen parameters are given in Table 2.4 and Figure 2.8 shows the specimen design. Appendix F gives the parameter values for the simulation, which was used for the comparison with the tests.

Table 2.2 Specimen parameters for comparison tests

Parameter	Description	Value
Esp	Elastic modulus of the specimen	42 GPa
Asp	Specimen cross sectional area	15 mm^2
L_s	Specimen gage length	50mm

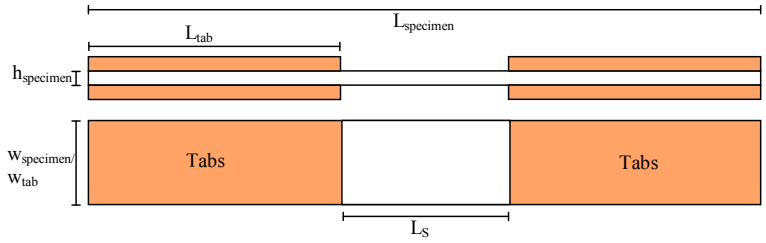

Figure 2.8 Schematic specimen design

A set of custom grips made from high strength aluminium was used for gripping the specimen . Load was measured with a Kistler 9071 Piezo electric load cell.

Figure 2.9A shows a comparison between the test and the model for the strain vs. strainrate response. In the simulation, the strain rate increased immediately, while in the real test the strain rate raises slowly and then accelerate. Figure 2.9B shows the specimen strain plotted against the piston rod position with a free travel of 185mm before impact.

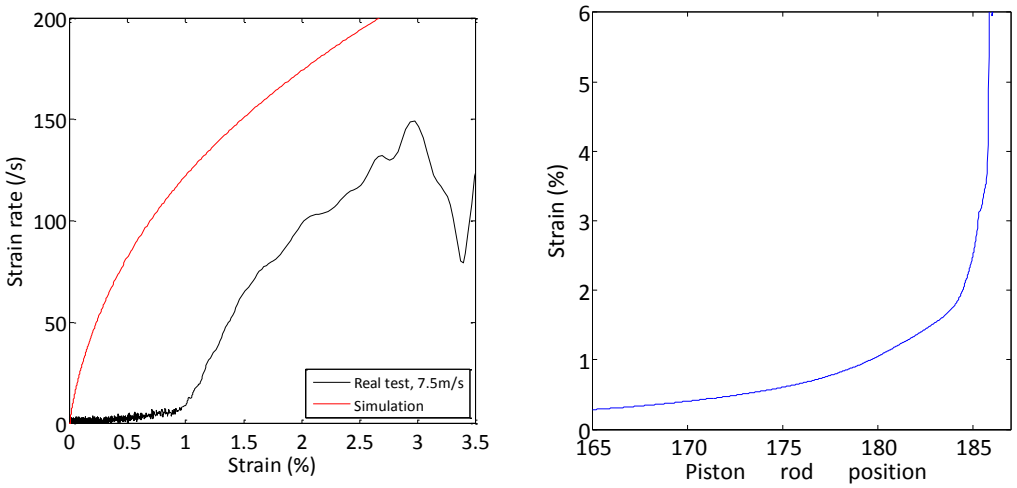

A) Specimen strain vs. strainrate *B) Specimen strain versus piston rod position*

Figure 2.9 Simulation and test of linear elastic material of straight side coupon specimen with cross section =15mm^2, Esp = 38GPa and Lg =50mm.

The plot reveals that the specimen strain up to 1% was built up only 15 - 25mm before impact with a slowly exponential increase in strain rate. The strain may be a result of friction or trapped air between the piston rod and slack adapter. Friction would most likely set of from the start of the piston rod movement and would not build up towards the ending, unless the slack adapter became progressively skew towards the impact end. Such defects on the slack adapter were not observed. Trapped air could cause the observed effect. To check if the observed effect could be trapped air, the model was enhanced to predict the pressure rise inside the slack adapter as the piston rod moved. The model is presented in Appendix C. The model handles the compressibility of the air and models the outflow of air together with the pressure increase in the slack adapter. Any size of outlet holes/leakage could be handled. The model output a force as function of the piston rod position to a given time and model was implemented in the slack adapter model by adding the force to the rubber and the piston rod. Trapped air would act against these parts of the load train. The air was able to escape between the moving parts in the comparison tests and the escape cross sectional area was estimated to around 15mm^2. The initial air pressure in the slack adapter was set to one atm. Figure 2.10 shows a comparison between a simulation and a test at 7.5 m/s impact velocity. The air inclusion created the effect of slowly rising strain rate and a following rapid increase. However, the air compression model does not account fully for the effect, but the model was still found to describe the behaviour of the slack adapter reasonable accurate.

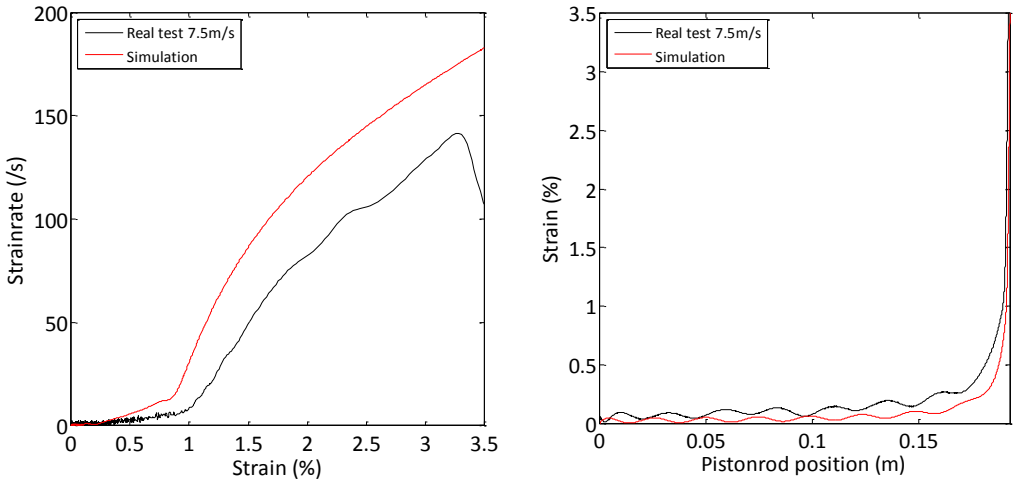

A) Strain rate vs strain with air inclusion simulated *B) Specimen strain vs piston rod position*

Figure 2.10 Comparison between simulation and real test with air model included. The pressure was added as pressure on the rubber and on the piston rod.

2.4 Examination of stress and strain rate response

Simulations were carried out to examine how the stress-strain curves are affected by the dynamic loading conditions and then how the strain rate developed in the specimen as function of the deformation history. The stress in the specimen was calculated by dividing the force of the load cell with the initial cross sectional area of the specimen. In a real test, the strain would be measured directly on the specimen with a strain gage or non-contact measurement methods. In the simulations, the strain was calculated by dividing the elongation of the specimen with the initial gage length. The deformation applied to the specimen was calculated as the displacement between the two nodes surrounding the specimen. Further, also the forces in the slack adapter were examined as the high acceleration forces could lead to destructive loading of the slack adapter system. The effect of the missing rigid connection in the slack adapter was also studied. Four setups were considered:

1. Conventional slack adapter – without any damping
2. Conventional slack adapter – with 3 mm rubber damper
3. Conventional slack adapter – with 3 mm rubber damper and air damping (fully closed volume)
4. Fast Jaws system.

A linear elastic specimen was considered and the specimen parameters are given in Table 2.3. Other parameters are given in Appendix F. The specimen design for the conventional slack adapter is shown in Figure 2.9 while the specimen design for the Fast Jaws system is shown in Figure 2.13. The model of the Fast Jaw setup were adjusted such that the specimen "slack end" was accelerated to piston rod velocity in less than 15 µs, which corresponded to the acceleration time reported in literature [12].

Table 2.3 Specimen parameters and their nominal values

Parameter	Parameter	Elastic specimen	Elasto plastic specimen	Varied
Esp	Elastic modulus	42 GPa	200 GPa	x
Asp	Specimen cross sectional area	15 mm^2	15 mm^2	x
Lsp	Specimen gage length	50mm	50mm	x
σ_y	Yield strength	-	800 MPa	-
N	Hardening exponent	-	0.01	-
ε_f	Termination strain	3.5%	50%	-

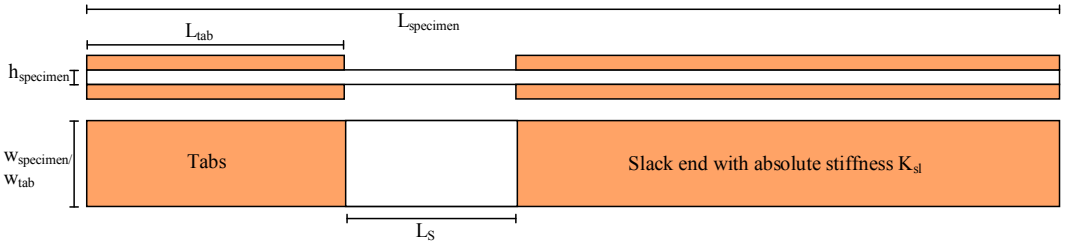

Figure 2.11 Specimen design used in the simulations of the Fast Jaws

The simulated stress strain-curves is shown in Figure 2.12A. The error in Figure 2.12B is the difference between the calculated stress in the simulation and a perfect elastic response of the specimen.

The conventional slack adapter with or without damping gave similar result for the simulated stress-strain curve. The measured stresses were below the perfect linear response and an increased damping gave a smaller error. The plot showed also that the error stabilised with increasing strain.

The linear elastic response of the specimen causes the force to increase constantly with an increasing deformation. Due to the inertia of the load cell and upper grip the force measured with the load cell constantly lacks after the actual load in the specimen, which causes the stabilised error. The higher air damping caused a higher initial strain on the specimen before the specimen was accelerated and the air damping thereby caused a lower stress "lack".

For the fast Jaws system, the error varied in a different way. In this model, there was no lower heavy grip to accelerate together with the specimen. The specimen was then loaded much quicker, which caused the resonance wave in the stress measurement. In this case, the loading was too fast and excited the resonance frequency of the simulated load cell/grip arrangement.

Figure 2.12A also showed that the beginning of the stress-strain curve is not linear. If the elastic modulus was estimated with respect to ASTM 3039 [56], the recommended data in the strain range 0.1 – 0.3% would be obscured by the load cell resonance. The effect would be a too low estimated elastic modulus. The error could be minimized by selecting a strain range, which was less affected. However, that would require the materials to behave perfect linear elastic, before a fair comparison could be made to quasi-static test, with the elastic modulus estimated in the recommended strain range.

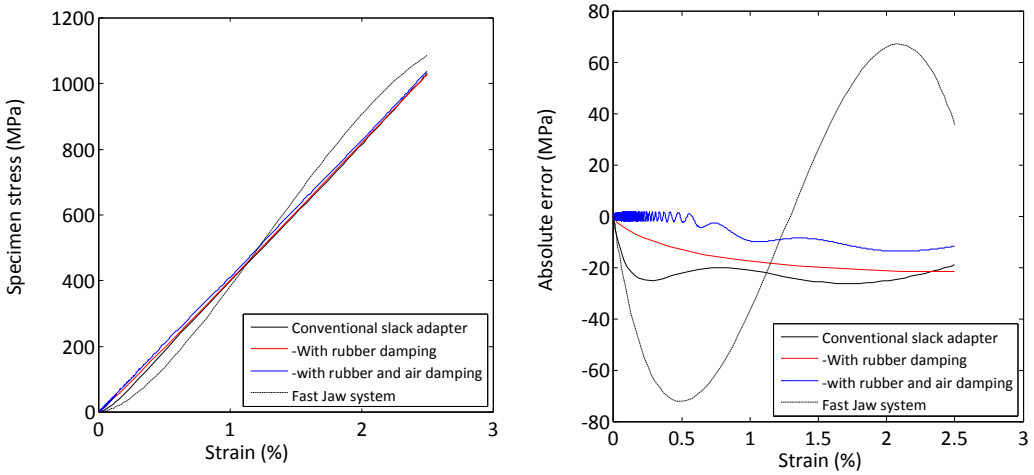

A) Stress strain curves

B) absolute error compared to perfect linear elastic relationship

Figure 2.12 Simulation of stress strain curves for piston rod velocity of 20 m/s

Care should be taken when comparing elastic modulus obtained at high impact speed and obtained at quasi-static conditions and these findings suggest that this kind of testing is unsuitable for estimation of the elastic modulus.

Figure 2.13A shows the strain-rate vs strain plots for the simulations in Figure 2.12. For the conventional slack adapter, the strain rate was rising through the entire deformation. This happened since the lower grip never attained a constant velocity before the specimen reached its fracture strain. This damping was enhanced by the rubber and air damping, which amplified the problem due their lower accelerations of the lower grip.

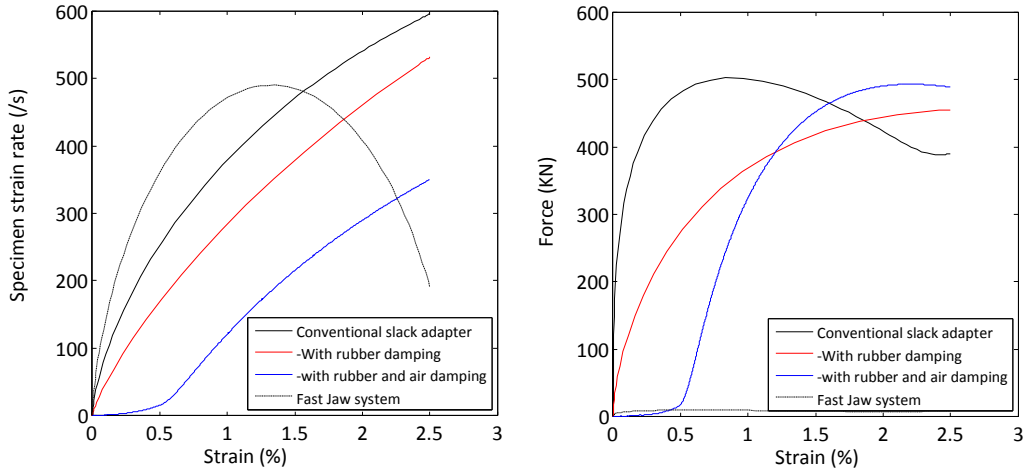

A) Strain rate

B) Force in the slack adapter. For the Fast Jaw system the force was calculated in the long slender part of the specimen.

Figure 2.13 Strain rate and force in the system.

The observation of non-constant strain rate was reported in literature for the conventional slack

adapter, where a thicker rubber layer was suggested [57]. However, this modelling suggested that a thicker rubber layer would damp the maximum strain rate further without making it constant. For the Fast Jaws the strain rate increased faster due to the lack of inertial damping, however the strain rate was not steady, but became a function of the oscillations introduced in the entire system.
Figure 2.13B shows the forces in the slack adapter vs. strain. For the conventional slack adapter the maximum force were approximately the same, but the time the force peaked were different. In the case of the combined rubber and air damping the air pressure had already compressed the rubber so the final impact became harder than the case with the rubber alone. If the slack adapter is too weak to withstand these forces, it would fail before any substantial forces are transferred to the specimen. For the Fast Jaw system, the force in the slack length of the specimen is low, due to low masses in the system.
A bouncing effect in the specimen displacement rate due to the non-rigid connection between the specimen and the slack adapter has been reported in litterature [12, 13]. This bouncing effect was caught by the model and is shown in Figure 2.14. The simulations revealed that the period of the bouncing was long enough, so the specimens failed within the first bounce. In this case, the specimen displacement rate becomes a function of the impact mechanism in the slack adapter and not only a function of the piston rod velocity.

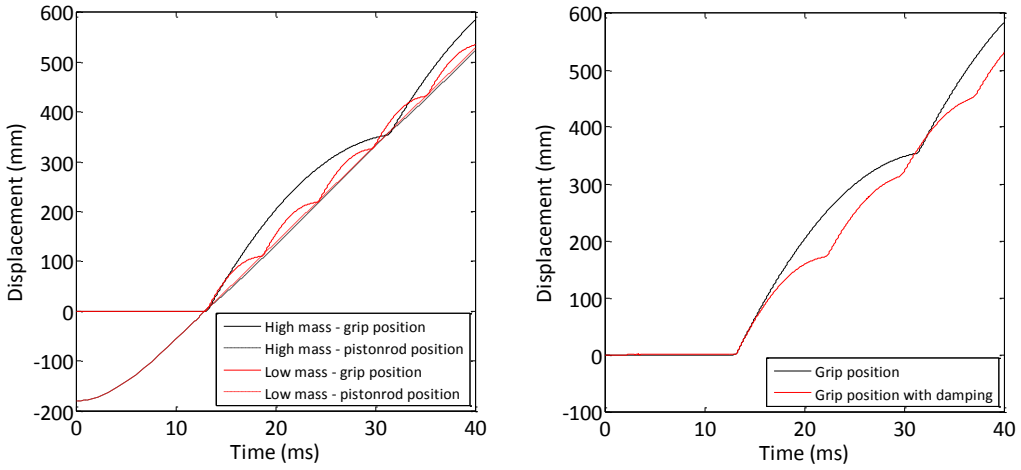

A) Bouncing effect for high and low grip mass. A rubber layer is included as damping element for both the high and low mass simulation.

B) Effect of additional air damping on the bouncing effect

Figure 2.14 The bouncing effect because of no rigid connection between the slack adapter and the specimen. In figure B additional damping was added by inclusion of air in the slack adapter.

2.4.1 Parameteric study

The model of the conventional slack adapter was used for a parameter study to examine the effect of the load train parameters on the achieved strain rate in the specimen. The parametric study was carried out by varying the different parameters of the model individually and calculating the resulting average strain rate and the standard deviation in the interval $[0.5\varepsilon_f : \varepsilon_f]$ where ε_f were the termination strain of the simulation. The parameters were varied according to

$$\boldsymbol{x} = Par * [0.1, 0.5, 0.75, 1, 1.5, 2, 3, 5] \tag{2.17}$$

x was the vector of values used in the simulations; "Par" was the nominal value of the parameter and the values in the square bracket were the multiplication factors to the nominal value. The parameters, are given in Table 2.4 along with their nominal values.

Table 2.4 Parameter description and their nominal values.

Parameter	Description	Nominal value
Lr	Rubber thickness	3 mm
C1	Rubber shear stiffness	25MPa
Ls	Slack adapter length	190 mm
As	Slack adapter cross sectional area	452 mm^2
Es	Slack adapter elastic modulus	200 GPa
M1	Load cell grip mass	1.83 kg
M2	Moving grip mass	2.4 kg
M3	Piston rod mass	33 kg
Ag	Cross sectional area, where air escapes in the slack adapter	5 mm^2

The impact velocity was set to 2 and 20 m/s and the system pressure was set to 270 bars. The final velocity at 270 bar pressure drop would then be 2 or 20m/s respectively. Both a linear elastic and elasto plastic specimen were used for the simulations, and the parameters of the specimens are given in Table 2.3. An elasto plastic specimen was included to compare how the varied parameters may influence the specimen deformation differently dependent on the material response.
Figure 2.15 shows the normalised strain rate for the conventional slack adapter impacted at 20 m/s. The x axis is the normalised factor of the parameter in question, e.g. a factor of two for the loadcell grip mass M1 correspond to 2*M1.The y axis is the normalised strain rate. All strain rates were normalized with the average strain rate obtained with nominal parameters. The three factors with the largest influence on the average strain rate were the specimen length, the slack adapter stiffness and the slack adapter cross sectional area. To maximize the average strain rate the absolute stiffness of the slack adapter should be increased. Further the lower grip mass should also be minimised.

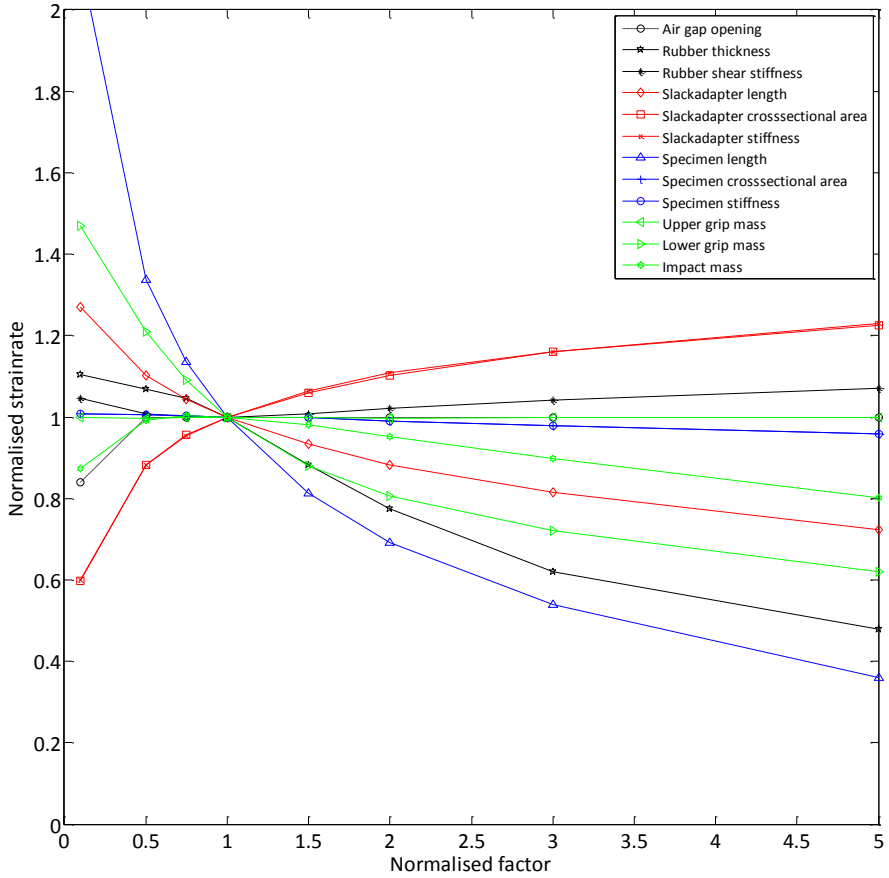

Figure 2.15 Parameter study of classical slack adapter setup. The largest effect on the strain rates are found from the specimen length and cross sectional area of the slack adapter. Impact velocity 20 m/s.

In Figure 2.16 the normalised strain rate is shown for an impact velocity of 2 m/s. The lower impact energy changed the important parameters for the achieved strain rate. The strain rate primarily depended on the specimen parameters due to the lower acceleration forces associated with the lower velocity. The lower grip mass had a decreasing effect on the average strain rate with decreasing weight, while for the 20m/s the lower grip mass had increasing effect for a decreasing weight.

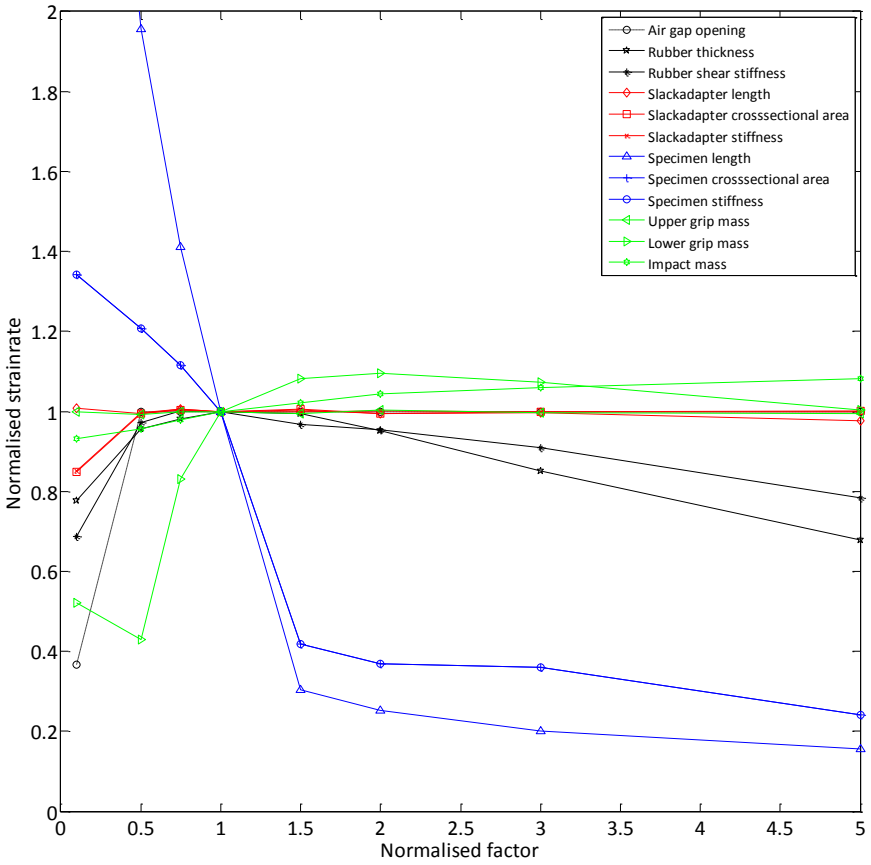

Figure 2.16 Parameter study of classical slack adapter setup. Impact velocity 2 m/s.

For comparison an elasto plastic specimen were also simulated and the result is shown in Figure 2.17. Here the gage length were the dominant factor for the resulting strain rate. The impact mass were seen to decrease the strain rate at higher masses, which is counter intuitive, but the reason is because the acceleration length was kept fixed so the heavy mass could not reach full velocity before impact. This was seen in the parameters studies for the linear specimens as well. If the acceleration length is adjusted so the heavier impact mass can reach full velocity before impact the influence disappears.

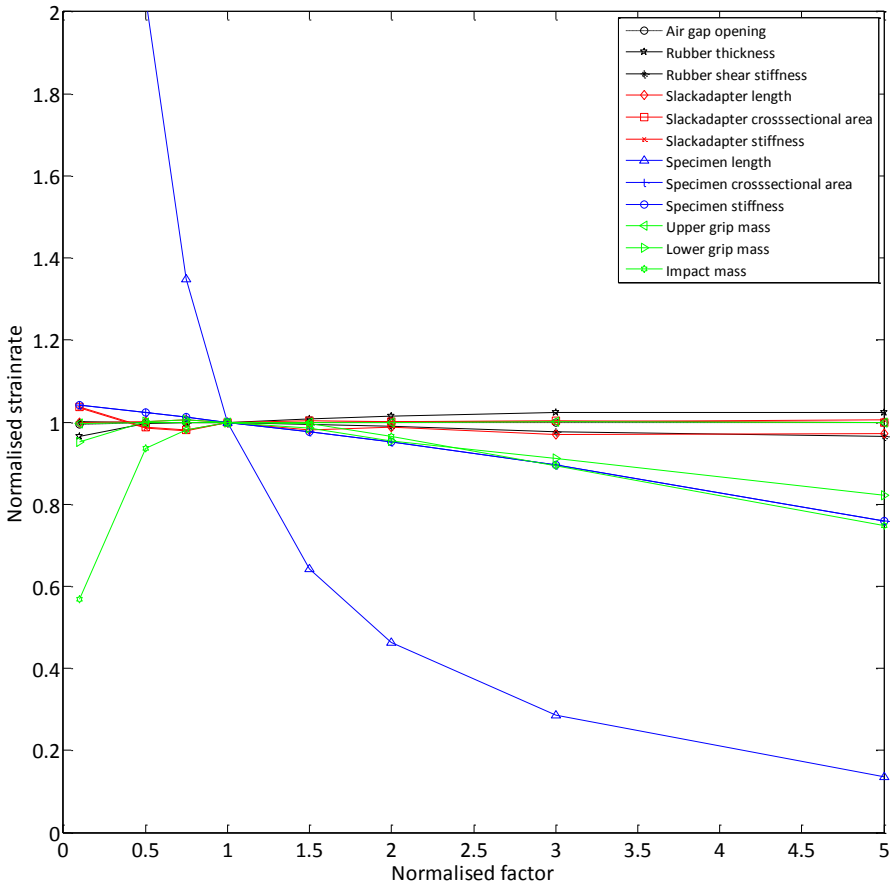

Figure 2.17Parameter study for elastic plastic specimen. Impact velocity 20m/s

2.5 Summary

A model was presented to simulate the load train of a high speed servo hydraulic test machine. The influence of the load train on the test results was examined and a series of conclusions could be drawn from the modelling:

- A linear elastic specimen cannot be deformed with a constant velocity in the high-speed servo hydraulic test machine due to inertial effects.
- There is no differential pressure to apply a force to a specimen when the piston rod moves at constant velocity.
- The deformation velocity transferred to the specimen was controlled by the mass of the moving grip. In the case of the conventional slack adapter, which had a high moving grip mass the velocity was constantly changing with the acceleration and deceleration of the moving grip. For a Fast Jaw setup there was no lower moving grip, however the transferred velocity was controlled by the elasticity of the slack length of the specimen and in this case the velocity will neither be constant for linear elastic specimens.
- For the conventional slack adapter the specimen failed within the first bounce of the bouncing effect. For metal testing bouncing could lead to a load/ unload condition.
- The rigid connection created with the Fast Jaw system, combined with the fast gripping mechanism, lead to oscillations in the load cell before fracture of the linear elastic specimen.

- Trapped air in the slack adapter caused high loading on the specimen before it was accelerated. This could cause weak specimens to fracture before a high strain rate was reached.

3 Design and construction of a High-Speed Servo-Hydraulic Test Machine

The design and construction of a high-speed servo-hydraulic test machine (HS machine) is described in this chapter. Chapter 2 describes the concept and working method of the HS machine and this chapter describes the construction of a high speed servo hydraulic testmachin test machine. Guidelines for the design process are developed, including the design of test specimens. The machine was built with a limited budget so where possible existing equipment was rebuild and reused for this purpose.

3.1 Design

The HS machine was divided into five design elements as shown in Figure 3.1, and the design elements are described in the subsequent sections. Figure 3.1 also shows the conceptual setup of a HS machine, where the main difference from a standard servo hydraulic test machine is the introduction of the "lost motion unit". The other main difference, not shown in the figure, was the use of open loop control with no control of the piston rod position.

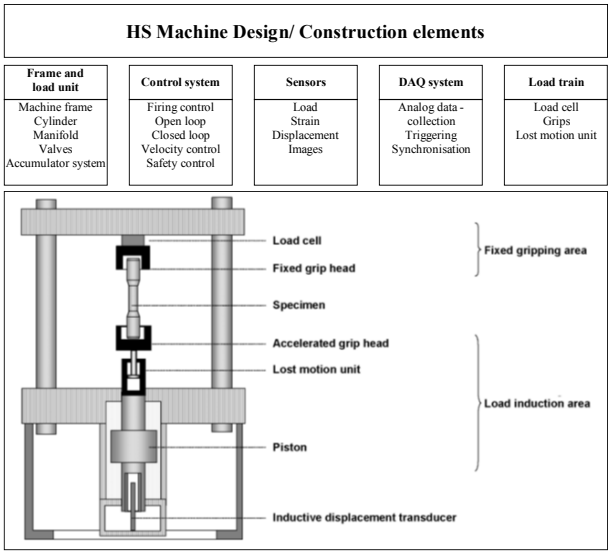

Figure 3.1 Design modules for design and construction of the HS machine. Illustration from [1].

The performance requirements for the machine were set in Table 3.1.

Table 3.1 Performance requirements

Parameter	Value
Static force	>100 kN
Maximum velocity	>20m/s
Acceleration length	0.2m
Working length	0.1m
Function	Doubled ended piston rod. Must handle Tension and compression
Payload	20kg

The static force is the force delivered at maximum system pressure. The maximum velocity is the velocity the piston rod achieves within the given acceleration length. The acceleration length was set to 0.2m to maintain a stiff load train, but also to account for the weight penalty on the piston rod from a long stroke. The working length is the remaining stroke when the piston rod has reached constant velocity.
A payload of 20kg was added to the design weight to be accelerated to be sure the machine would be able to accelerate the added grip system. Further, the machine should handle both tension and compression loadings.

3.2 Frame and load unit

The hydraulic load unit consisted of the following parts

- Cylinder
- Manifold
- Hydraulic valves
- Accumulator system

The cylinder and manifold were designed in cooperation with the Swedish companies Industri hydraulik SE (Manifold) and Argos SE (Cylinder).
Standard servo hydraulic test machines operate with a system pressure of 210 bars. If the system pressure is increased to, for example, 280 bars then moving parts could be smaller while maintaining the output force. Based on the availability of valves the system pressure was set to maximum 280 bars with a minimum working pressure of 250 bars.
The initial cylinder design from Argos indicated a piston rod mass of about 35 kg. With a payload of 20kg, the total accelerated mass became 55kg. As described in chapter 2 the pressure decreases with increased flow through the valve and the acceleration force decreases. Combining Newton's second law and equation (2.16), yield the following relationship between the piston rod velocity $\dot{x}$, and acceleration $\ddot{x}$

$$\ddot{x}_i = \frac{A_p}{M}\frac{P_N}{{V_N}^2}\left({V_N}^2 - {\dot{x}_i}^2\right) \tag{3.1}$$

Equation (3.1) was solved for x, $\dot{x}$ and $\ddot{x}$ with MatLab's Ode45 solver. V_n was defined as the velocity where all the pressure P_n in the valve was lost and A_p was defined as the pressurised area. For this design A_p was fixed to 4778mm^2. Figure 3.2 shows piston velocity vs. piston displacement for this configuration for different velocities V_n. A configuration with Vn slightly above 20m/s would reach close to a constant velocity of 20 m/s at $x = 0.2m$.

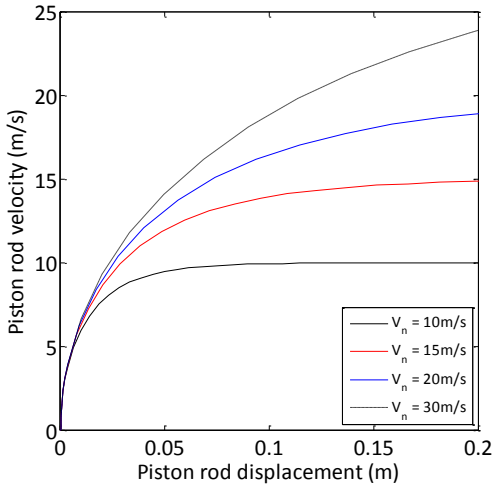

Figure 3.2 Velocity profile of the piston rod as function of the displacement. M = 55kg. A_p= 4778mm^2. P_n = 280 bar.

A piston rod velocity of 20m/s corresponds to a flow rate of 5734 l/min for A_p = 4778mm^2, and the minimum flow requirement for the valve selection was set to 5800 l/min.

The total oil flow during the valve opening must be less than the total cylinder volume to finish the piston rod acceleration before the piston rod reaches the end cushion. A linear relationship was assumed between the opening of the valve and the flow, such that a 50% valve opening gave 50% of the maximum flow. Assuming incompressibility of the oil, the piston rod velocity was calculated from the pressurised area A_p and the flow rate Q as

$$\dot{x} = \frac{Q}{A_p} \tag{3.2}$$

The acceleration length of the piston rod was set to x_{acc} and the oil flow acceleration was assumed constant. The maximum opening time was then calculated from

$$t_{open} = \frac{2A_p x_{acc}}{Q_{max}} \tag{3.3}$$

Q_{max} is the maximum flow rate resembling the flow rate at constant velocity of the piston rod and full pressure loss. Figure 3.3 shows relationship between valve maximum flow rate, the acceleration length, the piston rod velocity, and the maximum valve opening time. With a flow rate of 5800 l/min, the maximum opening time was found to be 21ms for an acceleration length x_{acc} of 0.2m.

No commercial valve rated for a maximum flow of 5800 l/min or higher is available, so two Moog D665 valves was chosen. The Moog D665 valve is rated at 1500 l/min for a pressure drop of 10 bars, and with a maximum flow rate of 3600 l/min at 58 bar pressure drop. The response time to 100% opening is 12ms with a stub shaft spool configuration.

The Moog D665 valve can be used for open loop control as well as closed loop control. However, the high flow rate make the D665 unsuitable for close loop control of the piston rod. Instead, a MTS 256.09 servo valve was selected to drive the machine in closed loop control for positioning the piston rod before testing. A_p = 4778mm^2 corresponds to a force of 121kN at 250 bar and 135kN at 280 bar.

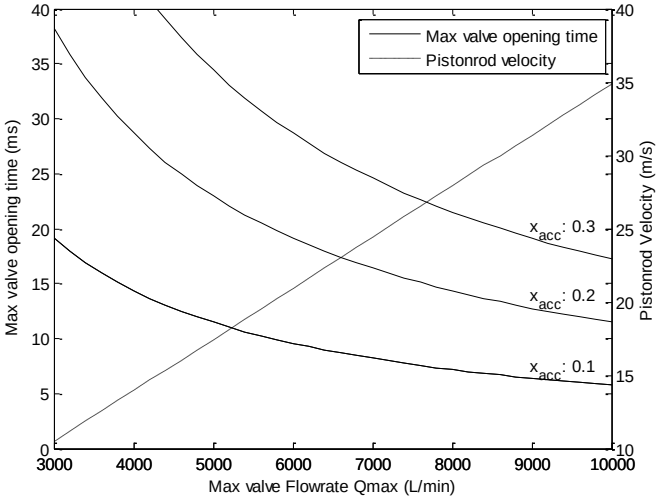

Figure 3.3 Valve selection chart – x_{acc} is the acceleration length to full flow rate. A_p = 4778mm^2

The cylinder was designed for a dynamic stroke of 330mm, which covered both the required acceleration length of 0.2m and the working length of 0.10 m. The full stroke was 608mm which includes end cushions and clearance stroke for the inlet ports.

The accumulator system was designed to deliver an oil volume of $V_R = A_p \cdot 330mm = 1.6l$ from a maximum pressure of P_2 = 280 bars to a minimum pressure of P_1 = 250 bars and at flow rates up to 7200 l/min. The 7200 l/min was chosen to accommodate the full potential of the valves. With an assumption of adiabatic expansion of the gas the required nominal accumulator volume V_0 is given by [58]

$$V_0 = \frac{V_R}{\left(\frac{P_0}{P_1}\right)^{\frac{1}{\gamma}} + \left(\frac{P_0}{P_2}\right)^{\frac{1}{\gamma}}} C_a \tag{3.4}$$

C_a is a correction constant with respect to the adiabatic process, γ = 1.4 is the adiabatic constant of the gas in accumulator and P_0 is the gas pressure in the accumulator before oil pressure was applied. With C_a = 1.4 and P_0 = 180 bars, V_0 is 36.4l. From these requirements, the Hydac SB330 H10 accumulator was selected. This accumulator has a nominal volume V_0 of 10l and a rated flow rate of 30l/s. Four accumulators were used on the pressure side in parallel connection to accommodate the full flow of $4 \cdot 120\text{l/s} = 7200\text{l/min}$ and to obtain a total nominal volume of 40l. Additional four accumulators were placed at the return side of the cylinder to absorb the oil and suppress pressure spikes in the system. The gas pre-pressure P_0 was set to two bars. The cylinder and manifold were designed with a port size of Ø80mm in areas where the full flow of 7200l/min would occur. Ø80mm equals an area of 5026mm^2, so the port diameter was designed larger than the pressurised area A_p = 4778mm^2 in the cylinder.

The cylinder was designed with end cushions to smoothly stop the piston rod at the ends. Due to the high piston rod velocities and the open loop control, it was impossible to stop the piston rod by closing the valves, so the end cushions were designed to absorb the full kinetic energy of the piston rod. The end cushions consisted of a chamber fitted with relief valves, where the piston rod moved into at the end of the stroke. Inside the end cushions champers, the piston rod has to compress the trapped oil out through the relief valves. Argos designed the end cushions to a 104MPa working pressure and an maximum pressure of 125MPa. With a pressure of 104MPa the maximum dynamic force was calculated to

$$Fd = 104MPa * 4778mm^2 = 496kN \quad (3.5)$$

This load distributes though the machine and into the support and fundament of the machine, and the dimensioning dynamic force was set to 500kN.

3.2.1 Machine Frame and support frame

A frame from an older MTS servo-hydraulic test machine was available to accommodate the custom designed manifold and cylinder. Figure 3.4A shows a sketch of the frame and Figure 3.4B shows the frame with the original cylinder removed. The frame was modified to support the new manifold and cylinder, such that the impact forces are transferred from the cylinder to the frame and the lab floor. The machine had a total height of 4.7 meters and had to be lowered into the lab floor to obtain a feasible working height.

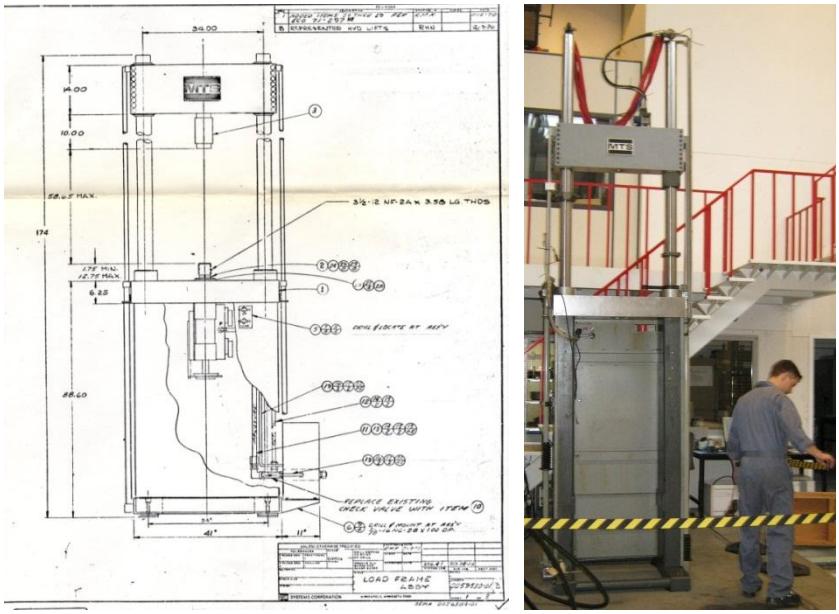

A) Drawing from the original documentation

B) Frame with the original cylinder removed.

Figure 3.4 Frame available to build a high speed servo hydraulic test machine

The entire machine frame and the cylinder and manifold were drawn as a 3D model, which was used to design the modifications of the machine frame. Figure 3.5A shows the 3D model. A support frame was constructed to create a platform for the test machine and to direct the impact forces to the strongest part of the lab floor. Figure 3.5B shows the frame in the 3D model together with a securing cage around the machine.

The weight of the designed manifold and cylinder was about 2.5 tons and the weight of the machine frame was 2 tons. The maximum load on the support frame is 500kN + 25kN + 20kN = 545kN. Due to uncertainties in the actual dynamic pressure the design load was set to 650kN and the safety factors in the steel construction standard DS412 [59] was used for dimensioning the support frame.

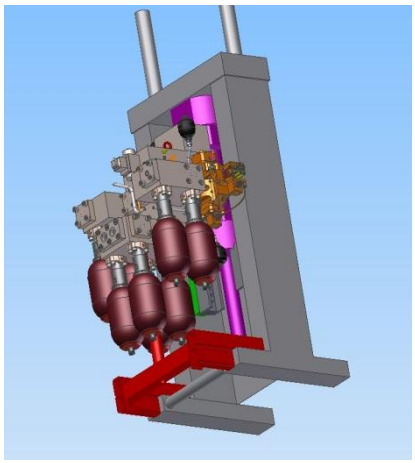

A) 3D model of the manifold and cylinder installed in the frame.

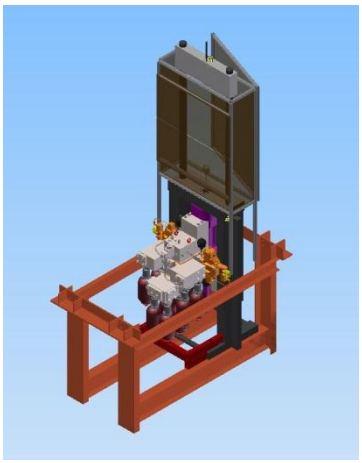

B) 3D model of the full test machine including support frame to fit the machine into the lab floor.

Figure 3.5 3D model of the test machine

Figure 3.6A shows the installation of the complete manifold and cylinder into the machine frame. Figure 3.6B shows the installation of the support frame into the lab floor and Figure 3.6C shows the finished installation of the machine with control electronics next to the machine as well as a security cage around the machine.

A) Installation in of the actuator in the test machine frame

B)Installation of the support frame in the lab floor

C) The machine in place with flooring and security cage and the control electronics installed at the left side.

Figure 3.6 Installation of the test machine

3.3 Control and DAQ system

The test machine was designed with both a closed loop and open loop control systems. The closed loop control system was used for positioning the piston rod prior to firing, and was created with a

MTS TestStar II Digital Controller. The closed loop controller provided also emergency stops and safety chain features around the machine. The open loop control system was primarily used for firing the Moog D665 valve for velocities above 1m/s, and to handle a number of other tasks, such as data acquisition. The open loop control system performed the following task simultaneously during a test:

- Control of the Moog D665 valves with an analogue signal between -10 to 10 volt for firing the machine.
- Synchronised triggering of analogue data acquisition equipment (DAQ), and other external equipment such as high speed cameras.
- Keep track of the safety chain status from the TestStar II controller.
- Set the closed loop system in the TestStar II controller on idle, such that the closed loop control did not interfere with operation of the main valves.

A program was written in LabView to handle these tasks, and the system simultaneously handled analogue in- and output, and digital in- and outputs. The hardware part consisted of two National Instrument 6115 multifunctional PCI 12bit DAQ boards with an analogue sampling frequency of maximum 10MHz synchronized on eight channels. The boards were installed directly to the PCI bus in a high performance desktop computer. The DAQ board was programmed to work in two modes: a slow sampling mode with streaming to the PC memory for showing current data during setup of the machine, and a transient mode where the DAQ board's internal memory was set up as a ring buffer, so data was only streamed to the board memory during a test. The latter mode prevented the PCI bus to be flooded with data at maximum sampling frequency. The board memory could hold about 4.3M samples per channel and the memory control was configured to allow an arbitrary distribution of the memory around the trigger. The data before the trigger was pre-trigger data and the data recorded after the trigger was post-trigger data. When the board memory was full after triggering, the data was transferred to the PC memory. Table 3.2 provides the simplified firing sequence of the system.

Table 3.2 Simplified firing sequence. When the user asked to fire, step 5 allowed the used to abort the operation.

Step	Description
1	Prepare TestStar II controller for idle mode.
2	Prepare analogue output sequence based on the selected velocity and load into output buffer of the board.
3	Put analogue output into a firing position and await firing trigger.
4	Stop the slow sampling mode of the DAQ board, reconfigure to transient sampling, and begin ring buffer streaming.
5	Ask user to fire or abort (if the safety chain of the TestStar II controller is still unbroken!)
6	If firing is accepted, put TestStar II on idle.
7	Send trigger to the analogue out, to open the valves and move the piston rod.
8	Wait until analogue sampling has finished and transfer recorded data to the PC memory for saving and post processing of the data. Put TestStar II to active mode.
9	Set DAQ board back to slow sampling mode.

The complete firing sequence included several controls signals sent back and forth to Moog valves and the TestStar II controller to ensure all steps were completed correctly.
A test at a target velocity of 20 m/s would complete in less than 30ms and would leave no possibility for human interaction for triggering of the DAQ board. Instead, the trigger system was designed to be fully automated and to work with external equipment as well. The trigger to fire the machine was activated via a software button such that only the operator could fire the machine. The DAQ equipment and external equipment could be connected to this trigger, or they could work with their own triggers as for example the build in level trigger circuit on the NI 6115 board. A level trigger, triggers when its analogue channels reaches a pre-set level. The external

equipment, as for example a high-speed camera was connected to these triggers and synchronise with the DAQ board. The concept of variable trigger setting and possible trigger dependency is visualised in Figure 3.7.

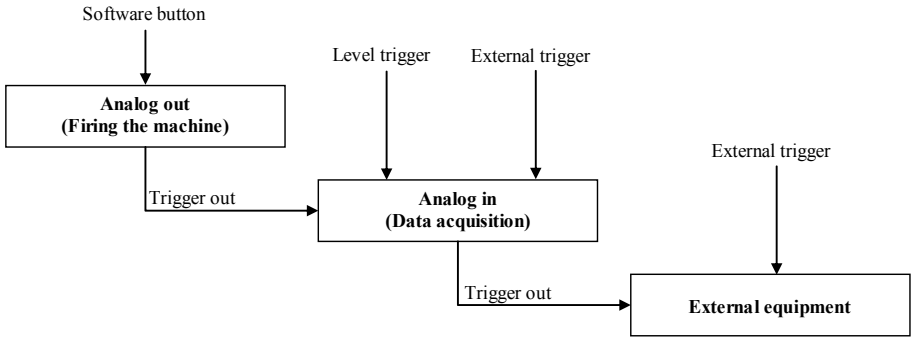

Figure 3.7 Trigger setup

This arrangement provides a flexible setup where data acquisition could be triggered in any possible way and allows for time synchronisation of external equipment.
Before the machine could be fired, the correct voltage signal was generated for the valves. The signal generation was based on a calibration of the machine. The calibration was performed by opening the valves with a given constant voltage signal, and measuring the resulting steady velocity. Figure 3.8A shows the calibration curve with velocity as function of signal voltage. Figure 3.8B shows a sketch of the actual signal sent to the valve.

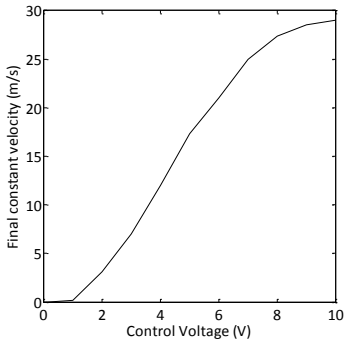

A) Velocity calibration curve

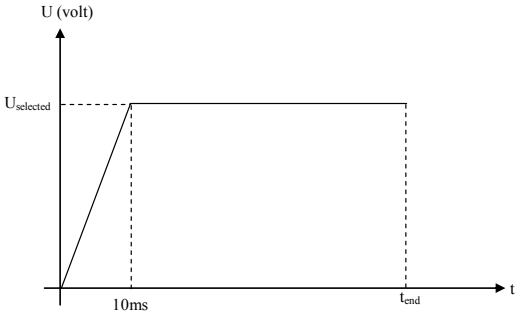

B) Sketch of valve drive signal. Signal was ramped to minimize oscillations in the system.

Figure 3.8 Velocity calibration and used valve signal

The LabView program had three user interfaces. The main user interface allowed the user to select velocity and setup, and to see the status of the DAQ channels and the status of the prerequisites to fire the machine. The window also contained a graph to visualise the acquired analogue data after a test. The DAQ interface allowed the user to setup the analogue channels and to set the ring buffer setting and the trigger routes. The saving window allowed the user to select which data to save.

A Photron APX-RS camera was available for use with the machine and the cameras control was integrated into the program for automatic synchronisation of images and analogue data.

3.4 Control electronics

All the electronics of the machine was assembled in control tower. A custom connector box was designed and built, which connected the NI 6115 board with the MTS controller, the valves, and the sensor amplifiers. The connector box was also equipped with BNC connections for distributing the trigger signals and sensor signals, and further it did also provide a power supply for the Moog valves. The installation of the control tower required custom cabling of all the components. Figure 3.9 shows the control tower, which also includes a PLC control for the pump. All PLC controls were provided by a technician.

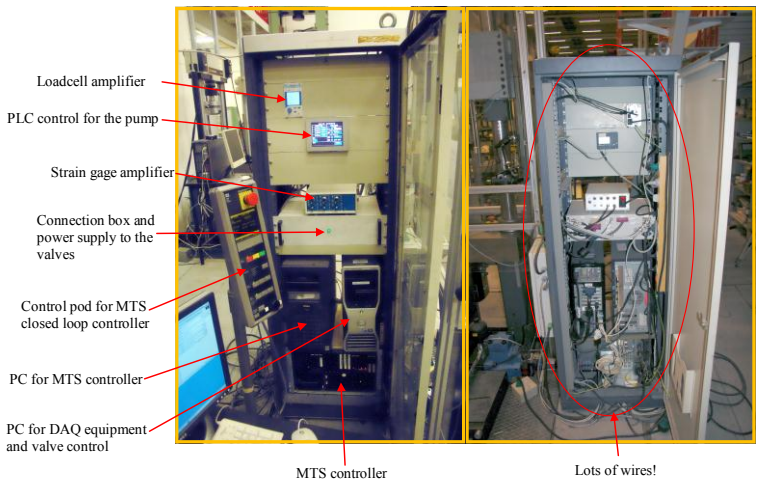

Figure 3.9 Control electronics

3.5 Sensors

The machine was equipped with a Sentech HydraStar displacement transducer (Linear Variable Displacement Transducer, LVDT) mounted in the piston rod for monitoring of the piston rod position. This LVDT was chosen due to its specialised design for high-speed motions.
The machine was also equipped with a Kistler 9071 piezo electric load cell. Piezo electric load cells are designed to measure compressive forces, but here the load cell was implemented into the upper grip structure such that tensile forces could be measured [60]. This was done by preloading the load cell and then let tensile forces reduce the compressive. The amount of preload determines the load capacity of the setup. The preload was limited by the absolute compressive load capacity of the load cell and for this setup, the preload was limited to 150kN by the grip design. The implementation of the load cell in the upper grip system is described in section 3.7.
The machine was equipped with a three-channel FYLDE HT379TA broadband strain gage amplifier. Broadband amplifiers are normally rated with a cut-off frequency and their slew rate referred to input (RTI) or referred to output (RTO). The slew rate is the maximum rate of change the amplifier can sustain, normally given in the units V/µs. For example when the slew rate is 8 V/µs RTO it means the amplifier can maximum change its output with 8 V/µs. The FYLDE HT 379TA had a slew rate of 8V/ µs RTO and the selection guide in Appendix E reveals that a slew rate of 1V/ µs or more is admissible for the high-speed servo hydraulic test machine.

3.6 Specimen design

The test specimen is an integral part of the load train and the design of the specimen influences the load train design and vice versa. In this case, the specimen design was considered first, but the

limitations in the grip design were kept in mind. Only tensile testing was considered in this work. Dogbone specimens are normally used for tensile testing of metallic materials, where the narrow part promotes the failure position. This design is not suitable for FRP materials, as the fibres area required to be cut in the loading direction. Instead, straight sided specimens are used [2], which insures all fibres in the specimen are loaded. However, the straight-sided design complicates the promotion of failure in the gage length and it becomes important to ensure a smooth load transfer between the grip and specimen to avoid premature failure within the grips. Specimens can be made with bonded tabs, loose tabs as emery cloth, or no tabs. Bonded tabs are strongly recommended for highly unidirectional specimens [56]. If segregated wedges are used in wedges grips, the tabs also prevents fibre damage, when the grip tightens around the specimen and 'bite' into specimen. With bonded tabs the load transfer happens through the bond line, and the premature failure could then happen in the tabs (sliding), the bond line (failure) or in the substrate for the bonding.
Straight- sided coupons with bonded tabs were used in this work. The design of the bond line was done in accordance with ASTM 3039 [56] by designing the L_{tab} according to

$$\begin{aligned} &2G_{su}W_{tab}L_{tab} > \sigma_{tu}h_{specimen}W_{specimen} \Leftrightarrow \\ &2G_{su}L_{tab} > \sigma_{tu}h_{specimen} \Leftrightarrow \\ &L_{tab} > \frac{h_{specimen}}{2}\frac{\sigma_{tu}}{G_{su}} \end{aligned} \tag{3.6}$$

σ_{tu} is the ultimate tensile strength of the specimen and G_{su} is the ultimate shear strength of the glue. Equation (3.6) shows the tab length solely depended on the specimen failure strength, the bond line shear strength, and the specimen thickness. The specimen should be thin with long tabs and a strong glue to promote failure in the gage section of the specimen. Figure 3.10A shows and overview of the tab setup for a specimen with tabs on both sides, and Figure 3.10B shows equation (3.6) plotted for different values of the parameters.

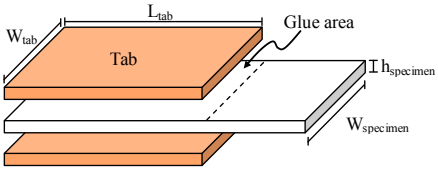

A) Exploded view of tabs around one of the specimen.

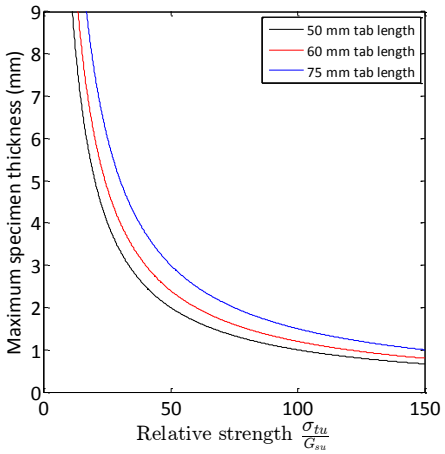

B) Maximum thickness of specimen as function of the tab length and relative strength between specimen and glue.

Figure 3.10 Design of specimen and tabs

A substantial amount of trial and error was required in this work to establish a working specimen design. The trial and error were related to uncertainties in the specimen tensile strength and the bond-line shear strength. The tensile strength increased in many cases with strain rates, and tab designs which worked at quasi-static strain rates, did not work at high strain rate. The bond strength was also indicated to change with strain rate. The solution was to decrease the design bond strength with 50% and design the specimen accordingly.
For quasi axial specimen it was found that the outer layer, which was glued to the tab had to be be

the strongest layer with respect to the loading direction. Off axis, layers were found to fracture in tab area, if they were placed in contact with the tab. An example is given in Figure 3.11A where a 90° and 45° plies were visible on the tabs, which was ripped off during the test. Figure 3.11B shows an example with a UD 0° Eglass/LPET specimen tested at 20m/s where the bond lines failed. The glue was still attached to the aluminium tabs, so failure happened in the glue/specimen interface.

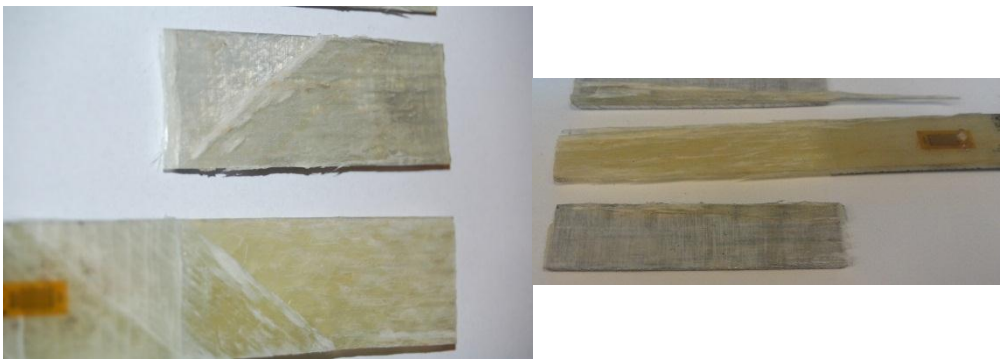

A) Example of a tab failure for a multidirectional specimen with an angled outer layer

B) Example of bond line failure for a UD 0° specimen

Figure 3.11 Examples of tab failures

3.6.1 Gage length

As discussed in chapter 2 the gage length has high influence on the achievable strain rate for a straight-sided test specimen. ASTM 3039 suggests a gage length of 138mm for a 0° layup. However long gage length requires high impact velocities and it was preferable/required to reduce the gage length if a certain strain-rate regime had to be accessed. The drawback of the smaller gage lengths is a higher vulnerability to misalignment and a less representative nature of the bulk material.

3.7 Load train

The load train includes the load cell, the grips to fixate the specimen and the slack adapter. The conventional slack adapter design from chapter 2 was selected. Standard grips, both hydraulic and mechanical, were found to be too heavy to

be used in as their weight easily exceed 15-20kg for 100kN design. Instead, a set of highly optimized and customized mechanical wedge grips were designed. High-strength tough aluminium was used for the housing of the grips, and the wedges were made from hardened steel. The maximum specimen length inside the grip was set to 60mm as a compromise between weight and maximum tab length on the specimens. The grip consisted of two parts: a static, and a movable. The movable part was designed with a wedge shaped cavity to house the wedges. The two parts was fastened to each other with bolts. When the bolts were tighted manually, the wedge was forced together and the specimen was clamped. The maximum specimen thickness was 9.7mm including tabs. Figure 3.12A shows the upper grip mounted in the test machine and Figure 3.12B shows a static finite element simulation of the grip with the specimen pulled at 150kN. The used aluminium had a yield strength of 620MPa.

A) Upper grip assembly mounted on the machine

B) Von Mises stress in a static Finite element simulation of the upper grip assembly with 150kN of load applied to the specimen. Specimen had full contact to the wedges.

Figure 3.12 The upper grip system and the finite element simulation of the system

The upper grip assembly also accommodated the piezo electric load cell, where the load cell was mounted between the upper grip and the crosshead of the machine frame. The crosshead had a through hole in the centre and a tie rod was mounted through the hole to pull the upper grip up against the crosshead as shown in Figure 3.13. The tie rod was then used to preload the load cell. Calibration of the load cell was carried out as the tie rod shunted the load cell.

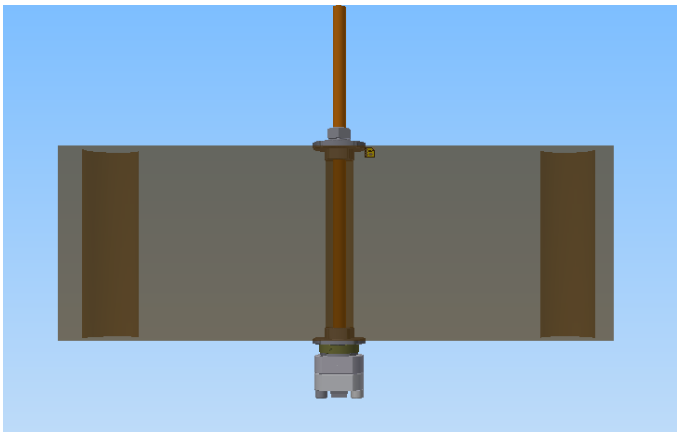

Figure 3.13 Upper grip assembly and the mounting to the crosshead

The lower grip was designed similar to the upper grip assembly and made use of the same components. The weight of a full grip assembly was about 1.5kg. The lower grip was connected to the piston rod with the slack adapter. The slack adapter was designed as a long slender bar, which was screwed up into the lower grip. The piston rod of the cylinder was made hollow to save weight and the space was used to install the slack adapter down into the piston rod. The plug was designed with a hole where the slack adapter could pass through.

Figure 3.14 shows the parts used for the load train including wedges and equipment for aligning the load train. Attachment equipment for the reference load cell for calibration is also shown. The slack adapter assembly is shown in the left with the lower grip attached.

The wedges were made from hardened steel to accommodate hard materials to be gripped. The surface was segregated to allow a mechanical interlock to be created to the tabs of the test

specimens. Two different patterns were used, with the coarse one for soft tabs where deep mechanical interlock was needed to create a strong connection.

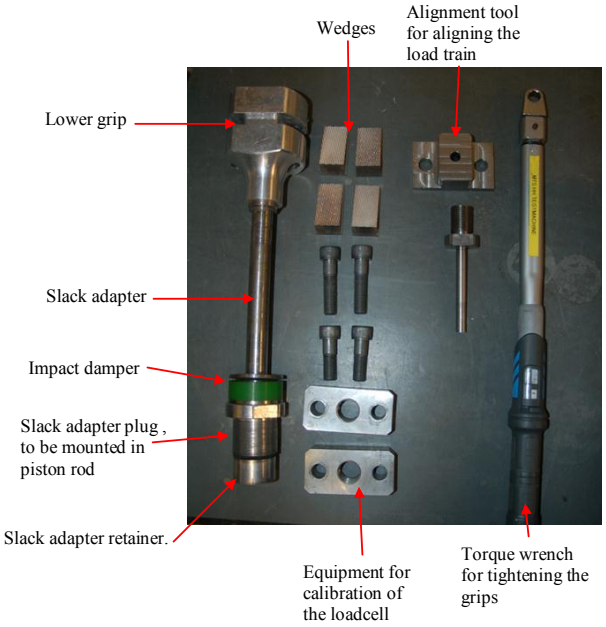

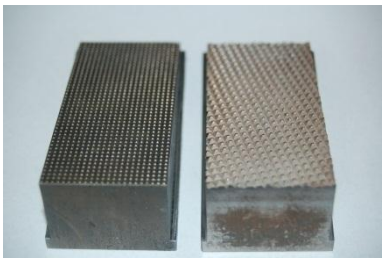

A) Parts for the load train *B) Wedges – with different patterns*

Figure 3.14 Parts for the load train. The upper grip assembly is not shown.

3.8 Issue with grips

It was found that the highest forces in the load train occurred when the lower grip impacted the piston rod upon deacceleration of the piston rod. Due to the requirement of a stiff slack adapter there was no room for a large deacceleration length, and the impact was normally damped with a rubber layer. Figure 3.15A shows a failed rubber damper, which caused the grip in Figure 3.15C to fail under its own weigh during impact. The rubber damper was changed to a thick PUR damper, which was custom casted from a Shore 72D polyurethane base. The lower grip was further modified to remove stress concentration critical to the deacceleration loading. The modifications solved the problem.

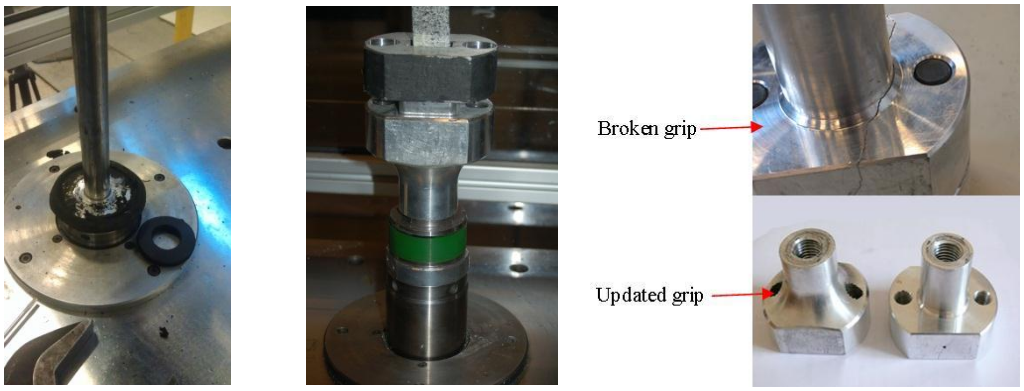

A) Failed impact damper. Lose undamaged damper shown next to the piston rod.

B) Updated impact damper (Green) casted from PUR shore 72D.

C) Broken and updated grip

Figure 3.15 Impact damper for deaccleration of the lower grip.

3.9 Summary

A high-speed servo hydraulic test machine was designed, constructed and equipped with a full set of sensors to monitor test specimens during testing. The work also included constructing the full control system as well as a support frame to integrate the machine into the lab.

The work included design of a conventional slack adapter and custom grips and equipment to mount the piezo electric load cell. The load cell and grips were designed to maximum tensile loads of 100kN. The slack adapter system was aimed at testing fibre-reinforced composites with respect to the choice of a conventional slack adapter and rough segregated wedges for gripping soft materials. The velocity calibration in Figure 3.8A showed the machine was able to reach velocities in excess of 28m/s.

4 Characterisation of fibre reinforced materials at medium strain rates

This chapter present an examination of the medium strain rate behaviour of three fibre-reinforced polymers (FRP). An Eglass/Epoxy, an Eglass/Lpet and Carbon/PA6 FRP was tensile tested from 1 /s to 300/s with the high-speed servo-hydraulic test machine described in chapter 3. The findings was used as validation cases for the model presented in chapter 2 and as input data for the RESIST project mentioned in the preface.

4.1 Method

The three materials were tensile tested at three loading velocities 1, 7.5 and 20 m/s, in two loading direction and with two layups. The two lay-up were a UD and a Quattro axial lay-up (named MD). The two loading direction for the UD configuration were 0°, along the fibres, and 90°, transverse to the fibres. The MD lay-up had no dominant fibre direction and the test direction was just named "Tensile". Table 4.1 details the test combinations matrix. Each test series is identified with a code as "CRBJ20B" and covers a combination of velocity, loading direction, and lay-up. Five specimens were tested for each test series and the test matrix Table 4.1 covers in total 125 tests. Specimen size was given as total size and the gage length L_S. The general specimen design is shown in Figure 4.1 and the details of the specimen materials, fabrication methods and tab size is given in Table 4.2. Figure 4.2 shows specimens before testing.

Table 4.1 Test matrix. IP = In plane.

Material	No	Description	Deformation rate (m/s)	Specimen (mm)	Lay-up	Loading	Results
Eglass/Epoxy	CRBJ20B CRBJ20C CRBJ20D	IP Tension 0°	1 7.5 20	Straight 150x15x1 L_S = 50	$[0]_4$	Tension along 1 axis	E_{11}^t, ν_{12}^t, X_{11}^t
Eglass/Epoxy	CRBJ21B CRBJ21C CRBJ21D	IP Tension 90°	1 7.5 20	Straight 150x25x4 L_S = 50	$[0]_4$	Tension along 2 axis	E_{22}^t ν_{21}^t, X_{22}^t
Eglass/Epoxy	CRBJ21E	IP Tension 90°	1	Straight 150x25x4 L_S = 100	$[0]_4$	Tension along 2 axis	E_{22}^t ν_{21}^t, X_{22}^t
Eglass/Epoxy	CRBJ10B CRBJ10C CRBJ10D	IP Tension	1 7.5 20	Straight 150x25x4 L_S = 50	$[0/-45/90/45/-45/90/45/0]_3$	Tension along x- axis	E_{xx}^t ν_{xy}^t, X_{xx}^t
Eglass/Lpet	CRBB20B CRBB20C CRBB20D	IP Tension 0°	1 7.5 20	Straight 150x15x1 L_S = 50	$[0]_4$	Tension along 1 axis	E_{11}^t, ν_{12}^t, X_{11}^t
Eglass/Lpet	CRBB21B CRBB21C CRBB21D	IP Tension 90°	1 7.5 20	Straight 150x25x4 L_S = 50	$[0]_8$	Tension along 2 axis	E_{22}^t ν_{21}^t, X_{22}^t
Eglass/Lpet	CRBB10B CRBB10C CRBB10D	IP Tension	1 7.5 20	Straight 150x25x4 L_S = 50	$[0/45/90/-45]_s$	Tension along x- axis	E_{xx}^t ν_{xy}^t, X_{xx}^t
C/PA6	CRBF20A CRBF20B CRBF20C	IP Tension 0°	1 7.5 20	Straight 150x15x1 L_S = 50	Winding	Tension along 1 axis	E_{11}^t, ν_{12}^t, X_{11}^t
C/PA6	CRBF21A	IP	1	Straight	Winding	Tension along	E_{22}^t

CRBF21B CRBF21C	Tension 90°	7.5 20	150x25x4 L_S = 50	2 axis	v_{21}^t, X_{22}^t

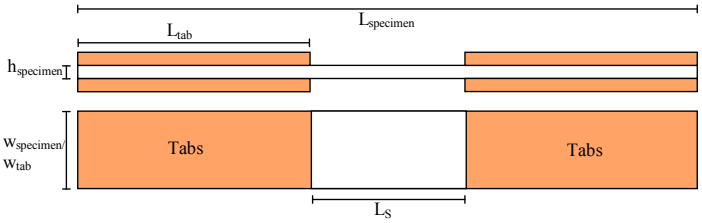

Figure 4.1 General specimen design

A) UD layup, 0° loading direction. *B) UD layup, 90° loading direction.* *C) Quattro axial layup – Loading direction: x.*

Figure 4.2 Specimens before test for an impact velocity of 20 m/s

Table 4.2 Test coupons and materials

Table header	Eglass/Epoxy	Eglass/Lpet	Carbon/PA6
Matrix	ARALDITE LY 564/ ARADUR 917	LPET	PA6
Fibre	SAERTEX S14EU990-00940-T1300-499000	TufRov 1200 Tex 4588	Tenax 12k X011 HTS 40
Production method	Vacuum infusion. Specimen cut watercooled diamond saw	Commingled yarn - Vacuum consolidation Specimen cut water cooled diamond saw	Commingled yarn - Winding. Specimen cut watercooled diamond saw
UD 0°			
Tabs (L_{tab} xW_{tab})	60x15mm [0/90] Eglass/Epoxy	60x15mm [0/90] Eglass/Epoxy	60x15mm [0/90] Eglass/Epoxy
UD 90°			
Tabs (L_{tab} xW_{tab})	40x25mm [0/90] Eglass/Epoxy	40x25mm [0/90] Eglass/Epoxy	40x25mm [0/90] Eglass/Epoxy
Quattro axial			
Tabs (L_{tab} xW_{tab})	60x25mm [0/90] Eglass/Epoxy	60x25mm [0/90] Eglass/Epoxy	

All specimens were equipped with tabs glued with Scotch DP460 Epoxy glue and all tabs were made from standard Eglass/epoxy $[0/90]_x$ tab material. Tab length was maximized with respect to the specimen description in chapter 2. Department of Wind Energy (DTU) tested the materials under static condition and all result mentioned as “static” results in this chapter comes from

Toftegaard et al. [62, 63].
Load was measured with the Kistler 9071 Piezo electric load cell and the load was converted to stress by dividing the load with the initial cross sectional area of the test specimen. A strain gage was glued to the gage area with cyanoacrylate for measuring strain. Two test specimens in each test series were equipped with a 0°/90° 350Ω strain gage with 6mm gage length (Vishay EA-06-125VA-350) for measuring Poisson's ratio. The remaining specimens were equipped with a Vishay EA-06-250BF-350 350Ω strain gage, also with 6mm gage length. In addition, a high-speed video was captured of the test specimen with a single Photron APX-RS high-speed camera. All test specimens were spray painted with a speckle pattern to employ the images for 2D Digital Image Correlation (DIC) with the DIC code ARAMIS 2D. Prior to testing, the camera were calibrated for scale, and lens distortions. The set-up details are given in Table 4.3 and examples of speckle patterns are shown in Figure 4.3 Examples of speckle patterns. ARAMIS creates a displacement field for the specimen, which is converted into a strain field. The strain field consisted of a strain tensor estimated with a least square method in each facet from the eight surrounding facets. The strain measure for the characterisation of the test coupon was taken as the average strain of all calculated facets over the gage area.

Table 4.3 Digital image correlation setup

Technique used	2D Image correlation, Calibrated
Subset size	15 x 15px – 19 x 19px
Facet step	13 px
Field of view	144 x 640px - 96 x 256px
Frame rates	10000 – 70000 FPS
Shutter time	2-10µs
Camera	PHOTRON APX-RS
Lens	50mm
Light	Dedocool

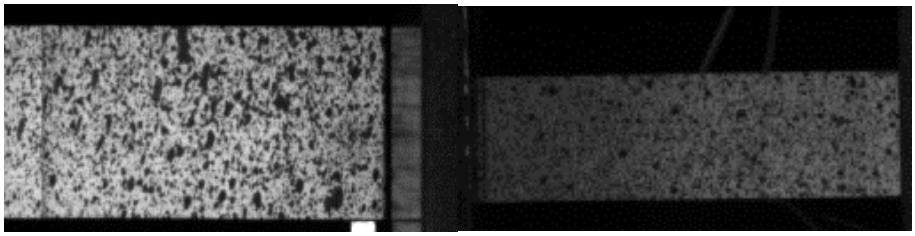

Figure 4.3 Examples of speckle patterns.

4.2 Results

The measured stress-strain data were used to construct the stress-
strain curve. Further, the elastic modulus, the failure stress, the failure strain, and strain rate were calculated as given in Table 4.4. For each parameter in each test series, the 95% confidence interval was calculated assuming a normal distributing with n-1 degrees-of-freedom where n was the number of test specimens in the test series. The 95% confidence interval is written in parenthesis after the mean value.

Table 4.4 Parameter estimation

Parameter	Method	Data source
Elastic moduli	Least square regression in the 0.2% - 0.5% strain interval. The interval may vary slightly dependent on data quality	Strain gage and DIC. Average strain calculated before regression.
Failure stress	Maximum load divided by cross sectional area	Kistler load cell
Failure strain	Strain at maximum load. If there is no strain data, strain data is extrapolated.	Strain gage/DIC
Strain rate	Calculated as the time derivate of strain measurement. The reported strain rate is calculated as the average strain rate over the last 50% of strain in the specimen before failure.	Strain/DIC
Poisson's ratio	Least square regression over linear part of inplane strains – strain interval maximized to minimize noise.	DIC – average x and y strain of the estimated strain tensors / Strain gage where available.

Figure 4.4 shows examples of specimens after test for all test velocities.

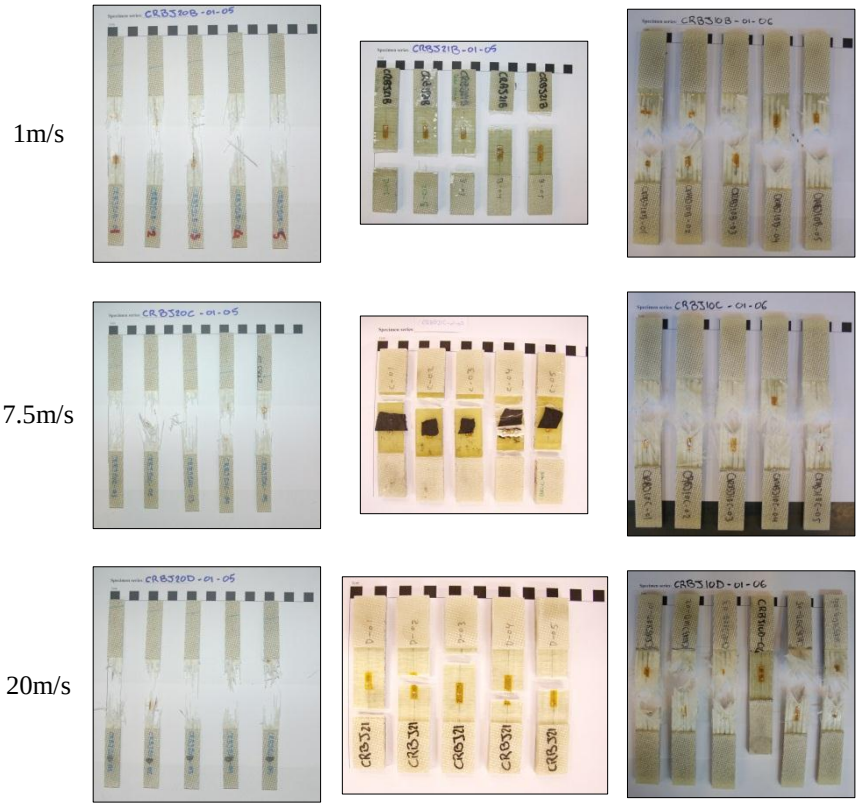

A) UD layup. Loading direction: 0°. *B) UD layup. Loading direction: 90°.* *C) MD layup. Loading direction: x.*

Figure 4.4 Specimens after test for an impact velocity of 20 m/s

There was sign of higher splitting of the specimen for the UD 0° specimen at higher velocities. The 90° did not have any significant changes in its fracture pattern and the same was the case for the MD specimens. Figure 4.5 gives examples of stress strain curves for UD 0° at all impact velocities.

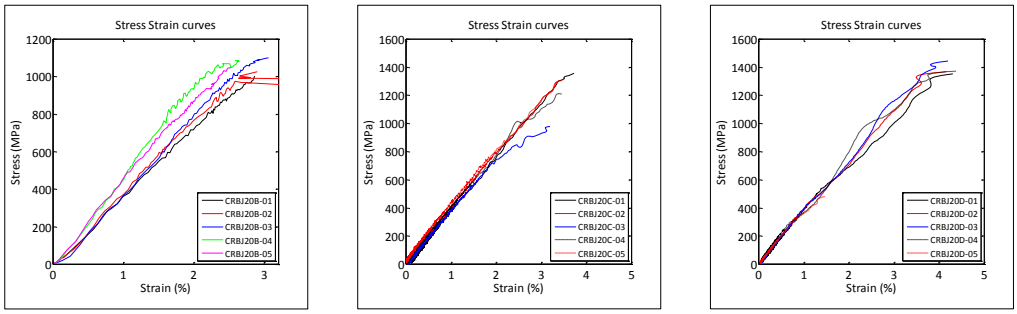

A) Impact velocity: 1 m/s *B) Impact velocity: 7.5 m/s* *C) Impact velocity: 20 m/s*

Figure 4.5 Example of stress strain curves for Eglass/Epoxy 0° loading direction

All estimated parameters are given in Table 4.6 to Table 4.9. All results in the columns "static" are taken from [62, 63].

Table 4.5 Elastic modulus (GPa)

	Static	**1m/s**	**7.5 m/s**	**20 m/s**
Eglass/Epoxy 0°	45.3 (1.3)	42 (3.42)	42.5 (2.0)	41.2 (2.1)
Eglass/Epoxy 90°	12.7 (0.8)	13.5 (3.4)	13.6 (1.88)	12.2 (2.2)
Eglass/Epoxy MD	22.1 (0.6)	19.6 (0.9)	20.1 (1.9)	18.2 (2.8)
Eglass/Lpet 0°	39 (0.3)	36.2 (3.3)	37.3 (1.8)	34.3 (4.1)
Eglass/Lpet 90°	9.5 (0.2)	9.2 (2.4)	10.5 (2.4)	8.6 (2.3)
Eglass/Lpet MD	19.7 (0.3)	15.0 (1.1)		
Carbon/PA6 0°	100	110 (10.8)	103 (7.3)	97.6 (7.7)
Carbon/PA6 90°	8.9	6.2 (0.4)	5.7 (2.0)	6.75

Table 4.6 Failure stress (MPa)

	Static	**1m/s**	**7.5 m/s**	**20 m/s**
Eglass/Epoxy 0°	1041 (31)	1095 (42)	1274 (186)	1485 (84)
Eglass/Epoxy 90°	29 (3)	26.3 (11.3)	34.3 (2.01)	32 (5.1)
Eglass/Epoxy MD	387 (8)	481 (23)	554 (11)	616 (31)
Eglass/Lpet 0°	789 (21)	903 (84)	882 (69)	788 (82)
Eglass/Lpet 90°	33 (2)	27.1 (18.4)	33.3 (37.8)	30.4 (6.0)
Eglass/Lpet MD	337 (9)	315 (29)		
Carbon/PA6 0°	931	1569 (107)	1869 (205)	1816 (184)
Carbon/PA6 90°	70	46.6 (12.3)	39.4 (19.4)	48.25

Table 4.7 Failure strain (%)

	Static	**1m/s**	**7.5 m/s**	**20 m/s**
Eglass/Epoxy 0°	2.9 (0.8)	2.77 (0.38)	3.85 (0.16)	4.41 (0.25)
Eglass/Epoxy 90°	0.22 (0.03)	0.19 (0.09)	0.28 (0.05)	0.54 (0.07)
Eglass/Epoxy MD	2.7 (0.2)	3.56 (0.19)	3.91 (0.09)	4.15 (0.68)
Eglass/Lpet 0°	2.2 (0.1)	2.65 (0.15)	3.12 (0.69)	3.57 (0.87)
Eglass/Lpet 90°	0.39 80.03)	0.38 (0.14)	0.32(0.4)	0.28 (0.13)
Eglass/Lpet MD	2.65 (0.184)	3.58 (1.00)		
Carbon/PA6 0°	1.0	1.31 (0.10)	1.59 (0.21)	1.87 (0.17)
Carbon/PA6 90°	0.85	0.63 (0.2)	0.38 (0.07)	0.63

Table 4.8 Poisson's ratio (-)

Table header	Static	1m/s	7.5 m/s	20 m/s
Eglass/Epoxy 0°	0.27 (0.013)	0.26 (0.05)	0.30 (0.04)	0.30 (0.01)
Eglass/Epoxy 90°	0.077 (0.008)	0.08	0.05	0.06
Eglass/Epoxy MD	0.301 (0.003)	0.27 (0.01)	0.27 (0.03)	0.31 (0.07)
Eglass/Lpet 0°	0.332 (0.013)	0.33 (0.04)	0.29 (0.02)	0.28 (0.07)
Eglass/Lpet 90°	0.083 (0.004)			
Eglass/Lpet MD	0.336 (0.011)	0.30 (0.05)		
Carbon/PA6 0°	0.32	0.36 (0.04)	0.36 (0.11)	0.31(0.08)
Carbon/PA6 90°	0.036	0.018	0.023	

Table 4.9 Average strain rate (/s)

Table header	Static	1m/s	7.5 m/s	20 m/s
Eglass/Epoxy 0°		2.6 (1)	78 (39)	298 (38)
Eglass/Epoxy 90°		3.6 (2.3)	3 (1.24)	4.8 (3.8)
Eglass/Epoxy MD		2.4 (1.1)	94 (13)	211 (75)
Eglass/Lpet 0°		2.8 (0.6)	121 (20)	258 (126)
Eglass/Lpet 90°		7.3 (1.4)	2.3 (1.4)	2 (1.8)
Eglass/Lpet MD		3.4 (0.7)		
Carbon/PA6 0°		3 (0)	90 (20)	135 (24)
Carbon/PA6 90°		6 (4.9)	2.8 (2.4)	6.5

The data in Table 4.9 show that the strain rate for the 90° specimens was low even at high impact velocities, since the specimens were broken before the slack adapter completely engaged the specimen. The effect could be seen for the 0° and MD specimens where the strain – strain rate curves in Figure 4.6 shows an initial ramp with low strain rates up to a strain level between one and two percent, before the strain rate increased. The 90° fracture strains are below 1% so they failed in this preload range. The strain rate curves also showed that it was not possible to achieve a constant strain rate.

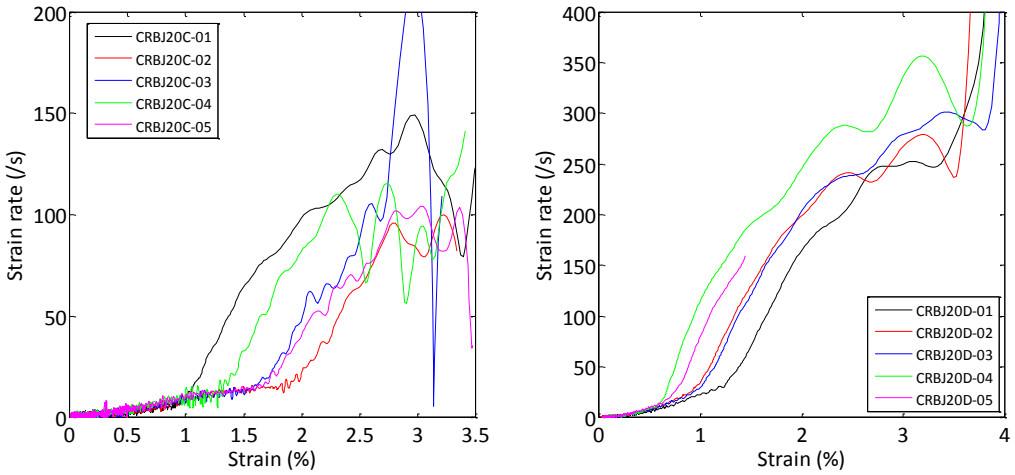

A) 7.5m/s Impact velocity *B) 20 m/s Impact velocity*

Figure 4.6 Example of strain - strain rate curves. The non-constant strain rate was found for all tests!

Figure 4.7 show the graphs of data in Table 4.6 to Table 4.8. For each test series, the average parameter values were normalised with the mean value of the static test and plotted against the

average strain rate for the test series.

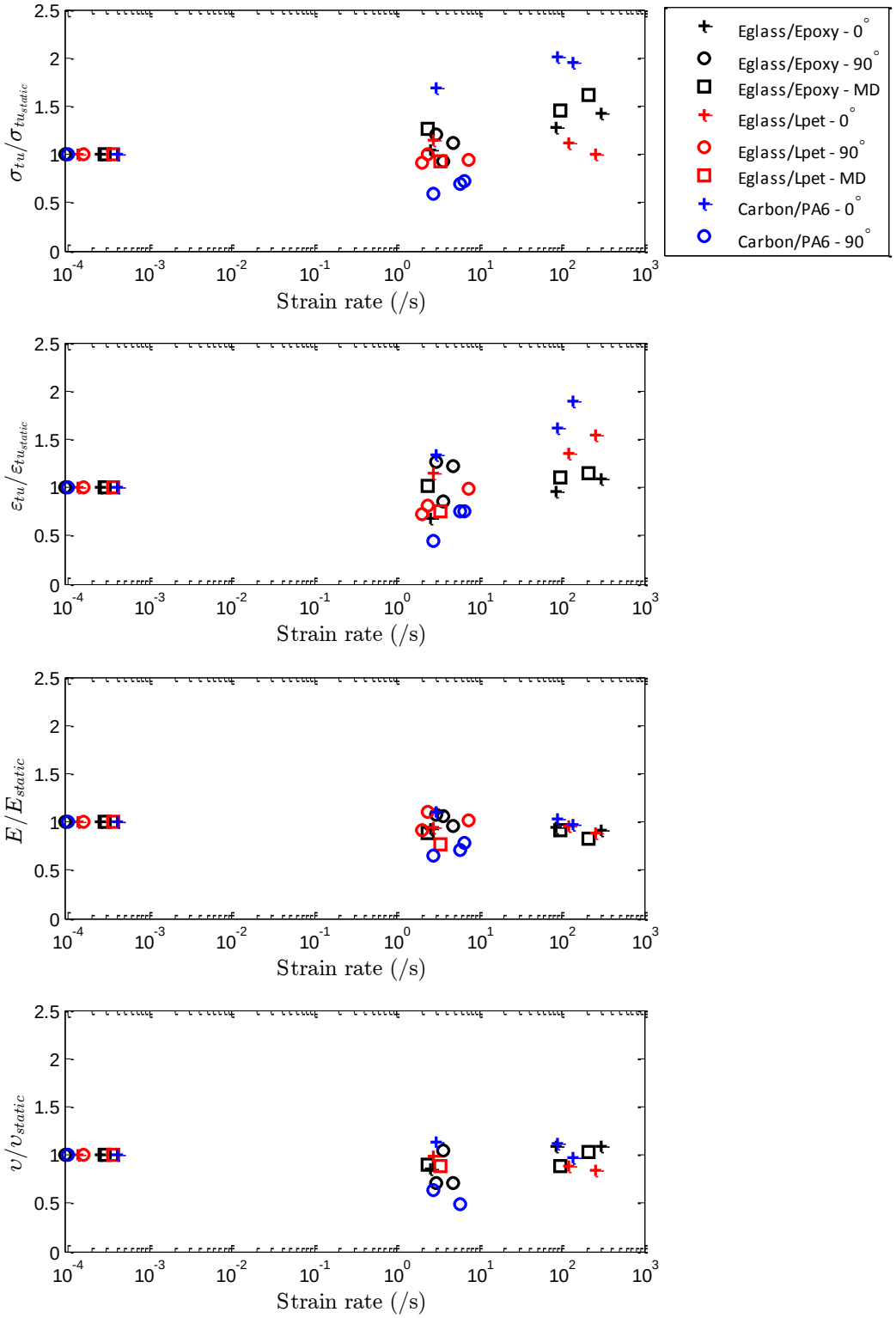

Figure 4.7 Averaged normalised Failure stress, Failure strain, Elastic modulus and poisons ratio as function of strain rate

Figure 4.6 present examples of strain - strain rate curves and Figure 4.8 present an example of the curve from where poisons ratio is estimated.

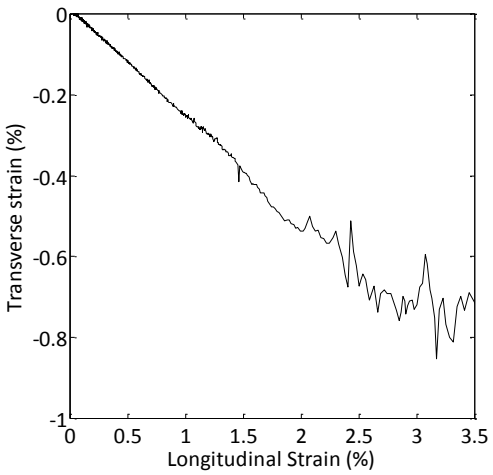

Figure 4.8 Example of curve from which poisons ratio is estimated as the slope of the curve. This curve is for UD 0° Eglass/Epoxy at 20m/s.

4.3 Discussion

Figure 4.7 indicates that the failure stress and strain are more affected of strain rate than the elastic parameters (the elastic modulus and Poisson's ratio). Both the failure stress and strain increase with strain rate while the elastic parameters are unaffected. Both the Eglass/Epoxy UD 0° and MD laminates showed a positive trend with strain rate whereas the UD 0° Eglass/Lpet first increased and then dropped at the highest strain rates. The 90° specimens could not be tested at higher strain rate due to limitations in the load train. The Carbon/PA6 dropped in fracture stress and strain at higher strain rates whereas the Eglass/Epoxy and Eglass/Lpet stayed at the same level. It should be noted that the 0° Carbon/PA6 shows a high degree of rate dependency from static to 1/s. The static measurements were done in a former project [64] while the new specimen was produced for this project. After the test were carried out, it was noted that the specimens for static testing was produced with a Tenax STS (Standard tensile strength) [65] carbon fibre while the new specimens was manufactured with a Tenax HTS (High tensile strength) carbon fibre [64]. The HTS fibre has a typical strength of 4300MPa while the STS fibre has a typical strength of 4000 MPa. The low static value of around 1GPa in failure strength cannot be explained solely from the use of a different fibre. The static measurement puts the Carbon/PA6 in level with the Eglass/Epoxy material. The apparent high strain rate effect indicated here is doubtful because of the low static measurement. Only small increase in fracture strength is reported in literature for carbon materials [24, 26].

The elastic modulus was not significantly affected by strain rate, but the estimates at higher strain rates had high scatter. The ASTM D3039 standard [56] prescribed a strain interval from 0.1 to 0.3% strain for estimation of the elastic modulus, but the first amount of strain could be disturbed by resonance in the load cell as described in section 1.5. Further, the strain – strain rate plots showed a low strain rate in this strain range. If the strain rate and elastic modulus were estimated at higher strain rate, any nonlinearity in the material behaviour would affect the calculated elastic modulus. For these reasons it is not possible to say if the elastic modulus is unaffected by the strain rate. Poisson's ratio was estimated in the same range as the elastic modulus and the same arguments apply as for the elastic modulus. However, Figure 4.8 shows that Poisson's ratio (slope

of the curve) is constant up to around 2% longitudinal strain where the strain rate has started to raise. The noise and linearity after 2% longitudinal strain is believed to be damage progression in the specimen.

The general trends in the data presented here correspond to what has been presented in literature. However, constant strain rate could not be obtained, and the average strain rate then depend on the selected strain interval to calculate the average strain rate. Figure 4.9A illustrates the problem where the strain rate could be set between 100/s and 250/s. Recently, Fitoussi et al. [57] reported high strain rate testing of FRP composites with a similar setup as used in this work. The time – strain plot in Figure 4.9B from Fitoussi et al. [57] shows the same problem with a non-constant strain rate, and the secant line was an attempt to estimate the strain rate. It indicate the problem of non-constant strain rate persist in the data reported in literature and that the reported strain rate may be highly dependent on the experimenters choice of interval for calculation of the strain rate.

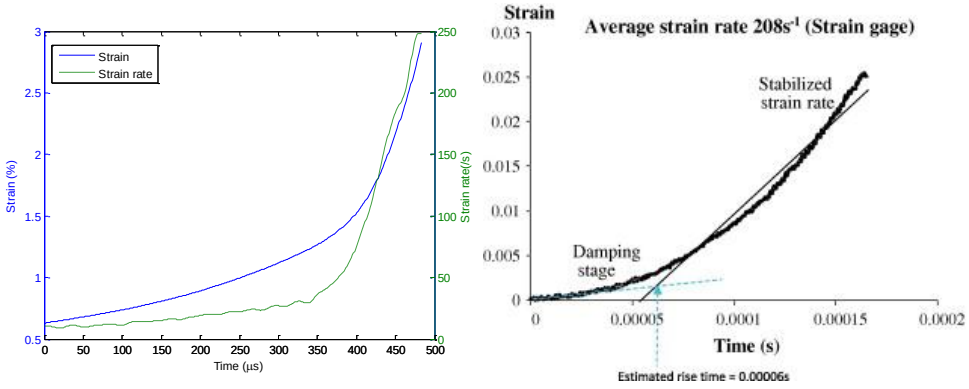

A) Strain vs time and strain rate vs. time for a Eglass/Epoxy 0° specimen tested at 20m/s. *B) Time vs. strain plot from* [57]

Figure 4.9 Comparison of non-constant strain rate problem with results from Fitoussi et al. [57].

If the simulation application is sensitive to strain rate effects, then the calculation of the strain rate in the test becomes important factor as this affect the rate sensitive parameters values in the material models. Further, Figure 4.9A also shows that the elastic modulus and failure stress is estimated at different strain rates for the same test. Any interpretation of rate sensitivity in the elastic modulus should be done with great care from this kind of high strain rate testing, as the modulus is estimated when the specimen is strained at low strain rates.

4.4 Summary

An Eglass/Epoxy, An Eglass/Lpet, and C/PA6 were tested at elevated strain rates. General trends in data corresponded to results reported in literature. However, the C/PA6 showed very high rate sensitivity, which is doubtful. It was not possible to test 90° specimen at higher strain rate since preloading in the slack adapter during acceleration caused the specimen to fail before a high strain rate was reached. It was not possible to reach a constant strain rate in any of the test. In chapter 2 this was explained as an problem with inertial damping. It was pointed out that the variable strain rate caused problem in stating the strain rate for the test, and the elastic modulus would be estimated in a strain regime with low strain rate.

5 Introduction to the Split Hopkinson Pressure Bar

The Split Hopkinson Pressure Bar is based on techniques developed by Bertram Hopkinson in 1914 to study wave propagation in long elastic bars [66]. The technique was later used by Davis and Hunter [67] and Kolsky et al. [68] to create the Split Hopkinson Pressure Bar (SHPB). The SHPB relies on a single elastic wave to load the specimen, and avoids the oscillations in load measurements from the high-speed servo hydraulic test machine. The original SHPB was designed for compression testing, but was later extended to tension, torsion, multi axial, and 3 point bending tests. The SHPB method is widely described in the literature [17, 18, 20, 69-72] and Zhang et al. [73] recently gave a comprehensive review of the SHPB method for linear elastic materials. This chapter briefly introduces the SHPB method with respect to compression testing of linear elastic brittle materials.

5.1 The Split Hopkinson Pressure Bar

The SHPB consists of two elastic bars with the test specimen positioned between them [8]. One bar is called the "Incident bar" and the other bar is called the "Transmitter bar". A schematic is shown in Figure 5.1 and an photo of the SHPB at the University of Southampton is shown in Figure 5.2.

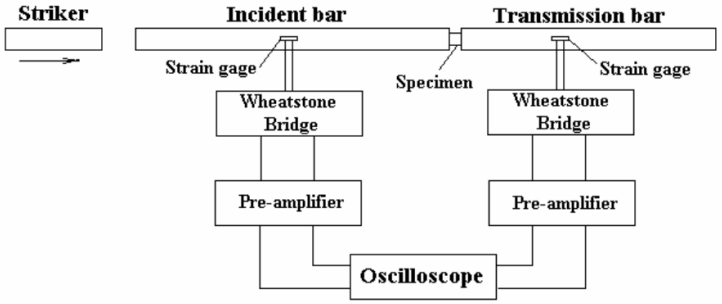

Figure 5.1 Schematic overview of the compressive Split Hopkinson Pressure Bar[69]

A test is conducted by firing a striker bar against the Incident bar. The impact between the bars creates a compressive pulse, named the "Incident wave", which travels towards the specimen. The Incident wave reflects and transmits when it reaches the specimen and the reflected part is named the "Reflected wave". The wavelength of the Incident pulse is twice the length of the Striker bar [3] and much longer than the specimen, such that the Incident wave alone fails the specimen in compression.

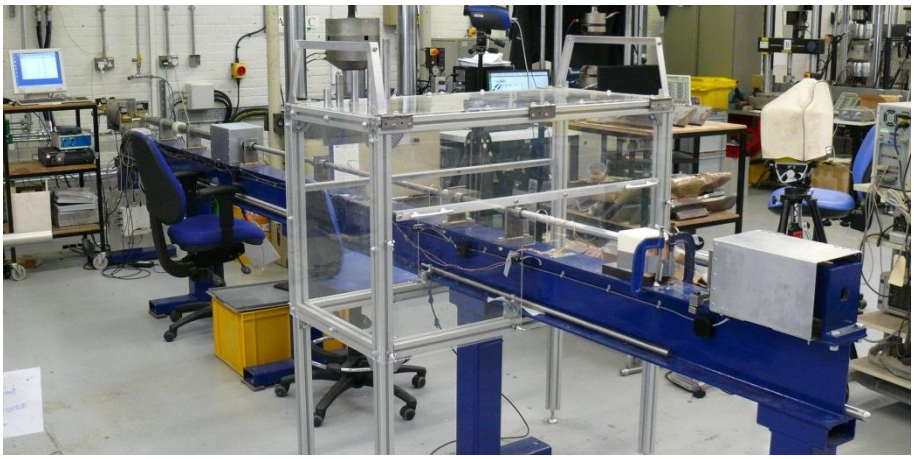

Figure 5.2 Example of a Split Hopkinson Pressure Bar at the University of Southampton

The transmitted wave propagates through the specimen towards the Transmitter bar and reflects and transmits again at the specimen/Transmitter bar interface. The transmitted part sets the Transmitter bar in motion at the interface and the resulting wave travelling in the Transmitter bar is called the "Transmitted wave". The reflected part propagates back through the specimen towards the Incident bar. At the specimen/Incident bar interface, the wave in the specimen reflects and transmits again and the wave is trapped in the specimen overlapping itself, while the reflections gradually loses more and more amplitude. At a certain time the wave has overlapped itself so many times that a state of constant deformation and stress equilibrium is reached and ideally the specimen first fracture after this state is reached.

The Incident bar, the Transmitter bar, and the Striker bar, are normally made from the same material and with the same cross sectional area. The striker bar is normally propelled against the Incident bar with a gas gun driven by either compressed air or a compressed inert gas.

Strain gages are placed on the bars to measure the waves and the strain gages are connected to high-speed strain gage amplifiers, which condition and amplify the signal from the strain gages to a high-speed Data acquisition card.

The Incident, the Reflected, and Transmitted wave are measured and the signals are conditioned and amplified with high-speed strain gage amplifiers and collected with a high-speed data acquisition board.

Figure 5.3A shows the waves generated in an SHPB with direct impact between the Striker bar and the Incident bar. According to classic wave mechanics, the direct impact between the Striker bar and the Incident bar creates a square wave as seen in Figure 5.3A with ripples due to dispersion [3]. The form of the reflected and transmitted wave is altered by the specimen response.

Figure 5.3B shows an example of pulse shaping where a copper disc is placed between the striker bar and the Incident bar. The copper disc deforms plastically and creates a ramp Incident wave, which is beneficial for testing linear elastic materials and soft materials [69, 74]. On the Incident bar, the Incident and Reflected wave are recorded with the same strain gage. The distance between the strain gage and the specimen must be at least twice the length of the Striker bar to avoid overlap of the waves, since the wavelength of the Incident wave is twice the striker bar length in the case of direct impact [3]. If pulse shaping is applied, the pulse duration is extended to more than twice the striker bar length and the gage position should be adjusted accordingly [75].

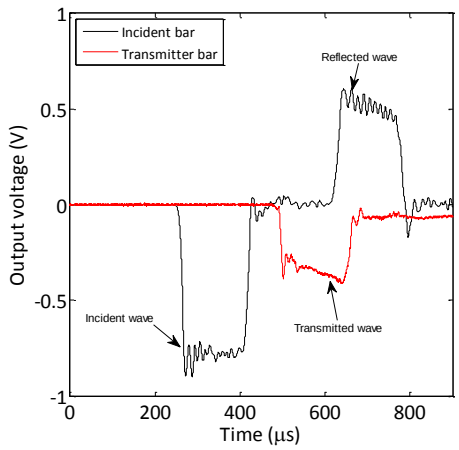

A) Waves from a standard SHPB with direct impact between the striker bar and the Incident bar

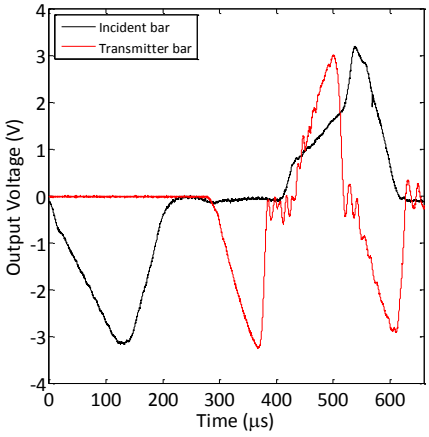

B) Waves from a SHPB with pulse shaping. In this case a copper disc was placed between the striker bar and the Incident bar

Figure 5.3 Examples of stress waves generated in the SHPB

The amplitude of the Incident wave is the particle velocity the wave carries as given by

$$\sigma = \rho C U_p \Leftrightarrow \varepsilon = \frac{U_p}{C} \tag{5.1}$$

σ is stress amplitude, ρ the density of the bar, U_p the particle velocity and ε is the strain in the bar. The total displacement of a material point due to a pass of the wave is obtained by integration of the wave over its total duration. A low deformation rate requires an Incident wave with low amplitude and long duration t_I to load the specimen to failure. The wavelength is calculated from the duration and the wave velocity C_I in the Incident bar as

$$L_{wI} = t_I C_I \tag{5.2}$$

Most metallic materials have a wave velocity of around 5000m/s and long wave duration easily requires a very long Striker bar and Incident bar. The gas gun will also have to size with the Striker bar and in the end there is a practical limit to how low strain rates can be achieved in the SHPB.

The stress strain curve of the material is obtained by a wave mechanics analysis of the recorded waves, and the classical Kolsky analysis [68] requires a set of assumptions [68, 71]:

- 1D Dispersion free wave motion in the bars
- The bars remain elastic at all times,
- The bar/specimen interfaces remains flat and parallel throughout the entire experiment.
- The bars have the same elastic wave speed and diameter.
- The specimen is in stress equilibrium.
- Strain gages are placed at the Incident and Transmitter bar at the same distances from the specimen.
- Specimen has lower mechanical impedance than the bars.

Figure 5.4 shows the specimen positioned between the Incident and Transmitter bar with the respective interfaces defined as (a) and (b). A, E and ρ is the cross sectional area, elastic modulus ρ

density respectively. Subscript I, S and T indicates the Incident bar, specimen and Transmitter bar respectively. The positive direction is marked (x).

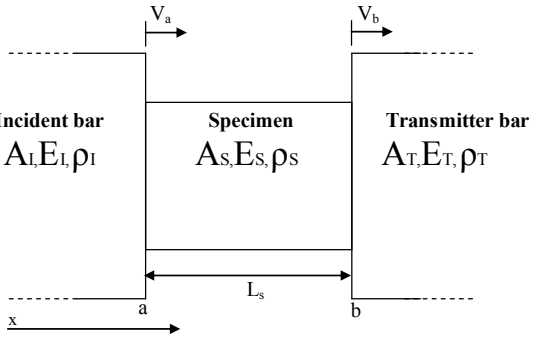

Figure 5.4 Schematic of the specimen situated between the Incident and Transmitter bars

L_s is the specimen length, and V_a and V_b are the interface velocities. The following derivation follows Kolsky [68] and Meyer et al. [3]. An alternative way to derive the formulas is found in [71]. In the equations the waves are named as

- Incident wave ε_I and σ_I
- Reflected wave ε_R and σ_R
- Transmitted wave ε_T and σ_T

According to D'Alembert's solution in equation (1.5), the velocity at a material point affected by traveling waves is the sum of the positive and negative traveling strain waves multiplied by the elastic wave velocity of the material. The incident wave reflects at interface (a), and during the entire test the velocity of interface (a) is calculated from

$$V(a,t) = C_I\big(\varepsilon_I(t) - \varepsilon_R(t)\big) \tag{5.3}$$

For the Transmitter bar the velocity of interface (b) becomes

$$V(b,t) = C_T\varepsilon_T(t) \tag{5.4}$$

The specimen undergoes deformation due to the velocity gradient over the specimen from V(a,t) and V(b,t), and the technical strain rate becomes

$$\frac{d\varepsilon}{dt} = \dot{\varepsilon}(t) = \frac{V(a,t) - V(b,t)}{L_s} \tag{5.5}$$

Inserting equations (5.3) and (5.4) into (5.5) yields

$$\dot{\varepsilon}(t) = \frac{1}{L_s}\Big(C_I\big(\varepsilon_I(t) - \varepsilon_R(t)\big) - C_2\varepsilon_T(t)\Big) \tag{5.6}$$

The strain at time t is found by integrating the strain rate from zero to time t as

$$\varepsilon(t) = \frac{1}{L_s}\int_0^t C_1\big(\varepsilon_I(\tau) - \varepsilon_R(\tau)\big) - C_2\varepsilon_T(\tau)\,d\tau \tag{5.7}$$

Linear elasticity and D'Alembert's solution give the forces specimen/bars interfaces

$$P(a,t) = A_I E_I(\varepsilon_I(t) + \varepsilon_R(t))$$
$$P(b,t) = A_T E_T(\varepsilon_T(t)) \tag{5.8}$$

The interface stresses then become

$$\sigma(a,t) = \frac{A_I E_I}{A_s}\big(\varepsilon_I(t) + \varepsilon_R(t)\big)$$
$$\sigma(b,t) = \frac{A_T E_T}{A_s}(\varepsilon_T(t)) \tag{5.9}$$

The stress in the specimen is the average of the interface stresses

$$\bar{\sigma}_s(t) = \frac{A_I E_I(\varepsilon_I(t) + \varepsilon_R(t)) + A_T E_T(\varepsilon_T(t))}{2A_s} \tag{5.10}$$

Equations (5.7) and (5.10) form the solution for calculating average stress and strain in the specimen without assumption of equal bars and stress equilibrium in the specimen. Kolsky discovered the technique of placing the strain gages on the Incident bar and Transmitter bar at the same distances from the specimen on the Incident and Transmitter bar. Then the Reflected and Transmitted wave would arrive at the same time at their respective strain gages, which time-synchronized them. Then Kolsky assumed stress equilibrium in the specimen such that forces P(a,t) and P(b,t) on each side of the specimen were equal.

$$P(a,t) = P(b,t) \tag{5.11}$$

Inserting equation (5.8) into (5.11) yields

$$A_I E_I\big(\varepsilon_I(t) + \varepsilon_R(t)\big) = A_T E_T(\varepsilon_T(t))$$
$$\varepsilon_I(t) + \varepsilon_R(\mathrm{t}) = \mathrm{K}\varepsilon_T(t) \tag{5.12}$$

with K given as

$$K = \frac{A_T E_T}{A_I E_I} \tag{5.13}$$

If the Incident bar and Transmitter bar are made from the same material and have the same diameter, then K=1and equation (5.12) reduces to

$$\varepsilon_I(t) + \varepsilon_R(t) = \varepsilon_T(t) \tag{5.14}$$

Further, the wave velocities in the Incident and Transmitter bars are equal as

$$C_I = C_T \tag{5.15}$$

Inserting equation (5.14) and (5.15) into (5.7) and eliminating the Incident stress, the strain rate calculation reduces to

$$\dot{\varepsilon}(t) = -\frac{2C_I}{L_s}\varepsilon_R(t) \tag{5.16}$$

The strain history is obtained by integration of equation (5.16)

$$\varepsilon(t) = -\frac{2C_I}{L_s}\int_0^t \varepsilon_R(t)\,dt \tag{5.17}$$

Inserting (5.14) and (5.15) into equation (5.10) and eliminating the Incident stress, the specimen stress calculation reduces to

$$\sigma(t) = \frac{A_I E_I}{A_s} \varepsilon_T(t) \tag{5.18}$$

In this case, the specimen stress only depends on the Transmitted wave, while the strain only depends on the reflected wave. The stress and strain calculations are decoupled from each other and the time-synchronization is done by the positioning of the strain gages. Alternatively, the Reflected wave or the Transmitted wave can be eliminated from equation (5.14) instead of the Incident wave. This forms two new sets of equations, which depend on different waves. The original Kolsky formulas are named "One wave 1" in Table 5.1 while the two alternative formulations are named "One wave 2" and "Two waves". "One wave 2" only depends on the Incident and Transmitted waves, which allows alternative arrangements of the strain gage for increased measurement durations [76]. The "Two waves" formulation uses two waves for calculation of the stress history, hence its name "Two waves". The "Three waves" analysis uses all three waves and does not assume stress equilibrium, but assumes equal bars. If the waves are not time-synchronized by the gage positioning then they are time-synchronized manually before applying the equations in Table 5.1. The "Foot shifting" method is when the Transmitter wave is shifted to rise at the same time as the Incident and Reflected wave. This manual synchronization is easier to perform, but the method introduces a higher degree of error in the calculations [77]. The "modern" method refers to the case where no assumptions of equal bars and stress equilibrium are made in the calculations. The stress and velocity at the ends of the specimen are calculated separately and used to calculate average stress and strain. The Incident and Transmitter bars can be of different materials and with different diameters, which is preferable for testing, for example, soft materials [69].

Table 5.1 Formulas to post process SHPB data – Table partly adopted from Zhang et al. [73]

Name	**Stress history σ(t)**	**Strain history ε(t)**	**Waves used**	**Assumptions**	
				$C_I = C_T$	$\varepsilon_I + \varepsilon_R = \varepsilon_T$
One wave 1	$\sigma(t) = \frac{A_I E_I}{A_s}\varepsilon_T(t)$	$\varepsilon(t) = -\frac{2C_I}{L_s}\int_0^t \varepsilon_R(t)\,dt$	$\varepsilon_R, \varepsilon_T$	x	x
One wave 2	$\sigma(t) = \frac{A_I E_I}{A_s}\varepsilon_T(t)$	$\varepsilon(t) = \frac{2C_I}{L_s}\int_0^t \varepsilon_I(\tau) - \varepsilon_T(\tau)\,d\tau$	$\varepsilon_I, \varepsilon_T$	x	x
Two waves	$\sigma(t) = \frac{A_I E_I}{A_s}\varepsilon_I(t) + \varepsilon_R(t)$	$\varepsilon(t) = -\frac{2C_I}{L_s}\int_0^t \varepsilon_R(t)\,dt$	$\varepsilon_I, \varepsilon_R$	x	x
Three waves	$\sigma(t) = \frac{A_I E_I}{2A}(\varepsilon_I(t) + \varepsilon_R(t) + \varepsilon_T(t))$	$\varepsilon(t) = \frac{C_I}{L_s}\int_0^t (\varepsilon_I(\tau) - \varepsilon_R(\tau) - \varepsilon_T(\tau))\,d\tau$	$\varepsilon_I, \varepsilon_R, \varepsilon_T$	x	
Foot shifting	$\sigma(t) = \frac{A_I E_I}{2A}(\varepsilon_I(t) + \varepsilon_R(t) + \varepsilon_T(t + t_0))$	$\varepsilon(t) = \frac{C_I}{L_s}\int_0^t (\varepsilon_I(\tau) - \varepsilon_R(\tau) - \varepsilon_T(\tau + t_0))\,d\tau$	$\varepsilon_I, \varepsilon_R, \varepsilon_T$	x	
Modern	$\sigma(a,t) = \frac{A_I E_I}{A_s}(\varepsilon_I(t) + \varepsilon_R(t))$ $\sigma(b,t) = \frac{A_T E_T}{A_s}(\varepsilon_T(t))$	$\varepsilon(t) = \frac{1}{L_s}\int_0^t C_I(\varepsilon_I(\tau) - \varepsilon_R(\tau)) - C_T\varepsilon_T(\tau)\,d\tau$	$\varepsilon_I, \varepsilon_R, \varepsilon_T$		
Hybrid analysis	One of the above	Direct measurement (DIC etc.)	$\varepsilon_I, \varepsilon_R, \varepsilon_T$	(x)	(x)

Figure 5.5 shows the schematic difference between the "Classic SHPB" and the "Modern SHPB". In the classis set-up (Kolsky), the Incident bar and the Transmitter bar are equal and the strain gages are placed at equal distance from the specimen. In the modern SHPB, the bars can be of different materials and different diameters and the strain gages can be placed at different distances from the specimen. The Modern SHPB requires manual time-synchronization and the calculation of separate stress and velocities on each side of the specimen.

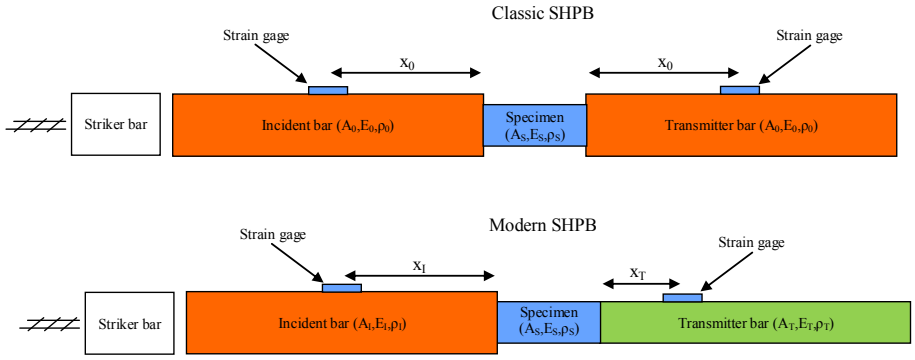

Figure 5.5 The classic and modern SHPB setup. Subscript I and T in the modern SHPB indicate the individual properties of the bars.

5.2 Pulseshaping

If the Striker bar and Incident bar have completely flat ends a nearly square is created upon impact. However, shaped incident waves with increased rising times facilitate stress equilibrium and constant strain rate [18, 20, 69, 74].

Christensen et al. [78] introduced pulse shaping to the compressive SHPB by using a conical striker bar with examples given in Figure 5.6. Recently, Baranowski et al. [79] performed a numerical study of the conical striker to optimise the Striker shape to different Incident wave shapes. Ellewood et al. [80] added an extra Incident bar and positioned a specimen similar to the test specimen between the two Incident bars. The square Incident waves travelled down the first Incident bar and the extra specimen would then smooth the square wave into the second Incident bar as a shaped Incident wave with a long rise time.

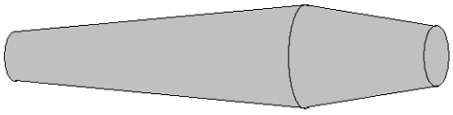

A) Conical striker [18]

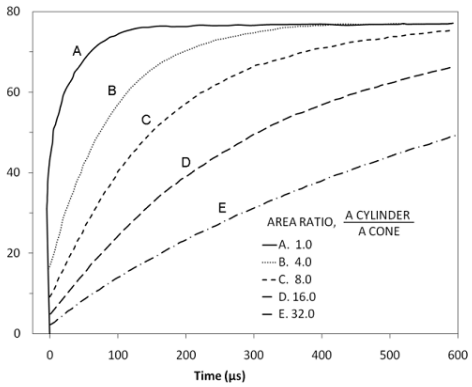

B) Incident waves produced by varying the area ratio between the cylinder and cone [18, 78]

Figure 5.6 Pulse shaping technique – Conical striker bar

Nasser et al. [74] modified the method by Ellwood et al. [80] by removing the extra Incident bar and exchanged the extra specimen with a soft elasto plastic material such as copper. The Striker bar would then hit the copper disc directly, which worked as pulse shaper. By varying the diameter and thickness of the copper disc, Nasser et al. were able to obtain different Incident wave shapes. Nasser et al. did also describe the deformation process analytically and the description was extended and improved by Frew et al. [20, 21]. The analytical description allowed the

experimenter to predict the shape of the Incident wave from the pulse shaper dimensions and the Striker bar length and velocity. The method was later developed into dual pulse shaping with two pulse shapers on top of each other to create a bi-linear Incident wave [18]. Gerlach et al. [81] have recently presented a new method of pulse shaping where an extra Incident bar with grooves creates a set of impedance mismatched, which the incident wave has to pass. The mismatch creates a series of reflections that smooth the wave.

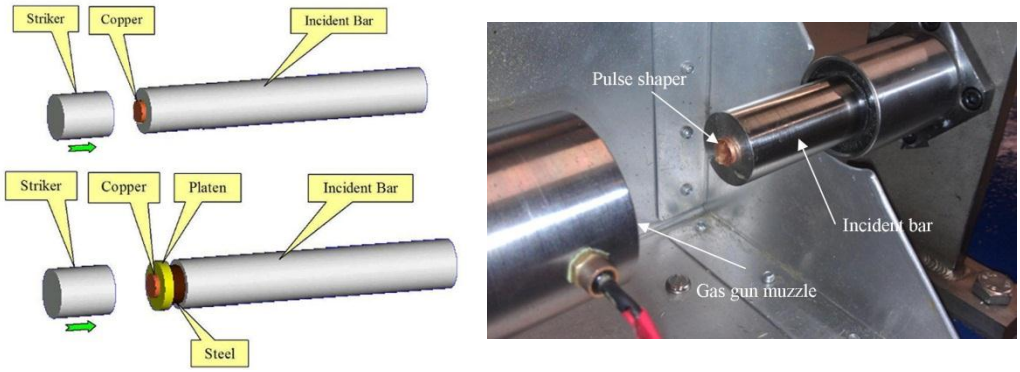

A) Schematics of a single and dual pulse shaper setup *B) Example of the copper disc pulse shaper placed at the Incident bar*

Figure 5.7 Pulse shaping method with a cushion material.

The method with a copper disc as cushion material between the striker bar and the Incident bar has been widely used in the literature [20, 21, 69, 70, 74, 75, 82-84] and is employed in this work. The next section describes the calibration and utilization of the method.

5.2.1 Copper disc pulse shaper

This section describes the analytical model developed by Nasser et al. and Frew et al. [20, 74] and the implementation of the method. The assumptions of the model are

- The striker bar and Incident bar have equal diameters
- The pulse shaper does not deform plastically to a larger diameter than the Incident bar

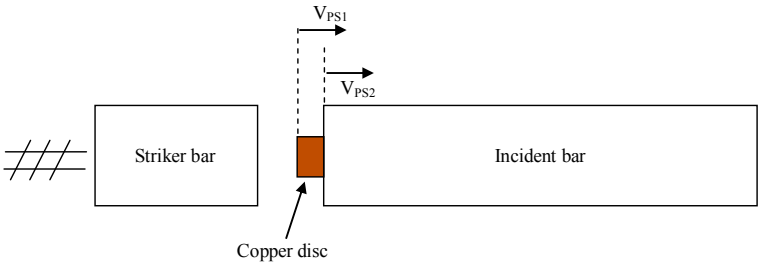

Figure 5.8 Schematic of the copper disc placed at the Incident bar with the interface velocities V_{PS1} and V_{PS2}.

The copper disc has initial thickness $h_{0p,}$ and cross sectional area A_p. The striker bar has density ρ_{ST}, elastic wave speed C_{ST}, length L_{ST}, and impact velocity V_0. Upon impact the copper disc deforms plastically while a compressive wave travels back through Striker bar. The relationship between time t and strain ε in the copper disc is given by

$$t = \frac{h_{0p}}{V_0}\int_0^{\varepsilon} \frac{1}{\left[1 - K'\left(\frac{1}{\rho_I C_I} + \frac{1}{\rho_{ST} C_{ST}}\right)\frac{f(x)}{1-x}\right]} dx, \qquad 0 \le t < T \tag{5.19}$$

f(x) is a function for the copper disc that gives the stress as function of strain. K is defined as

$$K = \frac{\sigma_0 A_{0p}}{V_0 A_{ST}} \tag{5.20}$$

σ_o is a constant. The time T to traverse the specimen is calculated as

$$T = \frac{L_{ST}}{C_{ST}} \tag{5.21}$$

The deformation of the copper disc may continue for several round trips of the wave in the striker bar and the time as function of strain is given by

$$t = nT + \frac{h_0}{V_0}\int_{\varepsilon_n}^{\varepsilon} \frac{1}{\left[1 - K\left(\frac{1}{\rho_T C_T} + \frac{1}{\rho_{ST} C_{ST}}\right)\frac{f(x)}{1-x}\right] - \frac{2K}{\rho_{ST} C_{ST}}\sum_{k=1}^{n}\frac{f(\varepsilon(t-kT))}{1-\varepsilon(t-kT)}} dx, \quad nT \le t < (n+1)T \tag{5.22}$$

ε_n is the strain at t = nT. The pulse shaper compresses when $V_{PS1} > V_{PS2}$. When $V_{PS1} < V_{PS2}$ equations (5.19) and (5.22) are no longer valid and the pulse shaper is assumed to be elastic unloading. The interface velocities V_{PS1} and V_{PS2} are calculated from equations (24a) and (24b) in [21]. Frew et al. suggested a resistance function for the copper disc as

$$\sigma_p = \frac{\sigma_0 \varepsilon_p^n}{1 - \varepsilon_p^m} \tag{5.23}$$

The function is calibrated by an end-point method. A series of tests were conducted and after each test, the maximum strain was derived from the final thickness of the copper disc. The associated maximum stress (σ_p) was found from the generated Incident wave as

$$\sigma_p = \frac{E_I A_I}{A_P}\left(1 - \varepsilon_p\right) \cdot \max(\varepsilon_I(t)) \tag{5.24}$$

The acquired data were plotted in a stress strain plot and equation (5.23) was fitted to the data point in a least square sense to determine n, m, and σ_0.

A soft grade stock copper was available in sheets of thickness of 0.5, 1, 1.5, 2 and 3mm. Round discs were created in various diameters d_0 between 3 and 15 mm with a punch machine available in the tool shop. This is laboratory practice to create copper disc pulse shapers as noted by Nishida et al. [85].

A) Copper sheets after punching

B) Different size pulse shapers between 3 and 15mm after test

C) Striker bars in lengths of 50mm, 100mm, 150mm and 200mm made from stainless steel. The Incident bar was made from the same material.

Figure 5.9 Copper discs and available strikers. The Teflon coating shown together with the Striker bars, was used for lubricating the barrel of the gas gun and is. Lubrication, as WD40, is not preferred as the tight tolerances in the barrel causes the oil to pile up in front of the Striker bar and disturbs the impact.

In total, twenty tree tests were used to calibrate the resistance function in equation (5.23). L_{ST}, d_0, h_{0p} and V_0 were varied between the tests to spread the data point along the line. Figure 5.10A gives the plot with the fitted function along with the estimated parameters of equation (5.23). Figure 5.10B shows a schematic overview of pulse created with a copper disc pulse shaper [86]. Part 1 is the elastic response of the pulse shaper. Part 2 is the plastic response and part 3 is the rigid response where the pulse shaper is maximum compressed. Part 4 is elastic unloading of the pulse shaper. An example of a measured Incident wave and a simulated wave is shown in Figure 5.10C. The measured wave does not have the initial elastic response as the simulated curve, which indicates that some form of damping was present at the impact.

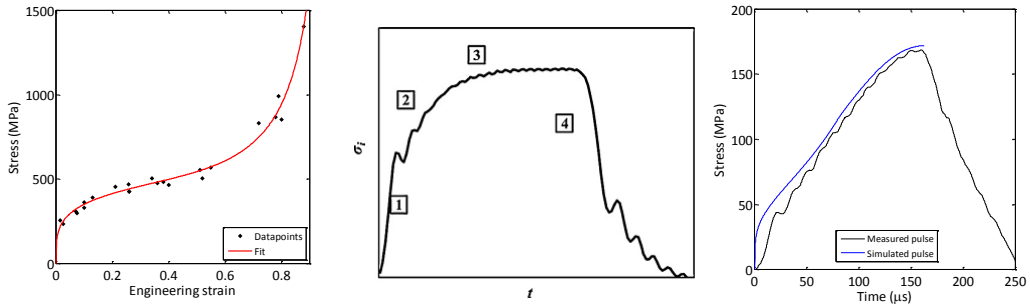

A) Fitted resistance function σ_0=608.3, m=4.236, n=0.2387.

B) Schematic graph of a shaped incident wave using a copper disc. Adopted from [86]

C) An example of a simulated and the corresponding measure Incident wave.

Figure 5.10 Pulse shaping with a copper disc

There are four parameters that control the shape of the Incident wave: V_0 = striker bar impact velocity; L_{ST} = the striker bar length; h_0 = the pulse shaper thickness; and d_0 = the pulse shaper diameter. Figure 5.11 shows a parametric study the shaped incident wave was simulated for a set of parameters.

Increased impact velocity increases the stress imposed on the pulse shaper. If in the impact velocity is high enough, the pulse shaper compresses enough to go into a strain region ($\varepsilon_{tech} > 0.6$) with a very steep increase of stress as seen for V_0 = 25m/s. An increasing striker bar length extends the pulse duration and forces the pulse shaper to higher strains. If the striker bar is long enough, the pulse shaper compresses to strains beyond 0.6 and the pulse becomes highly nonlinear. This is seen for L_{ST} = 300mm.

An increasing diameter causes the initial elastic response to be higher, as the pulse shaper exerts a

higher force on the Incident bar before the pulse shaper yields. If the striker bar length and velocity are kept constant, an increased diameter decreases the amount of plastic strain. Thus, the response grows in amplitude with increased diameter but moves backwards on the pulse shaper stress strain curve in Figure 5.10B.
An increased thickness lowers the amplitude of the generated pulse but extends the pulse duration. The increased thickness leads to a softer response, which gives a lower deceleration of the striker bar and thus a longer time in contact with the striker bar. The higher thickness also means that the induced strain is less and the pulse shaper is not loaded so far up its stress strain curve and keeps the amplitude low on the generated wave.

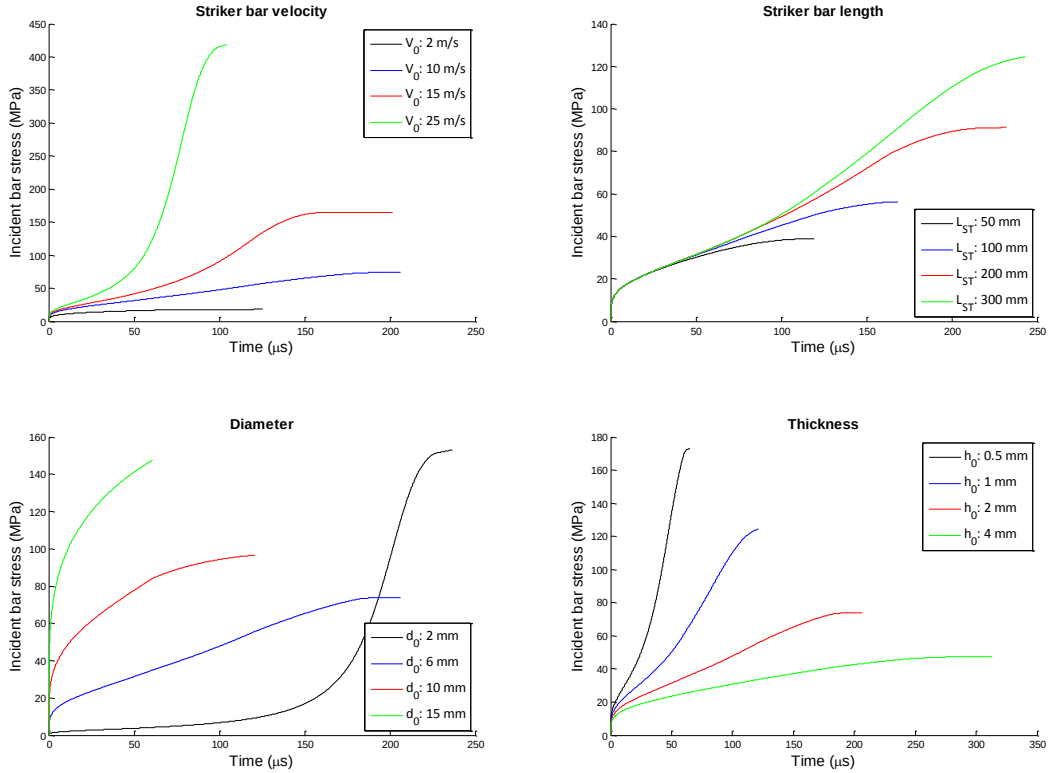

Figure 5.11 Parameter study of the four parameters. The basic set of parameters are the striker bar velocity V_0, the striker bar length, the pulse shaper diameter and the pulse shaper thickness.

Rising Incident waves with approximately constant and different stress rate can be generated by varying the four parameters. The copper disc method has limitations with respect to generating a monotonic rising pulse, required for a smooth loading of the specimen. If the parameters are misadjusted, the generated stress wave increases in rate at the last part. This happens when the pulse shaper is deformed into a strain range with high effective modulus taken as the slope of the stress strain curve in Figure 5.10B. This is seen in Figure 5.12 for copper with d_0 = 6mm compared with d_0 = 7.4 mm which has a more linear stress rate. As illustrated in Figure 5.11, the increased diameter decreases the maximum strain in the pulse shaper, but increases the initial elastic response as seen here. The straightforward way to increase the stress rate would be to increase the diameter and adjust the other parameters accordingly to obtain a linear response of required duration. However, the model presented by Frew et al. [21, 74] does not account for friction. For the combination of the bars and copper material used in this study the limiting diameter was about 11-12mm. At higher diameters, severe ripples were created in the Incident wave. This causes an oscillating strain rate and addition of high frequency content to the wave.

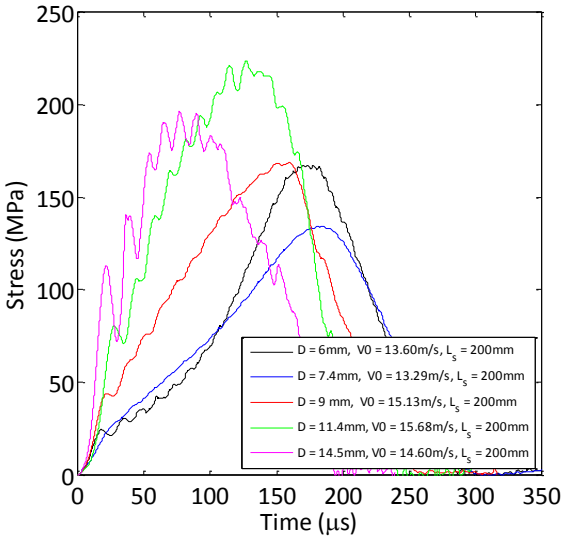

Figure 5.12 Various diameters (D) of 2mm thick copper disc tested under similar conditions.

A series of tests were carried out to determine the controlling parameters of the ripple problem. Figure 5.13A shows that at 1mm thickness the ripple problem only persists at diameters above 10mm. Figure 5.13B shows that increased impact velocity does not provoke the ripples to occur. In this case, the diameter and thickness were fixed and the impact velocity varied. Figure 5.13C shows that the increased thickness does not damp the ripple problem when the diameter was increased up to the critical dimensions. The repeated test in Figure 5.13C shows that the ripple problem persists and is not random.

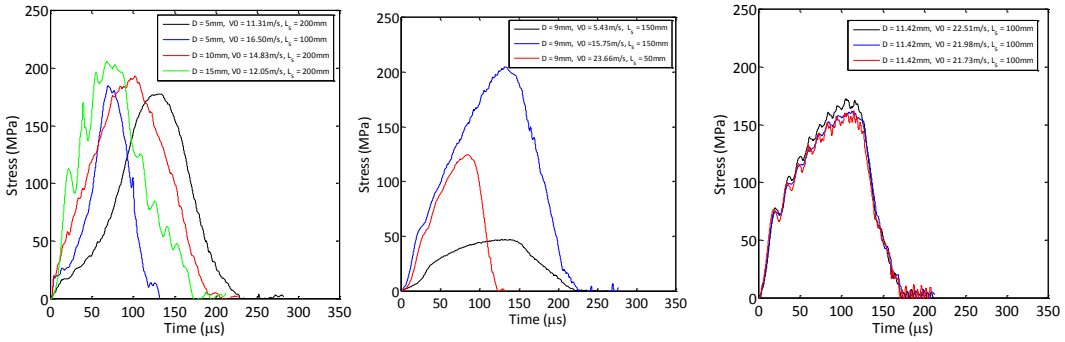

A) 1 mm thick copper discs *B) 2mm thick copper discs* *C) 3mm thick copper discs*

Figure 5.13 Investigation of "ripples". Pulse shapers were tested under various conditions to narrow down the controlling parameters of ripples.

The results in Figure 5.13 show that the diameters is the controlling parameter. Several lubricants, such as grease, MoS2, and thin plastic foil were tried, but did not damp the ripples in a reproducible way. The compression of the pulse shaper resembles a compression test of ductile materials in the SHPB so inspiration from these tests was searched for in the literature. An accepted design to balance inertia problem is a ratio $h_0/d_0 = 0.47$ [87] for a material with Poisson ratio of 0.3. The 11.42mm diameters discs of 3mm thickness had an h_0/d_0 ratio of 0.263. If friction were of concern then the h_0/d_0 ratio should be between 1.5 and 2 to minimize the effect of friction

on the result [88], but this is with respect to the measured signal and not with respect to ripples in the signal. An h_0/d_0 ratio in this range is not feasible for pulse shapers as the generated waves will have too small amplitude. Naghdabadi et al. [86] performed LS Dyna simulations of copper disc pulses shapers. Their simulations showed the ripples as function of the diameter, but the authors did not address the reason for the ripples or mention them as a problem. Figure 5.14 shows some of the simulations.

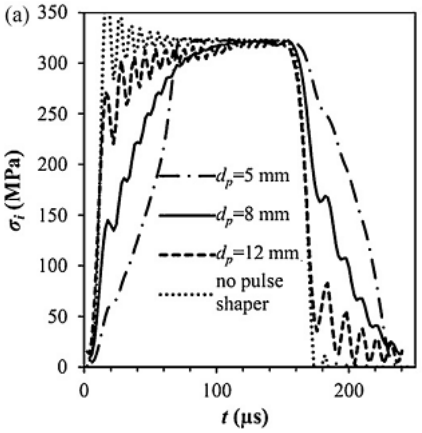

Figure 5.14 LS Dyna simulation of pulse shapers. h_p*= 1mm,* V_0 *= 16m/s,* L_{ST} *= 400mm* [86].

Then the pulse shaper method with a copper disc as cushion material between the striker bar and the Incident bar is limited by the frictional properties between the pulse shaper and the striker and Incident bars. The pulse shaper diameter controls the initiation of the ripple problem. For the specific combination materials used in this study the maximum diameter was around 10-11mm before the Incident wave got to large ripples.

5.3 Calibration of the SHPB setup

Post processing of the data acquired from an SHPB test requires the elastic modulus and the density to calculate the elastic wave velocity. Any error in these values propagates directly into the calculated values of stress and strain. Lifshitz et al. [89] examined the required accuracy of the elastic wave velocity of the incident and Transmitter bar and found that just a 1% deviation caused errors in the post-processed results as shown in Figure 5.15. They advised against using tabular values for density and the elastic modulus, but instead do a calibration.

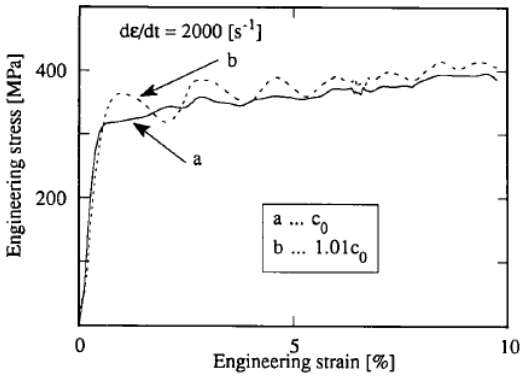

Figure 5.15 Effect of the accuracy of the elastic wave velocity C_0 on the stress strain curve [89].

The density (ρ) can be determined by measuring the weight and the dimensions of the bar. The elastic modulus E is estimated either from a tensile test, or by measuring the elastic wave velocity and applying $C = \sqrt{\frac{E}{\rho}}$. The SHPB test rig itself can conveniently be used to measure the wave velocity. In the Incident bar, the strain gage is positioned at distance L_{SGI}. Figure 5.16A shows a typical recording from the strain gage with the Incident and Reflected waves in the signal. The time Δt is the time it takes the Incident wave to propagate to the specimen and the Reflected wave to come back to the strain gage again. The elastic wave velocity can then be estimated as [18]:

$$C_B = \frac{2L_{SGI}}{\Delta t} \tag{5.25}$$

Δt is normally measured manually by the experimenter by determining when the Incident and Reflected pulses rise as indicated in Figure 5.16A. The estimate of Δt relies on the experimenter's ability to judge where the signals start and end and is a source of error. In Figure 5.16B the effect of judging the time 1μs/5μs wrong is shown as a function of the strain gage position and this should be compared to the time scale in Figure 5.16A. The estimation of the elastic wave velocity is then strongly dependent on the noise level in the signal and the experimenter's ability to judge where the wave rises.

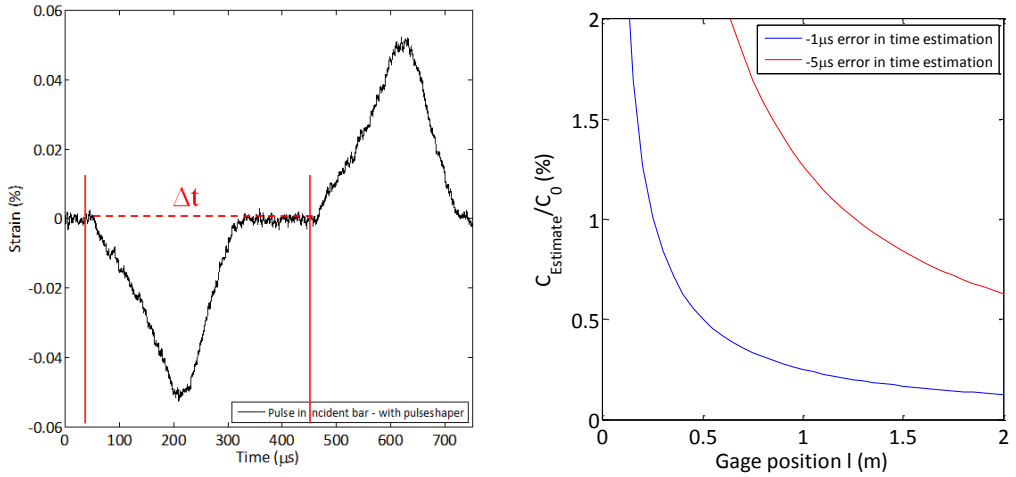

A) Example of Incident and reflected pulse in the Incident bar for gage position of l=1m. Δt is the time it takes the wave to travel to the end of the bar and back to the strain gage.

B) Error in estimated C_0 if time is estimated 1 µs/5 µs wrong for a real elastic wave velocity of 5000m/s.

Figure 5.16The incident and reflected wave in the Incident bar and the error in estimating the elastic wave velocity

5.3.1 Alternative method for estimating C_0

To remove the dependency on the experimenter's ability to judge the start of the incident and reflected wave, an alternative method can be used to estimate the wave velocity. The method exploits the longitudinal resonance phenomena of a bar [16].

Assume the Incident wave can move freely without contact to the specimen or the Transmitter bar. The impact of the striker bar creates a compressive wave traveling in the positive direction x of the Incident bar as indicated in Figure 5.17. At the free end of the bar, the wave reflects completely and returns as a tensile wave traveling in the negative direction. At left the end, it reflects and travels in the positive direction as a compressive wave again. This process continues until external and internal friction has reduced the amplitude of the wave to zero, and the bar is at rest.

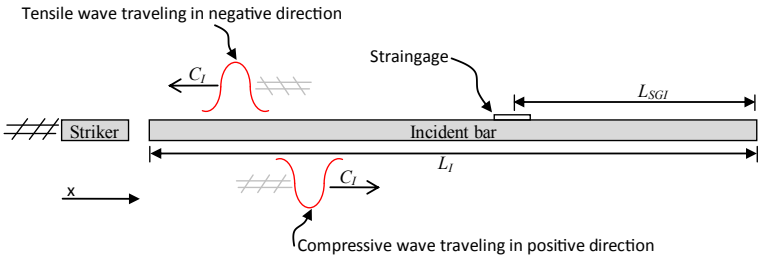

Figure 5.17 Schematic of the wave traveling inside the Incident bar. The striker bar impact creates a compressive wave, which travels in the positive direction. As the wave reflects at the other end it return as tensile wave traveling in the negative direction.

The strain gage at the Incident bar records both the compressive and tensile waves, and the time it takes the wave to reach back to the strain gage as a compressive wave after last time it passed as a compressive wave is marked with a red arrow in Figure 5.18A. The red arrow represents the

period T, which equals the time it takes the wave to travel $2L_I$. The inverse of the period gives the frequency so the frequency of the signal in Figure 5.18A yields

$$f_I = \frac{C_I}{2L_I} \tag{5.26}$$

The frequency is found by a Fourier transformation of the strain gage signal. The frequency corresponding to the wave velocity which will have the highest energy in the frequency domain. The strain gage signal in Figure 5.18A was obtained on a bar of stainless steel with a measured density of 7741kg/m^3 and a length 2.001m. The wave speed should be around 5000m/s such that the frequency should be around $\frac{5000m/s}{2.001m*2} = 1250Hz$. Figure 5.18B shows the frequency spectrum of the signal in Figure 5.18A.

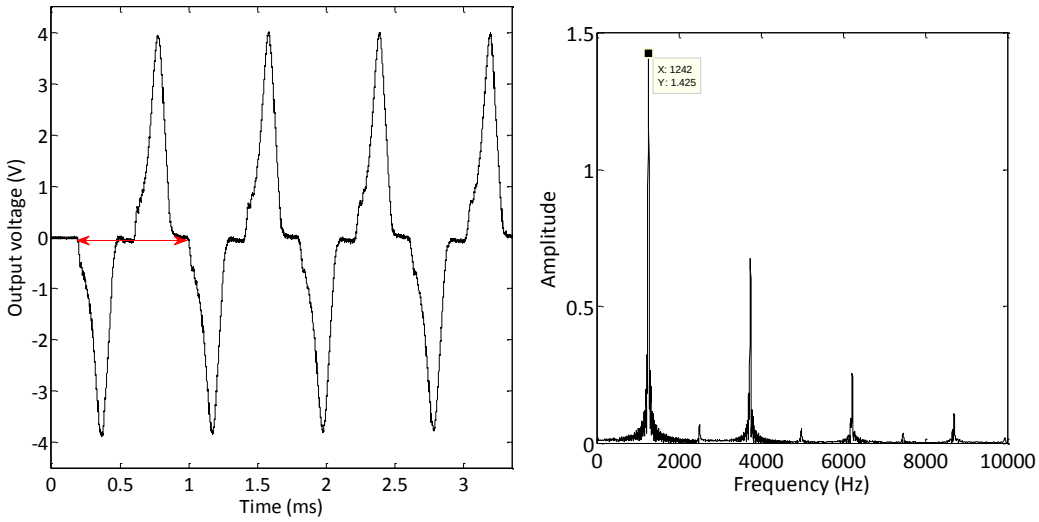

A) Period of the signal marked with an red arrow *B) Frequency spectrum of signal shown in (A)*

Figure 5.18 A signal from the Incident bar along with its representation in the frequency domain.

There is a clear peak at 1242Hz, which corresponds to a wave velocity of 4970 m/s. There are peaks at frequencies that are multiples of 1242Hz but these are harmonics and should be ignored. Thus, an algorithm can be set up that transfers the strain gage signal from the time domain to frequency domain, and then performs a search for the highest peak near the expected frequency of the wave velocity. The expected frequency is calculated from tabular values of the elastic modulus, the density, and the measured bar length.

The method is proved to be robust because the dependency on the experimenter's judgement of the signal is removed. Further, the method is also immune to noise as the energy of the noise will be less than that of the wave velocity frequency and be of higher frequency. The strain gage signal is discretely sampled in time at sampling frequency fs. The Fourier transformation then becomes a discrete sampling of the underlying analogue frequency spectra. If the signal length in data points is N then the resolution of the frequency spectra yields

$$\Delta f = \frac{f_s}{N} \tag{5.27}$$

The sampled length N should be maximised to increase the accuracy of the method. In this work a resolution was 1Hz. Instead of recording longer signals, the signal can be padded with zeroes to increase the resolution. For this work, an Incident bar and a Transmitter bar were calibrated using

the proposed method. The density was determined by measuring the dimensions and the weight three times and the average values were used. The wave velocity was calibrated through 10 tests to estimate the stability of the method. Table 5.2 shows the results. The wave velocities were estimated with a 95% confidence interval of ±2m/s, which is a relative error of ±0.04%. Thus, the method outperforms the manual method in precision and accuracy. The experimenter will have to select the correct period with a precision better than 0.15μs for strain gage position of 1m to reach a relative error of 0.04%.

Table 5.2 Calibration values for the incident and Transmitter bar.

Parameter	Incident bar	Transmitter bar
Material	Stainless steel	Aluminium
Length	2001mm	617mm
Diameter	25.02mm	24.99mm
weight	7.616kg	0.85kg
Calculated density	7741 kg/m^3	2809kg/m^3
Estimated wave velocities		
Test 1	4974 m/s	5105 m/s
Test 2	4974 m/s	5111 m/s
Test 3	4974 m/s	5110 m/s
Test 4	4982 m/s	5111 m/s
Test5	4978 m/s	5115 m/s
Test 6	4970 m/s	5107 m/s
Test 7	4970 m/s	5116 m/s
Test 8	4972 m/s	5112 m/s
Test 9	4972 m/s	5111 m/s
Test 10	4976 m/s	5106 m/s
Average	4974 m/s	5110 m/s
95% confidence interval	4972 < C_I < 4976 m/s	5108 < C_T < 5112 m/s
Elastic modulus	191GPa	73.5GPa

5.4 Time synchronisation

The Incident wave is recorded before the deformation takes place and the reflected and transmitted wave are recorded after the deformation took place. However, during the deformation, the waves are present at the specimen at the same time. To perform the post processing of the signals, the waves must be offset in time to be aligned as they would if they were recorded directly at the specimen ends. In the classical SHPB, the signals are automatically aligned since there is the same distance from the specimen to the strain gage on both bars. In a modern SHPB with different strain gage positions, the signals need to be synchronized after the test. In this work the rise of the incident wave was chosen as the synchronization point. If the rise of the incident wave is taken as T_0 on a global timescale T, then according to [18] the reflected wave rises at the strain gage at

$$T_{Rtot} = T_0 + T_R = T_0 + \frac{2L_{SGI}}{C_I} \tag{5.28}$$

The transmitted wave then rises at

$$T_{Ttot} = T_0 + T_T = \frac{L_{SGI}}{C_I} + \frac{L_{SGT}}{C_T} + \frac{L_s}{C_s} \tag{5.29}$$

L_{SGT} is the gage position on the Transmitter bar with respect to the specimen, C_T the wave velocity of the Transmitter bar, L_s the specimen length and C_s the specimen wave velocity.
The reflected wave is synchronized by shifting the time of all data recorded on the Incident bar

after T_{Rtot} as

$$T_{R_{shifted}} = T - T_R \tag{5.30}$$

The transmitted wave is synchronized by shifting the vector of all data by

$$T_{T_{shifted}} = T - T_T + \frac{L_s}{C_s} \tag{5.31}$$

The transmitted wave cannot be shifted $\frac{L_s}{C_s}$ backwards as this travel time through the specimen was present at the time when the actual deformation took place. However, if extra shifting is done and T_T alone is used for time shifting, the method is called foot shifting and causes higher errors in the estimated stress-strain curves [77].
Finally, the shift value for the transmitted waves becomes

$$T_{Tc} = T_T + \frac{L_s}{C_s} = \frac{L_{SGI}}{C_I} + \frac{L_{SGT}}{C_T} \tag{5.32}$$

The shift value for the reflected wave becomes

$$T_R = \frac{2L_{SGI}}{C_I} \tag{5.33}$$

Figure 5.19A shows the shift times in relation to each other and the raw waves. Figure 5.19B shows the waves after the shifting was performed.

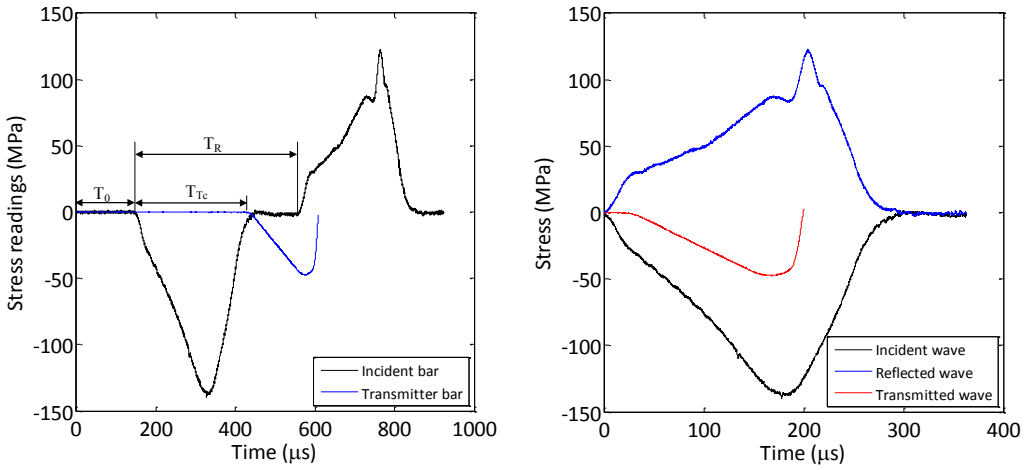

A) Stress reading from the incident and Transmitter bar. *B) Waves after synchronisation.*

Figure 5.19 Synchronisation of the Incident, Reflected and Transmitted wave.

The synchronization can only be done successfully if the wave velocities and strain gage position are measured with high precision. Otherwise, the synchronization leads to erroneous results in the post processing process.

5.5 Dispersion correction

A stress wave propagating along a slender bar can be expressed as a sum of harmonic waves with different amplitudes, periods and phases. The SHPB post processing procedures assume simple 1D

wave theory which states the wave velocity of a harmonic sinusoidal wave in an elastic rod to be calculated by $C = \sqrt{E/\rho}$. However, if the theory is expanded to 3D analysis including Poisson effect, lateral material movement and inertia are also introduced. The general 3D theory for propagation of sinusoidal longitudinal waves in long slender bars was derived by Pochhammer and Chree [67, 90] and concluded that the sinusoidal wave velocity depends on

- R - The bar radius
- Λ - Wave length
- C_0 - Wave velocity of infinitely long wave – 1D wave velocity.
- N - Poisson's ratio of the bar material

The original equations are complex and have an infinitely number of solutions corresponding to the different vibrational modes of the bar. The first mode (solution), is vibration in the longitudinal direction of the bar and is the dominating part in an SHPB test [72]. Figure 5.20 shows the exact solution of the Pochhammer-Chree equation to the three first vibrational modes of a longitudinal bar of infinite length. C is the wave velocity of a wave with wavelength Λ.

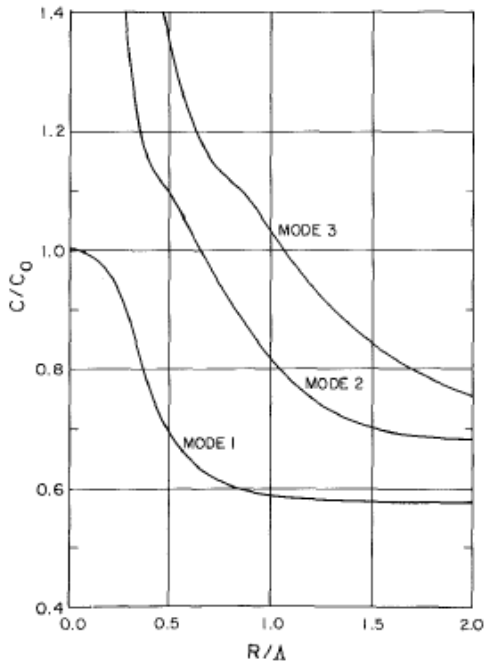

Figure 5.20 Exact Solution of the first 3 vibrational modes to the Pochhammer-Chree equation for bar material with v=0.3. Mode 1 is dominant in SHPB tests [72].

Figure 5.20 shows that wave components with wavelengths less than the bar radius travels 40-50% slower than waves with long wavelengths. Thus, high frequency content travels slower than low frequency content, resulting in a dispersion of the wave where the rising and falling edges are smoothed out and high frequency oscillation is superimposed on the original wave as shown in Figure 5.21 [90].

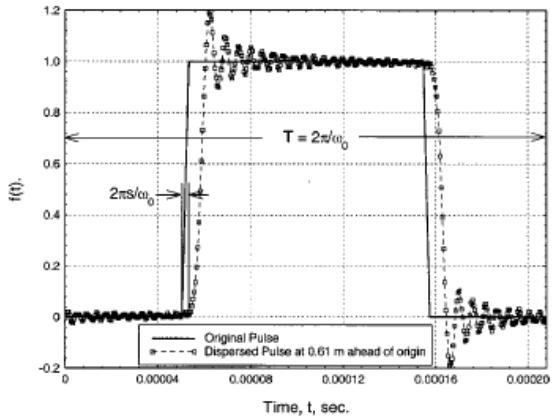

Figure 5.21 Initial sharp wave subjected to dispersion

The wave shape has an impact on the degree of dispersion, since a pulse with a short rise time has a wide frequency band with a higher amount of high frequency content, while a pulse with a smooth rising edge has a narrow low frequency band and suffers less from dispersion [91]. This is seen in Figure 5.22 where the frequency spectra were calculated for a square wave and a ramp wave recorded at the SHPB used in this work.

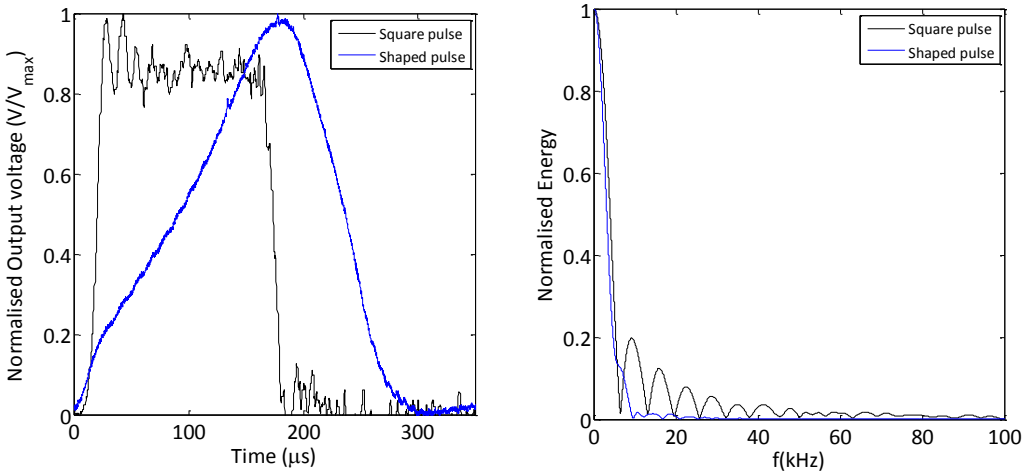

A) A square and pulse shaped incident wave *B) Frequency content*

Figure 5.22 Incident waves and their associated frequency content

According to the Pochhammer-Chree equations [67, 72], there is 3 main problems with dispersion

1. High frequency components travel with a slower propagation velocity than low frequency components.
2. Uneven distribution of stress across the cross sectional area of the bar as function of $\frac{R}{\Lambda_n}$
3. High frequency elastic modulus is different from the quasi-static elastic modulus.

Since dispersion corresponds to a phase shift as the wave travels, dispersion is corrected by performing a Fourier transformation of the wave to the frequency domain and a time shift of the phase angles for frequency in the wave. When the phase angles have been shifted, the pulse is shifted back into the time domain by an inverse Fourier transformation [91]. The incident wave is shifted forward in time as the wave changes after the strain is recorded and before the specimen is

loaded. The reflected wave and transmitted wave have to be shifted backwards as these waves are recorded after the specimen is loaded.
Andrew et al. [92] gave a step-by-step overview of the dispersion correction technique:

1. Convert the time-domain signal f(t) into the frequency domain
2. Derive the amplitude B(ω) and phase angle ϕ(ω) of each frequency component.
3. Calculate the phase velocity C(ω) of each frequency component.
4. For each frequency component, calculate the phase shift from the position at which the signal is recorded to some other point at an axial distance z from the recording position. z is taken positive in the propagation direction of the wave. The phase shift is ϕ'(ω) in radians is given by

$$\phi'(\omega) = \left(\frac{C_0}{C(\omega)} - 1\right)\frac{\omega z}{C_0} \tag{5.34}$$

5. Convert the signal back into the time domain using a corrected phase angle for each frequency

The dispersion correction is necessary if the frequency content in the bar is high. However, at lower frequencies the dispersion is not distinct. Figure 5.24 shows the phase velocity calculated from the 1D wave equation and the exact solution to the Pochhammer-Chree equations. As long as $\bar{\gamma} < 0.1$ there is a match between wave equation and the exact theory and thus this can be used as measure if dispersion correction is required.

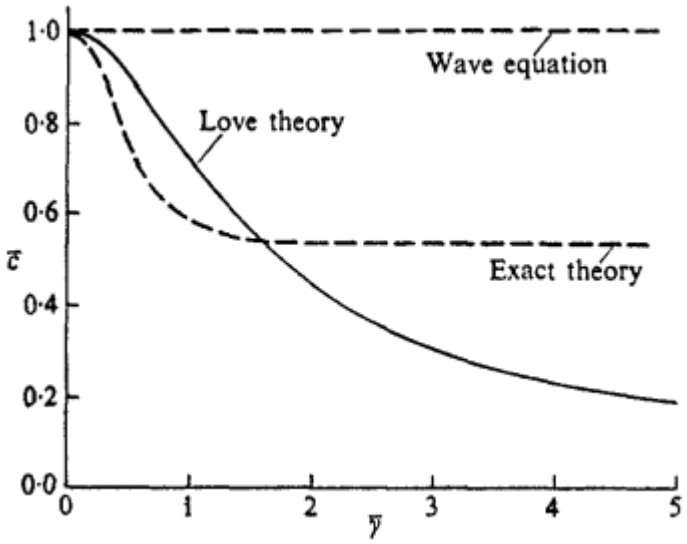

Figure 5.23 Variation of the phase velocity as function of the normalised wave number.

The normalized wavenumber is defined as

$$\bar{\gamma} = \frac{2\pi k v f}{C_0} \tag{5.35}$$

k is the polar radius of gyration calculated given by

$$k = \sqrt{\frac{J_{yy}}{A}} = \sqrt{\frac{\pi r^4}{2\pi r^2}} = \frac{r}{\sqrt{2}} \tag{5.36}$$

Figure 5.24 shows the maximum frequency as function of the bar radius for a material with C_0=5000m/s. Thus, for a 25mm bar the maximum frequency content should be less than 92 kHz. Comparing with Figure 5.22 the shaped Incident wave does not have much energy above 10 kHz and pulse shaping thus helps to minimize the dispersion effects in the SHPB.

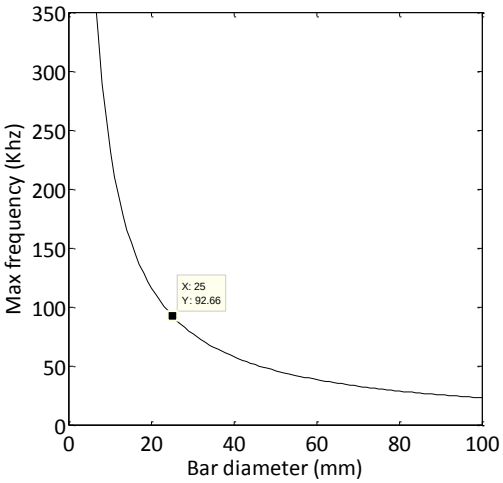

Figure 5.24 Maximum frequency present in the incident wave before dispersion correction is required. ν = 0.3, C_0= 5000m/s.

5.6 Summary

The compressional Split Hopkinson Pressure Bar to test linear elastic materials, were described in detail. The concept of pulse shaping was presented and particularly the method of utilizing cushion materials as copper. This method was found to be limited by friction, which created ripples in the shaped wave. Calibration of the SHPB test rig itself was also described. A new method to accurately calibrate the wave velocity in the bars was described which minimised the influence from the experimenter and could calibrate the wave velocity to a higher degree of accuracy than existing methods. It was emphasized that for a precise time-synchronization great attention has to be paid to an accurate calibration of the SHPB test rig. Lastly, it was shown that as long pulse shapers are used, dispersion is minimised, which simplifies the post processing of the recorded data.

6 A generalized wave mechanic model of the Split Hopkinson Pressure Bar

6.1 Introduction

The original Kolsky formulas and the alternative derivations for calculating the stress-strain response all assume equilibrium over the specimen [22][8]. Alternatively, separate stress measures from the incident and Transmitter bar can be used as presented for the modern SHPB in chapter 5. However, in each case, the conversion of the data into a stress-strain curve implicitly assumes a homogenous deformation state of the specimen, and an assessment of when the specimen is in equilibrium is required. A generalized model is developed in this chapter to perform this analysis for linear elastic materials.

Ravichandran et al. [22] reported early in 1994 a model based for a linear elastic specimen tested in a classic SHPB. They calculated how many times the elastic wave had to traverse the specimen before the specimen had reached a state of equilibrium. Equilibrium was defined as stress difference between the end to be less than 5% of the mean stress in the specimen and calculated as

$$R_{EQ} = \left| \frac{\sigma_a - \sigma_b}{\frac{\sigma_a + \sigma_b}{2}} \right| \tag{6.1}$$

Then the maximum strain rate is calculated from the number of wave transits to equilibrium and an assumption of constant strain rate. Parry et al. [93] presented a wave mechanics model for the classic SHPB, and the model described how the stress developed at the specimen/bar interfaces. They defined an equilibrium criterion as

$$EQ = \frac{\sigma_T}{\sigma_I + \sigma_R} \tag{6.2}$$

σ_I σ_R and σ_T are the incident, reflected and transmitted waves respectively and the bars are assumed to be equal in terms of the mechanical impedance. When the criterion reached unity, the specimen was in stress equilibrium. They found that stress equilibrium was reached within 3-5 wave transits dependent on the mechanical impedance of the tested material.

Frew et al. [20, 21] presented two models for calculating the evaluation of strain and stress in linear elastic material. They first used the original Kolsky formulas with assumption of stress equilibrium and equal bars to derive a closed form differential solution for the evolution of strain rate and strain through a test with linear rising pulse as loading. Equation (6.3) gives the solution for strain rate calculations and equation (6.4) gives the solution for calculating the strain.

$$\dot{\varepsilon}(t) = \frac{A_B M}{A_s E_s}\left[1 - e^{\frac{-2t}{rt_o}}\right] \tag{6.3}$$

$$\varepsilon(t) = \frac{A_B M}{A_s E_s}\left\{t - \frac{rt_0}{2}\left[1 - e^{\frac{-2t}{rt_o}}\right]\right\} \tag{6.4}$$

Equations (6.3) and (6.4) were later used by Pan et al. [70] and Foster et al. [94] to derive closed

form solutions for the maximum strain rate maintaining the inherent assumption of stress equilibrium. Table 6.1 compares the maximum strain rate measures and their assumptions.

Table 6.1 Maximum strain rate criteria for linear elastic brittle specimens and equal bars

Reference	Limit strain rate criteria	Assumption
[22]	$\dot{\varepsilon}_{Lim} = \frac{\varepsilon_f}{nt_0}$	Constant strain rate
[70]	$\dot{\varepsilon}_{Lim} = \frac{\varepsilon_f}{\frac{\tau}{1-\xi} - \frac{rt_0}{2}}$	Stress equilibrium, linear rising pulse
[94]	$\dot{\varepsilon}_{Lim} = \frac{\xi - 1}{1 + \ln(\xi) - \xi} \frac{2\varepsilon_f}{rt_0}$	Stress equilibrium, linear rising pulse

Parameter	Description
n	Number of wave transits in the specimens
ε_f	Failure strain
σ_f	Failure stress
ξ	Accepted deviation from equilibrium. Typically 0.05.
τ	Time to constant strain rate
$t_0 = \frac{L_s}{C_s}$	Propagation time through the specimen for an elastic wave.
$r = \frac{\rho_B C_B A_B}{\rho_0 C_0 A_0}$	Relative impedance between bar and specimen

Ravichandran et al. [22] found that a linear rising loading pulse requires at least four transits of the elastic wave through the specimen to occur before the stress difference was below 5% of the mean stress. This was calculated for a mechanical impedance ratio between the bar and specimen r = 1/8. For higher ratios more transits were required. The second set of equations Frew et al. [20, 21] developed is based on 1D wave mechanics and summed up all the wave reflections at the ends of the specimen as the wave propagated back and forth inside the specimen. The method used by Frew et al. [21] is in principle equivalent to the wave mechanics method used by Parry et al. [93], but Parry et al. arranged their formulas so stresses were summed up in the bars and not in the specimen. Yang et al. [19] used the same method as Frew et al. to derive equations for the stress equilibrium as defined in equation (6.1). Both step pulses and linear rising pulses were considered and Yang et al. found that at least six wave-transits were required for a linear rising pulse to get the stress difference below 5% of the mean stress in the specimen. Then there is not agreement in literature about the time to stress equilibrium. Table 6.1 shows the same for the criteria for constant strain rate. Further, all solutions in Table 6.1 also assume either stress equilibrium or constant strain rate. Foster et al. [94] used the strain rate equation from Frew et al. and found that stress equilibrium always occurs before constant strain rate, but the conclusion is limited by a assumption of uniform deformation in the specimen. Equilibrium solutions have also been found by modelling the specimen as a dynamic spring dashpot system as presented by Song et al. [17], but without agreeing with the other solutions.

The strain can be hard to measure when soft materials are tested. A high impedance mismatch between the specimen and Transmitter bar creates very low amplitude strains in the Transmitter bar, which are difficult to accurately measure. By suitable impedance matching, the signal can be amplified. For soft material testing, the impedance of the bar(s) must be lowered by changing the material and/or cross sectional area to match the soft materials to test. Chen et al. [95] changed the bar material from steel to aluminium and further used a hollow aluminium bar as the Transmitter bar for testing rubber, but the usage of uneven bars alters the Kolsky formulas and complicates the data reduction. Designing a SHPB requires the experimenter to decide the specimen cross sectional area and specimen length from requirements of high enough (constant) strain rate and homogenous deformation state (stress equilibrium) at failure. This is done from the models of

stress equilibrium and constant strain rate. However, the presented criteria for stress equilibrium and constant strain rate are no longer valid as the total impedance of the incident and Transmitter bars are not equal. The experimenter also has to select an Incident wave to apply to the specimen that satisfies the requirement of the test. The Incident wave must be shaped to promote stress equilibrium and constant strain rate.
In this chapter, a model is developed that describes the balancing of specimen cross sectional area and gage length with bar impedance and the form and size of the incident wave. The model is formulated and generalized such that restrictions of equal bars are removed. For reference, the model is named the GW model.

6.2 1D generalised wave mechanic model

The wave mechanics principle presented by Parry et al. [93] and Frew et al. [21] is used here to develop the GW model. Figure 6.1 defines a number of constants along with interface (a), between the Incident bar and the specimen, and interface (b), between the specimen and the Transmitter bar. 'A' is the cross sectional area, E the elastic modulus and ρ the density.

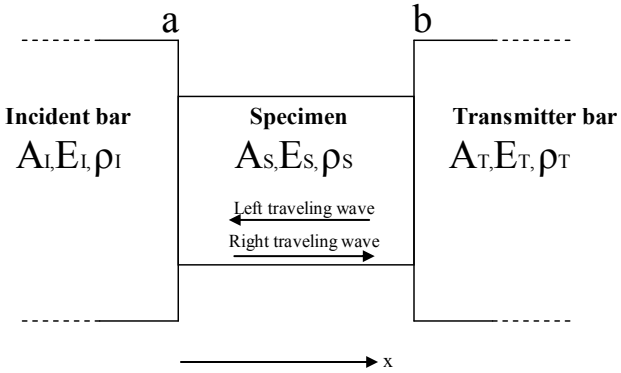

Figure 6.1 Schematic overview of the specimen and bar interfaces. The interface between the Incident bar and the specimen is denoted (a), while the interface between the specimen and the Transmitter bar is denoted (b). A is the cross sectional area. E is the elastic modulus, and ρ is the density. x defines the positive propagation direction of waves in the specimen.

The process starts with the incident wave propagating in the Incident bar towards the specimen. When the wave reaches the specimen, the wave is partly reflected and transmitted at interface (a). The transmitted part travels through the specimen, reaches interface (b) where it reflect, and transmits again. The reflected part from interface (b) propagates back toward interface (a) where it reflects and transmits again. The following assumptions apply to the wave motion:

- 1D dispersion free wave motion.
- The specimen behaves linear elastic up to fracture (brittle specimen).
- Single loading wave from the Incident bar
- Specimen remains in perfect contact with the bars during the entire loading duration (force equilibrium over the individual interfaces.)
- Bar ends remains perfectly flat during the entire loading duration.
- The bars have higher mechanical impedance than the specimen.

Equation (6.5) describes the 1D dispersion free wave motion [16].

$$\frac{\partial^2 u}{\partial t^2} = C_0^2 \frac{\partial^2 u}{\partial x^2} \tag{6.5}$$

C_0 is the elastic wave speed calculated as

$$C_0 = \sqrt{\frac{E}{\rho}} \tag{6.6}$$

D'Alembert solution applies to equation (6.6) and two quantities are of particular interest, the stress σ(x,t) and velocity V(x,t) at position x. Equation (6.7) give D'Alembert's solution to equation (6.5) for these quantities in the specimen in terms of stress waves travelling in the positive and negative x direction.

$$\begin{aligned} V(x,t) &= \frac{C_s}{E_s}(-\sigma_x(x - C_0 t) + \sigma_{-x}(x + C_0 t)) \\ \sigma(x,t) &= E_s(\sigma_x(x - C_0 t) + \sigma_{-x}(x + C_0 t)) \end{aligned} \tag{6.7}$$

The total stress σ(a,t) is calculated by summing all the incident and reflected waves at interface (a) and equivalent for σ(b,t) at interface (b). Three coefficients are defined to describe the transmission and reflection of the wave:

- B Transmission coefficient between the Incident bar and the Specimen
- B1 Reflection coefficient between the specimen and the Incident bar
- B2 Reflection coefficient between the specimen and the Transmitter bar

The specimen remains in perfect contact with the bars at all times so stress equilibrium over the interface applies and no gaps are formed or superposition of material occurs. The coefficients are calculated with classic wave mechanics as [3]

$$\frac{\sigma_s}{\sigma_I} = B = \frac{2A_I\rho_s C_s}{A_I\rho_I C_I + A_s\rho_s C_s} \tag{6.8}$$

$$\frac{\sigma_{s\_reflected}}{\sigma_s} = B1 = \frac{A_I\rho_I C_I - A_s\rho_s C_s}{A_s\rho_s C_s + A_I\rho_I C_I} \tag{6.9}$$

$$\frac{\sigma_{s\_reflected}}{\sigma_s} = B2 = \frac{A_T\rho_T C_T - A_s\rho_s C_s}{A_s\rho_s C_s + A_T\rho_T C_T} \tag{6.10}$$

The specimen has length Ls and the time it for an elastic wave to propagate from the Incident bar/specimen interface (a) to the specimen/Transmitter bar (b) is calculated by

$$t_0 = \frac{L_s}{C_s} \tag{6.11}$$

Each reflection at an interface is numbered by n = 0,1,2….k where k is the k'th reflection. The Incident wave is defined as $\sigma_I(t)$ with any arbitrary form. Figure 6.2 show a diagram over the reflection process with time on the y-axis and position on the x-axis.

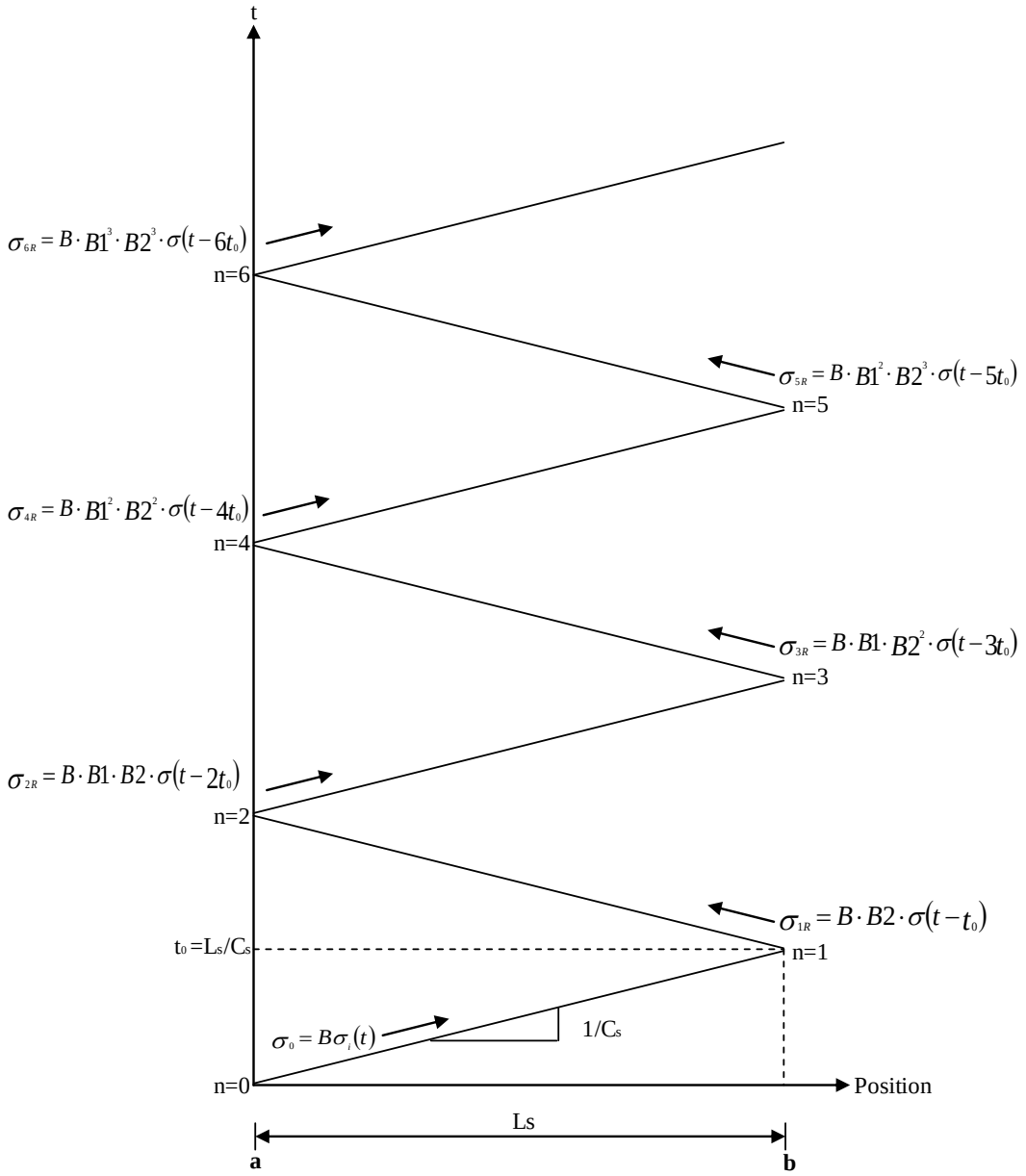

Figure 6.2 Diagram for wave motion the specimen. σ_{nR} is the reflected part of the wave at each reflection between the wave and the interfaces.

The loading process starts at t=0 and n=0 where the incoming incident pulse $\sigma_I(t)$is reflected and transmitted at the Incident bar/specimen interface (a). The transmitted part propagates through the specimen heading towards interface (b). Until the reflected part from interface (b) comes back to interface (a) the stress at interface (a) will be

n = 0 $$\sigma_a(t) = B\sigma_i(t), \qquad 0 \le t < 2t_0 \tag{6.12}$$

As the wave has to travel to and from interface (b), interface (a) will first see a change in its loading condition after $2t_0$. As the wave reaches interface (b) at n=1 the wave reflects and transmits and the stress is the sum of the incoming wave and the reflected part according to equation (6.7). $\sigma_i(t)$ is delayed t_0 when it hits interface (b) the first time such that it becomes

$\sigma_i(t - t_0)$. The incoming wave at interface (b) at t = t_0 is then

$$\sigma_{b\ incoming}(t) = B\sigma_i(t - t_0) \tag{6.13}$$

The wave is reflected and the reflected part (named σ_{1R} in Figure 6.2) is

$$\sigma_{1R}(t) = B \cdot B_2 \cdot \sigma_i(t - t_0) \tag{6.14}$$

The sum of the incoming and reflected wave gives the total stress at interface (b) as

$$\begin{aligned} &\sigma_b(t) = B\sigma_i(t - t_0) + B \cdot B_2 \cdot \sigma_i(t - t_0) \Leftrightarrow \\ \text{n = 1} \qquad &\sigma_b(t) = B \cdot (1 + B_2) \cdot \sigma_i(t - t_0) \\ &t_0 \le t < 3t_0 \end{aligned} \tag{6.15}$$

This sum is maintained as a function of $\sigma_i(t)$ until the wave reaches back from interface (a) again. σ_{1R} propagates back towards interface (a) where it arrives at time t = $2t_0$. The wave reflects and transmits and with the reflection coefficient B_1 of interface (a) the reflected part becomes

$$\sigma_{2R}(t) = B \cdot B_1 \cdot B_2 \cdot \sigma_i(t - 2t_0) \tag{6.16}$$

The total stress at interface (a) is now the sum of the incoming wave σ_{1R} from interface (b) plus the reflection σ_{2R} and further also the transmitted part of the incident wave from the Incident bar which is still is present at the interface at time t. σ_{2R} is also the Incident wave, just transmitted, reflected twice and delayed $2t_0$. The total stress is calculated as

$$\begin{aligned} &\sigma_a(t) = B\sigma_i(t) + B \cdot B_2 \cdot \sigma_i(t - 2t_0) + B \cdot B_1 \cdot B_2 \cdot \sigma_i(t - 2t_0) \Leftrightarrow \\ \text{n = 2} \qquad &\sigma_a(t) = B \cdot \sigma_i(t) + B \cdot (B_2 + B_1B_2) \cdot \sigma_i(t - 2t_0) \\ &2t_0 \le t < 4t_0 \end{aligned} \tag{6.17}$$

σ_{2R} propagates towards interface (b) where it is the incoming wave that reflects and transmits. The reflected part becomes

$$\sigma_{3R}(t) = B \cdot B_1 \cdot {B_2}^2 \cdot \sigma_i(t - 3t_0) \tag{6.18}$$

The total stress at interface (b) is the sum of all incoming and reflected parts with their respective time delays

$$\begin{aligned} &\sigma_b(t) = B\sigma_i(t - t_0) + B \cdot B_2 \cdot \sigma_i(t - t_0) + B \cdot B_1 \cdot B_2 \cdot \sigma_i(t - 3t_0) + B \\ &\qquad \cdot B_1 \cdot {B_2}^2 \cdot \sigma_i(t - 3t_0) \Leftrightarrow \\ \text{n = 3} \qquad &\sigma_b(t) = B \cdot (1 + B_2) \cdot \sigma(t - t_0) + B \cdot (B_1B_2 + B_1B_2^2) \cdot \sigma(t - 3t_0) \\ &3t_0 \le t < 5t_0 \end{aligned} \tag{6.19}$$

σ_{3R} becomes the incoming wave at interface (a) and the reflected part of σ_{3R} at interface (a) is

$$\sigma_{4R}(t) = B \cdot B_1^2 \cdot {B_2}^2 \cdot \sigma_i(t - 4t_0) \tag{6.20}$$

The total sum of stress contributions at interface (a) now becomes

$$\begin{aligned} &\sigma_a(t) = B\sigma_i(t) + B \cdot B_2 \cdot \sigma_i(t - 2t_0) + B \cdot B_1 \cdot B_2 \cdot \sigma_i(t - 2t_0) + B \cdot B_1 \\ &\qquad \cdot {B_2}^2 \cdot \sigma_i(t - 4t_0) + B \cdot B_1^2 \cdot {B_2}^2 \cdot \sigma_i(t - 4t_0) \\ \text{n = 4} \qquad &\sigma_a(t) = B\sigma_i(t) + B \cdot (B_2 + B_1B_2) \cdot \sigma_i(t - 2t_0) + B \cdot (B_1B_2^2 + B_1^2B_2^2) \\ &\qquad \cdot \sigma_i(t - 4t_0) \\ &4t_0 \le t < 6t_0 \end{aligned} \tag{6.21}$$

Again the reflected part, now σ_{4R}, of the incoming wave, propagates towards interface (b). At n=5 the added incoming and reflected part is

n = 5

$$\sigma_b(t) = \ldots + B \cdot (B_2^2 B_2^2 + B_2^2 B_2^3) \cdot \sigma_i(t - 5t_0) \quad 5t_0 \le t < 7t_0 \tag{6.22}$$

This process continues as long the Incident wave is present and, at a certain time, the wave is reflected so many times that there is no practical addition to the stress state in the interfaces. For calculations beyond 5 transits, equations (6.12) to (6.22) is rewritten into a sum function of the wave for interface (a)

$$\sigma_s(a,t) = B \sum_{n=0}^{\left\lfloor \frac{t}{t_0} \right\rfloor} F(n, B_1, B_2)\sigma_I(t - nt_0) \tag{6.23}$$

$\left\lfloor \frac{t}{t_0} \right\rfloor$ is the largest possible integer (n) of the ratio $\frac{t}{t_0}$ and F(n) is a coefficient vector. From equations (6.12) and (6.22), F(n) is written as

$$F(n, B_1, B_2) = \left[B_1^{x1(n)} B_2^{x2(n)} + B_1^{x2(n)} B_2^{x3(n)}\right], n > 0 \tag{6.24}$$

Equations (6.12) - (6.22) show the exponents x1, x2 and x3 develops as function of n as given in Table 6.2.

Table 6.2 Sequences for exponents in equation (6.24) for n=0 to 10

n	x1	x2	x3
0	0	0	0
1	0	0	1
2	0	1	1
3	1	1	2
4	1	2	2
5	2	2	3
6	2	3	3
7	3	3	4
8	3	4	4
9	4	4	5
10	4	5	5

x1 to x3 are expressed as a function of n as

$$\begin{aligned} x1(n) &= \frac{n-1}{2} + \frac{1^n + (-1)^n}{4} \\ x2(n) &= \frac{n}{2} + \frac{1^n + (-1)^n}{4} \\ x3(n) &= \frac{n+1}{2} + \frac{1^n + (-1)^n}{4} \end{aligned} \tag{6.25}$$

Equation (6.24) is only valid for n>0. In the case where n=0, F(n) equals 2, but F(n) should be 1 according to Equation (6.12) as only the transmitted wave is present at t = 0-2t_0. So explicitly F(0) = 0.

Equations (6.12) and (6.22) also show interface (a) only gets an extra added term for even numbers of n while interface (b) gets an extra added term for odd numbers of n. Then the interface stresses are written as

$$\sigma_s(a,t) = B \sum_{n=0}^{\left\lfloor \frac{t}{t_0} \right\rfloor} F(n, B_1, B_2)\sigma_I(t - nt_0), \qquad n = 0,2,4 \ldots . k \tag{6.26}$$

$$\sigma_s(b,t) = B\sum_{n=0}^{\left\lfloor \frac{t}{t_0} \right\rfloor} F(n,B_1,B_2)\sigma_I(t-nt_0)\,, \qquad n = 1,3,5\ldots.k \tag{6.27}$$

The structure of F(n) is now exploited to derive equations for the velocity at the interfaces. First, it is necessary to recap from equation (6.7) that for the velocity, waves traveling in the positive x direction had negative sign in the sum while waves traveling in the negative x direction had a positive sign in the sum. For the stress computation, both waves had a positive sign. Examination of F(n) shows it is calculated as the product of B1 and B2 with one set of exponents, and this set is added with the other product of B1 and B2, which has another set of exponents. Careful examination of equations (6.12) to (6.22) reveals that the first product describes the incoming waves to the interfaces at their respective wave transit number (n). The second product describes the reflected wave at the interfaces and the reflected waves are always altered by an extra reflection compared to their incoming counterpart. This explains why the second product in F(n) is "ahead" in the exponents compared to the first product of F(n). Figure 6.3 shows that interface (a) has its incoming waves traveling in the negative x direction while the reflected waves travel in the positive x direction. For interface (b) it is the opposite and thus the interfaces require a different set of signs to calculate the velocity according to equation (6.3).

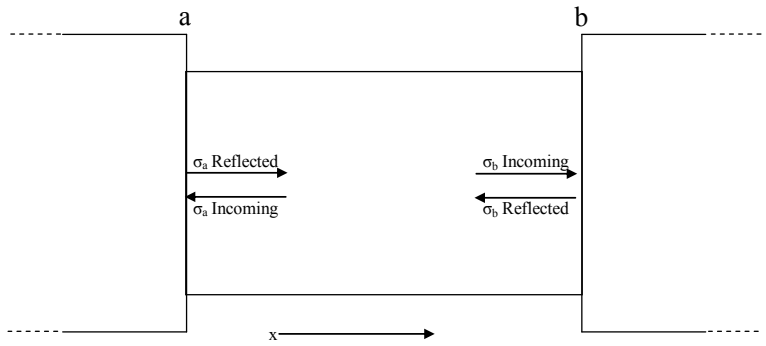

Figure 6.3 Wave directions.

Thus two coefficient functions Fva(n) and Fvb(n) are defined and with negative signs for the reflected waves, Fva(n) becomes

$$F_{va}(n,B_1,B_2) = \left[B_1^{x1(n)}B_2^{x2(n)} - B_1^{x2(n)}B_2^{x3(n)}\right], \qquad n = 2,4,6\ldots k \tag{6.28}$$

With negative sign for incoming waves, Fvb(n) becomes

$$F_{vb}(n,B_1,B_2) = \left[-B_1^{x1(n)}B_2^{x2(n)} + B_1^{x2(n)}B_2^{x3(n)}\right], \qquad n = 1,3,5\ldots k \tag{6.29}$$

As with F(n), Fva(n) and Fvb(n) are only defined for n>0. Fva(0) is -1 as the transmitted wave passes through the interface in the positive x direction. Fvb(0) is not used, but is set to 1. The velocity is now calculated in a similar way as the stresses in equation (6.26) and (6.27) using D'Alemberts solution.

$$V_s(a,t) = \frac{C_s}{E_s}B\sum_{n=0}^{\left\lfloor \frac{t}{t_0} \right\rfloor} F_{va}(n,B_1,B_2)\sigma_I(t-nt_0)\,, \qquad n = 0,2,4\ldots.k \tag{6.30}$$

$$V_s(b,t) = \frac{C_s}{E_s} B \sum_{n=0}^{\left\lfloor \frac{t}{t_0} \right\rfloor} F_{vb}(n, B_1, B_2)\sigma_I(t - nt_0)\,, \qquad n = 1,3,5 \ldots . k \tag{6.31}$$

Equations (6.26), (6.27), (6.30) and (6.31) form a set of equations that describe the variation of stress and velocity at the specimen ends for any arbitrary chosen incident wave and impedance mismatch between the bars and specimen. Thus, the equilibrium process can be estimated for any combination of bars, specimen and Incident wave.

When the specimen stress is known, the reflected wave in the Incident bar can be calculated, as well as the transmitted wave in the Transmitter bar. Applying the assumption of force equilibrium at interface (a) yields

$$\begin{aligned} &A_I(\sigma_I(t) + \sigma_R(t)) = A_s\sigma_s(a,t) \;\Leftrightarrow \\ &\sigma_R(t) = \frac{A_s}{A_I}\sigma_s(a,t) - \sigma_I(t) \end{aligned} \tag{6.32}$$

With force equilibrium over interface (b) the transmitted wave is calculated as

$$\begin{aligned} &A_S\sigma_s(b,t) = A_t\sigma_t(t) \\ &\sigma_T(t) = \frac{A_S}{A_T}\sigma_s(b,t) \end{aligned} \tag{6.33}$$

The Incident, Reflected and Transmitted waves are known for the Incident and Transmitter bar, and the SHPB formulas can be applied to calculate the linear stress strain curve. More importantly, the required stress wave amplitude in the bars can be estimated and compared to the yield strength of the bars as well as measurement system capacity.

6.3 Validation of the model

The GW model is compared to the wave mechanic model presented by Frew et al. [20, 21] (Equation (9) and (10)). Adapted from Yang et al. [19] three Incident waves is used to compare the models: a step pulse, a step pulse with finite rise time, and a linear rising pulse. The waves are shown in Figure 6.4A. The model derived by Frew et al. is only valid for equal bars so B1 = B2 is used for the GW model. Both models are implemented in MatLab to compare the stresses at interface (a) and (b). The average stress difference between the models is calculated as

$$\overline{\Delta\sigma} = \frac{(\sigma(a,t) - \sigma_{Frew}(a,t)) + (\sigma(b,t) - \sigma_{Frew}(b,t))}{2} \tag{6.34}$$

Figure 6.4B shows equation (6.34) plotted as a function of wave transit in the specimen for the three loading pulses shown in Figure 6.4A. The average stress difference is measured in µPa, which in practice mean the models behave equally.

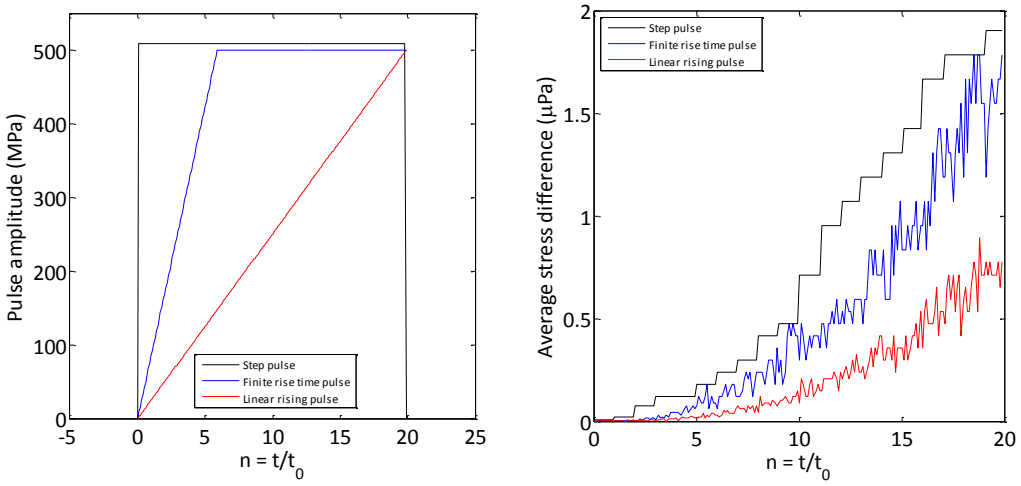

A) Waves pulses used for comparison of the models *B) Interface stress σ_a and σ_b*

Figure 6.4 Comparison of the wave mechanics model (Equations 9 and 10 in [21]*) presented by Frew et al. and the GW model derived in this work (Equations (6.26) and (6.27))*

Yang et al. [19] presented formulas to calculate the equilibrium state as a function of the number of wave transits n for different Incident waves. The formulas are only valid for equal bars so B1 = B2 in this case also. The equilibrium state is calculated as in equation (6.1). Figure 6.5 shows a comparison of the GW model and the formulas derived by Yang et al.

Step pulse

$$R(n) = \frac{2\beta(1-\beta)^{n-1}}{(1+\beta)^n - (1-\beta)^n}$$

Finite rise time pulse

$$R(n) = \frac{2\beta(1-\beta)^{n-2}}{(1+\beta)^n - (1-\beta)^{n-2}}, \quad k > 2$$

Linear rising pulse

$$R(n) = \frac{2\beta^2\left[1 - \left(\frac{-(1-\beta)}{1+\beta}\right)^n\right]}{2n\beta - 1 + \left(\frac{1-\beta}{1+\beta}\right)^n}, \quad k > 2$$

$$\beta = \frac{A_l Z_l}{A_s Z_s}$$

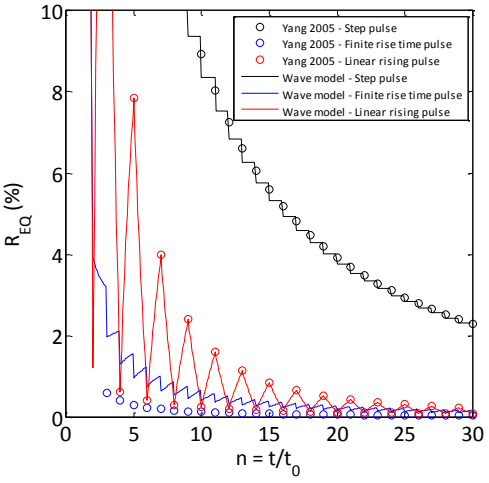

A) Formulas for calculating equilibrium measure as function of number of wave transits (n). *B) R(n) for β=0.0122 compared with the GW model*

Figure 6.5 Comparison between the GW model and the formulas derived by Yang et al. [19].

For the linear rising pulses, the models yields the same result while for step pulse the model from Yang et al. predict a value between two time steps in the GW model. For the step pulse with a finite rise time, the model by Yang et al. predict a faster equilibrium process compared to the GW model. The model by Yang et al. is only defined for n > 2 and the finite rise time in the pulse is set to 2n for their derivation. A pulse with finite rise of 2n has been used for both the models so the

difference is in the formulation of the models.

6.4 Effect of the Incident wave

The GW model can be used with any arbitrary loading pulse to predict the evolution of stress equilibrium and strain rate with any set of combination of bars and specimen. To examine the effect of the general shape of the Incident wave on the evolution in stress equilibrium and strain rate, the three loading pulses presented in Figure 6.4A are used along with an exponential growing curve $F(x) = Ct^x$ with x≠1. The loading pulses are shown in Figure 6.6 and they represent the set of loading pulse shapes, which can be generated in a SHPB test rig.

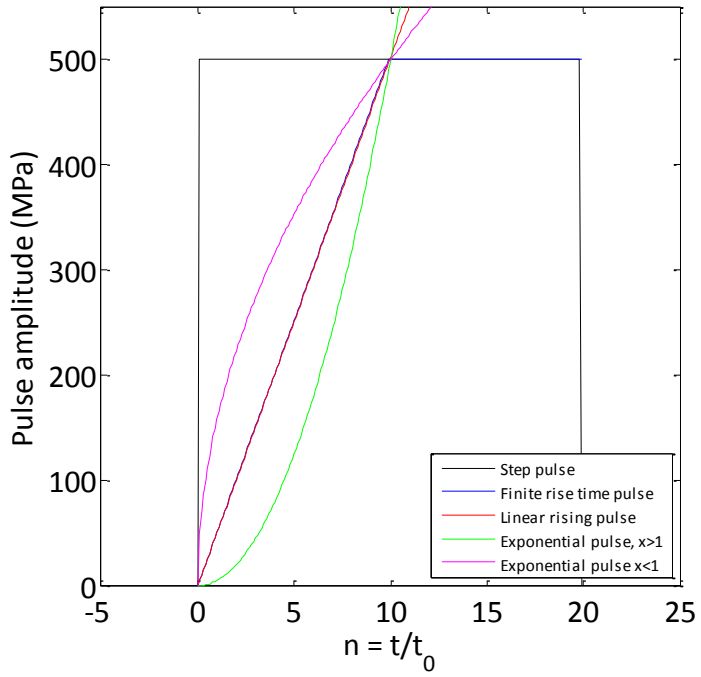

Figure 6.6 Different loading pulses

The influence of the shape of the loading pulse on the evolution of stress equilibrium and strain rate is examined with B1 = B2 = 0.667 in Figure 6.7. Dynamic equilibrium and constant strain rate are only reached with the linear rising pulse. In Figure 6.8 the case with rigid boundaries (B1 = B2 = 1) is examined. Here the step pulse with a finite rise time gives the best result, and the equilibrium evolution follows that of the linear rising pulse until the pulse reaches constant amplitude. The finite rise ensures faster stress equilibrium and reaches the same strain rate as the pure step pulse. None of the other loading pulses are able to create a state of constant strain rate with rigid boundaries. Thus if the test specimen is situated between elastic boundaries as in the SHPB test rig, and a state of stress equilibrium and constant strain are sought, then the linear rising pulse is the best option. Figure 6.9 shows the same holds true if the bars are made with different impedances. If the boundaries are close to rigid, a step pulse with a finite rise time is the best option.

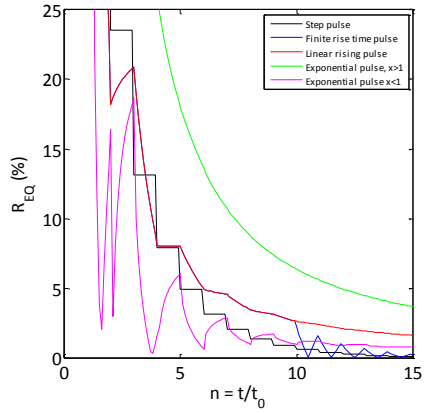

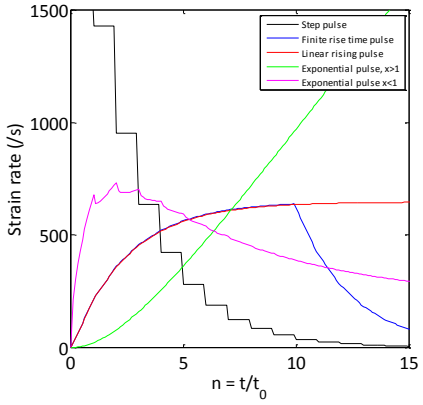

A) Stress equilibrium *B) Strain rate*

*Figure 6.7 Simulation of stress equilibrium and strain rate evolution for **B1 = B2 = 0.667***

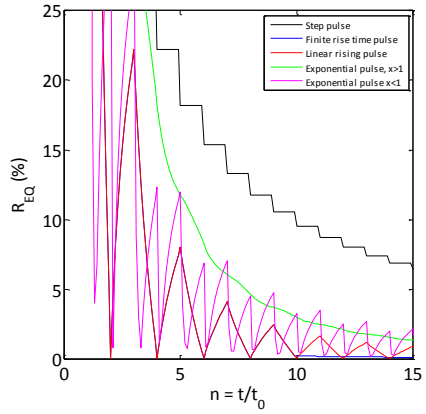

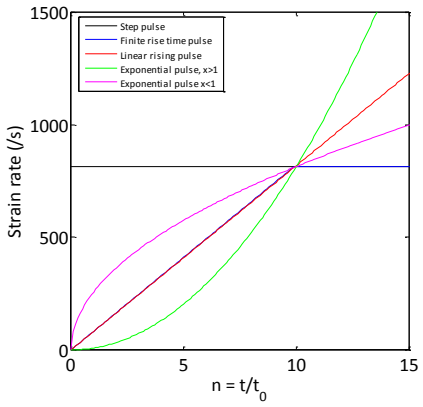

A) Stress equilibrium *B) Strain rate*

*Figure 6.8 Simulation of stress equilibrium and strain rate evolution for **B1 = B2 = 1**. (Rigid boundaries)*

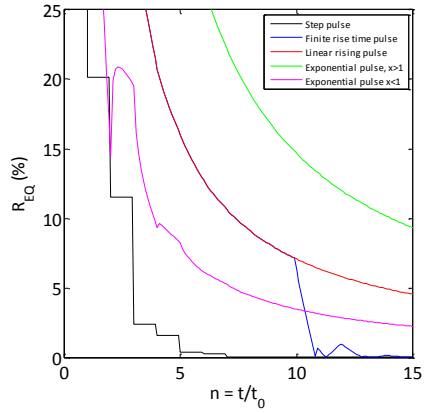

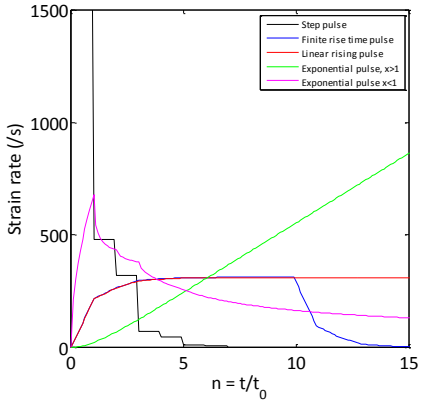

A) Stress equilibrium *B) Strain rate*

*Figure 6.9 Simulation of stress equilibrium and strain rate evolution for **B1 = 0.667, B2 = 0.22.***

The linear rising pulse as the best option for linear elastic brittle specimens was mentioned in several papers [17, 18, 20, 69, 71, 74, 83, 96, 97], but only for ensuring faster stress equilibrium.

6.5 Stress equilibrium and constant strain rate

The reflection function F(n) is exploited to give information about what specimen size, type of bars, and constant loading rate should be used to ensure that both stress equilibrium, and constant strain rate occur before the specimen fails. Equations (6.26) and (6.27) give the stress at the respective interfaces of the specimen for an arbitrary stress pulse σ_I as a function of time. However, based on the finding in section 6.4 the loading pulse σ_I is restricted to a linear rising stress pulse, with slope M, given as $\sigma_I(t) = M \cdot t$. If the stress is evaluated only at the k'th reflection such that $t = kt_0$ then equation (6.26) is written as

$$\sigma(a,k) = B \cdot M \cdot t_0 \cdot \sum_{n=0}^{k} F(n, B_1, B_2)(k-n)\,, \qquad n = 0{,}2{,}4 \ldots k \tag{6.35}$$

Equation (6.27) becomes

$$\sigma(b,k) = B \cdot M \cdot t_0 \cdot \sum_{n=0}^{k} F(n, B_1, B_2)(k-n)\,, \qquad n = 1{,}3{,}5 \ldots k \tag{6.36}$$

In the SHPB community it is widely accepted that the specimen is in dynamic equilibrium when R_{EQ} (equation (6.1)) is less than 5% [17-19, 22, 69]. So inserting equations (6.35) and (6.36) into (6.1) yields

$$\begin{aligned} &R_{eq}(k) \\ &= 2 \cdot \left| \frac{B \cdot M \cdot t_0 \cdot \sum_{n=0}^{k} F(n,B_1,B_2)(k-n) - B \cdot M \cdot t_0 \cdot \sum_{n=0}^{k} F(n,B_1,B_2)(k-n)}{B \cdot M \cdot t_0 \cdot \sum_{n=0}^{k} F(n,B_1,B_2)(k-n) + B \cdot M \cdot t_0 \cdot \sum_{n=0}^{k} F(n,B_1,B_2)(k-n)} \right| \Leftrightarrow \\ &R_{eq}(k) = 2 \cdot \left| \frac{\sum_{n=0,2\ldots}^{k} F(n,B_1,B_2)(k-n) - \sum_{n=1,3\ldots}^{k} F(n,B_1,B_2)(k-n)}{\sum_{n=0,2\ldots}^{k} F(n,B_1,B_2)(k-n) + \sum_{n=1,3\ldots}^{k} F(n,B_1,B_2)(k-n)} \right| \end{aligned} \tag{6.37}$$

Thus, with the assumption of a linear rising loading pulse, the stress equilibrium is independent of the stress rate, the specimen length, and the wave velocity. This is consistent with the findings for the case of equal bars [17, 94].

The strain rate in the specimen is linked to $F_{va}(n)$ and $F_{vb}(n)$. Equations (6.31) and (6.32) are rewritten in the same way as equation (6.35) and (6.36) to obtain the velocity in the specimen at the interfaces

$$V_s(a,k) = \frac{C_s}{E_s} \cdot B \cdot M \cdot t_0 \cdot \sum_{n=0}^{k} F_{va}(n)(k-n)\,, \qquad n = 0{,}1{,}2 \ldots k \tag{6.38}$$

$$V_s(b,k) = \frac{C_s}{E_s} \cdot B \cdot M \cdot t_0 \cdot \sum_{n=0}^{k} F_{vb}(n)(k-n)\,, \qquad n = 0{,}1{,}2 \ldots k \tag{6.39}$$

The average strain rate over a specimen of length L_s settled between two bars is calculated as [3]:

$$\frac{d\varepsilon}{dt} = \dot{\varepsilon}(t) = \frac{V_s(a,t) - V_s(b,t)}{L_s} \tag{6.40}$$

Inserting equations (6.38) and (6.39) into (6.40) yield

$$\dot{\varepsilon}(t) = \frac{1}{L_s} \cdot \frac{C_s}{E_s} \cdot B \cdot M \cdot t_0 \cdot \sum_{n=0}^{k} (k-n) \cdot \left(F_{va}(n, B1, B2) - F_{vb}(n, B1, B2)\right) \tag{6.41}$$

Utilizing that $t_0 = L_s/C_s$ the strain rate is calculated as

$$\dot{\varepsilon}(k) = \frac{1}{E_s} \cdot B \cdot M \cdot \sum_{n=0}^{k} (k-n) \cdot F_v(n, B1, B2) \tag{6.42}$$

Where $F_v(n)$ is calculated as the sum of Fva and Fvb remembering Fva is only defined for even numbers and Fvb is only defined for odd numbers. Then Fv becomes

$$F_v(n, B_1, B_2) = \left[B_1^{x1(n)} B_2^{x2(n)} - B_1^{x2(n)} B_2^{x3(n)}\right], \;\; n = 1,2,3 \ldots k \tag{6.43}$$

Equation (6.43 shows that the strain rate is proportional to the convolution sum of Fv and (k-n). The strain rate will reach a constant level when the convolution sum do not increase anymore with increasing values of k, which will happen when Fv(n) is small. The bars must have greater mechanical impedance than the specimen to ensure loading of the specimen, so B1 and B2 must be greater than 0. The maximum value of B1 and B2 is one[2], which is completely rigid bars. An analyses of F_v for n = 500 and all combinations of B1 and B2 between 0 and 1 gives a max value of $8x10^{-4}$ at B1 = B2 =1. Then, at n=500 all combinations of B1 and B2 would have reached constant strain rate, and n = 500 can be used as an estimate of the maximum strain rate. The relative deviation from constant strain rate is expressed as

$$R_{SR}(k, B1, B2) = \frac{\sum_{n=0}^{500}(500-n) \cdot F_v(n, B1, B2) - \sum_{n=0}^{k}(k-n) \cdot F_v(n, B1, B2)}{\sum_{n=0}^{500}(500-n) \cdot F_v(n, B1, B2)} \tag{6.44}$$

When R_{SR} is below 5%, a dynamic constant strain can be said to have occurred. Note that constant strain rate only occurs when $V_a(t) \neq V_b(t)$ and $V_a(t)$ and $V_b(t)$ are constant. Alternatively, if $V_a(t) \neq V_b(t)$ and $V_a(t)$ and $V_b(t)$ are undergoing the same acceleration, the velocity difference is constant, even though the velocity changes on both sides of the specimen. The number of reflections to constant strain rate is independent of t_0 and the maximum strain rate is then not a function of the specimen length. However, the specimen length controls how long it takes to reach the maximum strain rate. The well-known estimator of strain rate given in equation (6.45) is thus not useable with linear elastic materials loaded by linear rising pulse.

$$\dot{\varepsilon}_{eng} = \frac{V}{L_0} \tag{6.45}$$

It is interesting to examine whichever stress equilibrium or constant strain rate occurs first. Equations (6.37) and (6.44) are evaluated for all combinations of B1 and B2 to find n which satisfy both R_{EQ} and $R_{SR} < 0.05$. The result is plotted in Figure 6.10A as a contour plot. The blue dot represents a setup with B1 = B2 = 0.5. For this combination, stress equilibrium will happen between 8 and 10 transits of the wave through the specimen while constant strain rate is achieved after 4 to 6 transits. The diagonal of Figure 6.10A corresponds to equals bars and is plotted in Figure 6.10B. Whichever constant strain rate or stress equilibrium is reached first depends on the combination of impedance mismatches, also for equal bars. This is inconsistent with Foster et al. [94] who found that stress equilibrium would always happen first. However, this result was obtained from a homogenous approach and not the full wave mechanics approach as here.

[2] See Appendix B.

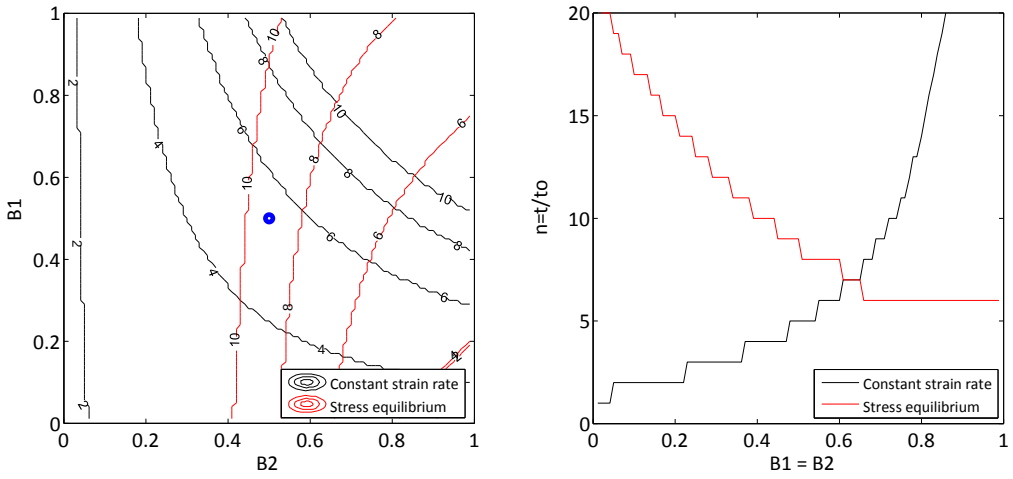

A) Contour plot of wave transits to obtain dynamic equilibrium and constant strain rate

B) Number of reflections to constant strain rate with equal bars

Figure 6.10 Number of reflections in the specimen to achieve stress equilibrium and constant strain rate

Figure 6.10 does not indicate if stress equilibrium or constant strain rate is fulfilled before specimen failure for a particular test. In addition, it does not indicate the achievable strain rate before failure. Figure 6.10 only indicates how many round trips the wave requires to equilibrate the condition. The final strain rate is determined from the applied stress rate, B1 and B2.

6.6 Test design

The GW model is well suited for designing a test in the Split Hopkinson Pressure Bar for FRP materials, if they are assumed linear elastic. In most cases, an SHPB is already available and maybe with Incident and Transmitter bars made from different materials. The challenge is to select the correct specimen size, together with the correct stress rate of the incident pulse to ensure conditions of stress equilibrium and constant strain rate before failure. If the elastic modulus and density are known for both the bars and the test specimen, the design process narrows to estimate the specimen cross sectional area A_s along with the length L_s. First for a given set of A and L_s, the number of wave transit to stress equilibrium (N_{EQ}) and constant strain rate (N_{SR}) should be calculated. Then the greater of these (n_{max}=max{N_{EQ},N_{SR}}) is used to solve equation (6.46) for the stress rate M.

$$\sigma_{s\_failure} = \sigma(a, n_{max}) = B \cdot M \cdot t_0 \cdot \sum_{n=0}^{n_{max}} F(n)(n_{max} - n) \qquad (6.46)$$

$\sigma(a,k)$ is used since the stress at interface (a) will always be larger than at interface (b). When M is calculated, the matching maximum strain rate is calculated from equation (6.42). Thus, the maximum strain rate, the maximum stress rate, and the time to fracture are known. Further analyses could include the required pulse length and maximum amplitude in the Incident bar. Finally, the required pulse can then be matched through the available pulse shaping technique. The design algorithm is summarised in table 6.3.

Table 6.3 SHPB specimen design algorithm

Step	Description
0	Select bars and set the design space for Ls and A. For example Ls can vary between 3 and 15mm. Also select criteria for constant strain rate and stress equilibrium
	Steps 1 to 8 are repeated for each combination of A and Ls
1	Calculate transmission and reflection coefficient B, B1 and B2
2	Calculate F and Fv
3	Create Fa
4	Find number (N_{SR}) of wave transits to constant strain rate
5	Find number (N_{EQ}) of wave transits to stress equilibrium
6	Select the highest number of N_{SR} and N_{EQ}
7	Calculate maximum stress rate
8	Calculate achievable constant strain rate using the result from step 7
9	Check of maximum stress in the Incident bar and Transmitter bar. Also check the required wave duration

As example the design algorithm with is used for a composite with an elastic modulus of 8.7 GPa in the loading direction and a density 2000kg/m^3. The SHPB is equipped with a 25mm diameter Incident bar made from steel with E = 191GPa and ρ = 7741kg/m^3. The Transmitter bar is 25mm in diameter, E = 73.4GPa and ρ = 2809kg/m^3. The specimen design is restricted such that the cross sectional area can vary in fractions between 0.2 and 0.8 of the bar cross sectional area. The gage length is constrained to lie in the interval 3-15mm.

Figure 6.11 gives maximum strain rate and stress rate as contour plots, calculated using the design algorithm in

Table 6.3. For example an area ratio of 0.25 and length of 10 mm will give an approximate maximum strain rate of 200 /s.

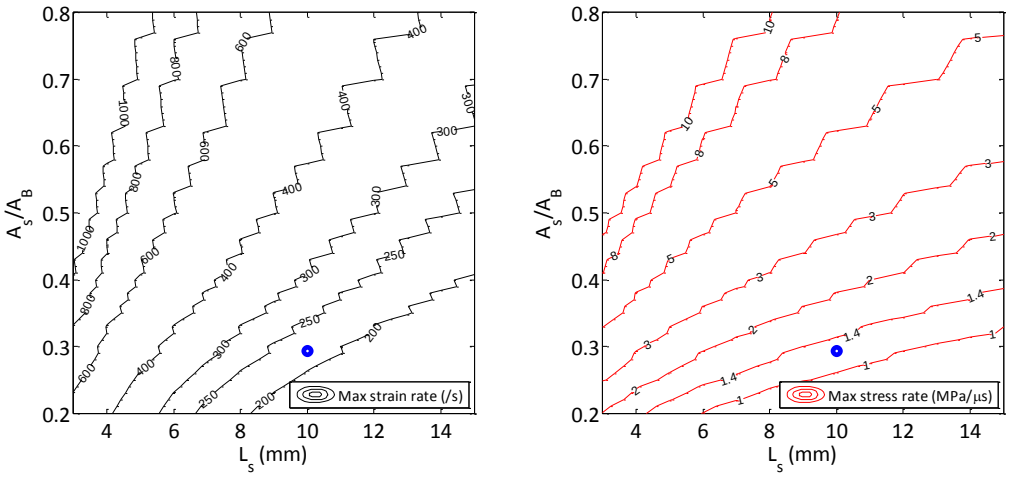

A) Maximum strain rate as a function of specimen cross section ratio A_s/A_B and specimen length L_s.

B) Maximum stress rate in the Incident bar as a function of specimen cross section ratio A_s/A_B and specimen length L_s.

Figure 6.11 Maximum strain rate and stress rate

The blue dot in Figure 6.11A represents a specimen with a square cross section with dimensions 12x12mm and a length of 10mm. This specimen was tested in the described SHPB and the strain – strain rate curves are shown in Figure 6.12A for different stress rates in the Incident wave. The corresponding incident waves are shown in Figure 6.12B. The test is described in details in chapter 8. A plateau is realised followed by a steady rise at low strain rate. The plateau is in agreement with Figure 6.11A, which predict that a steady strain rate of 150/s is possible. The limiting stress rate at the blue dot is 1.17 MPa/µs and the stress rate was 0.91 MPa/µs at low strain rate as shown in Table 6.4. The subsequent rise in strain rate from the plateau is believed to be due to the nonlinearity in the Incident wave, and failure progression in the specimen. The medium strain rate is around 250-300/s with a stress rate of around 1.42 MPa/µs. This is higher than the calculated limit and is indicated by slightly varying strain rate throughout the entire deformation history. For the high strain rate the stress rate is nearly 3 times higher than the calculated limit and this is seen as a highly varying strain rate throughout the deformation history.

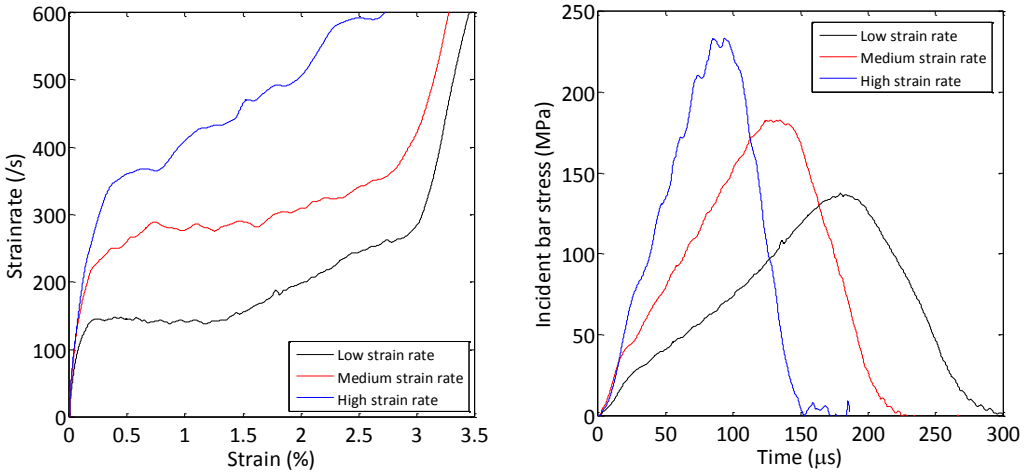

A) Strain rate vs. strain curves

B) Incident waves with different stress rates in the rising part

Figure 6.12 Incident waves and strain rate vs. strain curves for the design case

Table 6.4 Stress rates in Incident pulses in Figure 6.12

Strain rate level	Stress rate (MPa/µs)	Measurement interval (µs)
Low	0.91	100-150
Medium	1.42	50-100
High	3.16	50-75

6.7 Radial inertia - considerations

Radial inertia should also be considered when test specimens are deformed at high strain rates. The radial inertia due to the Poisson ratio will cause an added stress increment in the specimen, which causes an error in the stress measurement. Forrestal et al. [98] derived a closed form solution for the added inertia stress for an isotropic linear elastic material deforming at stress equilibrium. The addition of the stress in the loading direction is given by equation (6.47) [98] where "ν" is Poisson's ratio, "a" is the radius of the specimen, "ρ" the specimen density, and "r" is the position along the radial direction of the specimen. The added stress in the loading direction is proportional to the change of strain rate and the same is the case in the radial direction.

$$\sigma_x = \frac{\nu_s^2(3-2\nu_s)}{4(1-\nu_s)}\left[{a_s}^2 - \frac{2r^2}{(3-2\nu_s)}\right]\rho_s \frac{d^2\varepsilon_x^0}{dt^2} \qquad (6.47)$$

Thus if the specimen is deforming a constant strain rate the inertial stress increase will vanish. Further Forrestal and Chen et al. [18, 98] concluded that the for the strain rates which are generated in a SHPB rig the magnitude of the added stress is 1MPa or below. Thus, radial inertia can be ignored for high performance fibre reinforced specimens, and the effect is not included in the GW model.

6.8 Simulation tool

The formulation of equation (6.27) and (6.26) allows any arbitrary loading pulse to be analysed with the GW model. For example a simulated pulse-shaped loading pulse could be fed into the model, or an actual recorded loading pulse from a SHPB. No loading pulse is perfectly linear, so it is of interest to see the influence of the varying loading pulse on the simulated specimen response.

Figure 6.13 gives an overview of the simulation process with the GW model.

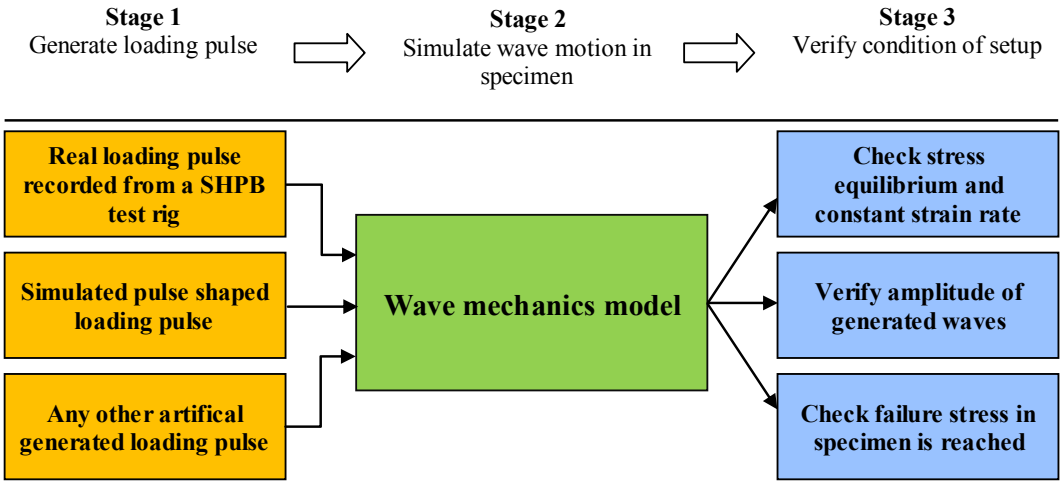

Figure 6.13 Schematic of the simulation model

The Incident, Reflected and Transmitted waves in the bars are calculated from equations (6.32) and (6.33) and can be used to post process the simulation with the different post processing equations as well as verifying stress equilibrium and constant strain rate. Figure 6.14 and Figure 6.15 show simulation and comparison for the two cases in Figure 6.12, "Low" and "high" strain rate. The pulse shaper code presented in chapter 5 was used to simulate the Incident waves. The stress strain curves were created by first calculating $\sigma(a,t)$, $\sigma(b,t)$, $V(a,t)$ and $V(b,t)$ and then calculating the average stress, and strain rate and strain from equation (6.40).

First, consider the low strain rate test in Figure 6.14. The test was done with the setup described in section 6.6. In the stress strain curves from the real test in Figure 6.14B, there is an offset in strain before the stress starts to rise. This is due to a small air gap between the bars and the specimen, which allow the bars to move without loading the specimen. Normally the specimen is kept in place with some grease and the strain offset of 0.19% correspond to 20µm, which is likely to be grease and air. The pre-simulate stress strain curve is created by running the simulated Incident wave through the GW model and calculating the stress, strain rate and strain. The "Post-simulated" curve in the strain rate plot was created by running the actual measured Incident wave through the GW model. The Pre-simulated model was offset with 0.19% strain to match the offset of the stress strain curves from the real tests. There is agreement between the simulation and the actual measured stress strain response. The simulated Incident wave has the same shape as the measured wave; however, there is a deviation in amplitude. The beginning of the measured wave lacks signs of yielding of the pulse shaper, which indicating some damping in the beginning of the initial elastic response of the pulse shaper. The measured stress equilibrium is above the simulated curve, but the measured stress equilibrium response does come below 5% relative deviation. The measured strain rate is actually the most stable compared to the simulated strain rates. The pre-simulation predicts first a stable region, and then an increasing strain rate. The increase is due to the Incident wave, which never becomes linear with the use of plastically deforming pulse-shapers. Therefore, at least a part of the increase in the strain rate curve can be explained from the input pulse, which changes loading rate as seen in Figure 6.14A.

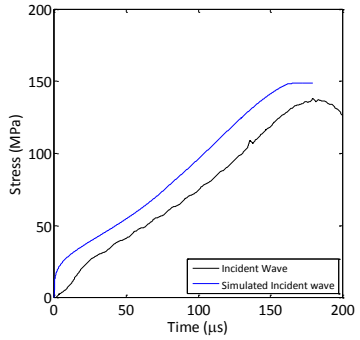

A) Incident wave with simulation from pulse shaper program

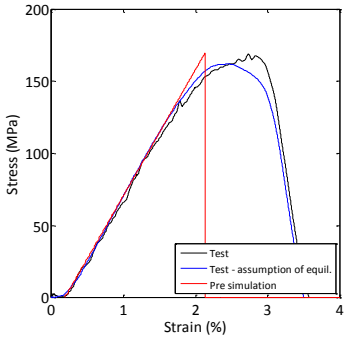

B) Stress-strain curves

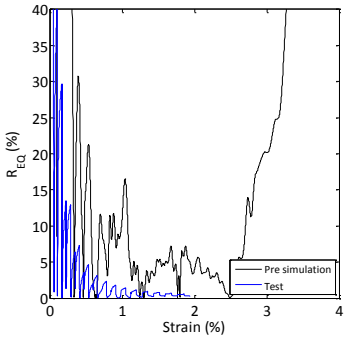

C) Calculated stress equilibrium R.

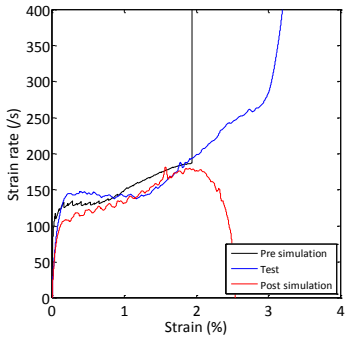

D) Strain rate as function of specimen strain

Figure 6.14 Pre and post simulation of the test "Low strain rate" in section 6.6.

The high strain rate test shown in Figure 6.15 also shows a simulated Incident wave with higher amplitude than the measured wave. In addition, the stress strain curves follow the same pattern as the low strain rate case. The simulated stress-strain curve agrees well with the measured stress-strain curve. The ripples at the beginning of the simulated stress-strain curve are due to the simulated Incident wave. The stress rate changes in the beginning due to the elasto-plastic behaviour of the pulse shaper. It takes several wave transits before the rate change is smoothed out. Figure 6.15C shows that the stress equilibrium never reaches a steady state below 5% relative deviation. The strain rate do not either find a steady plateau, but the pre-simulated, the measured, and the post-simulated curve agrees in the evolution of strain rate (Figure 6.15D). Feeding the measured Incident wave into the GW model generates the post-simulated curve.

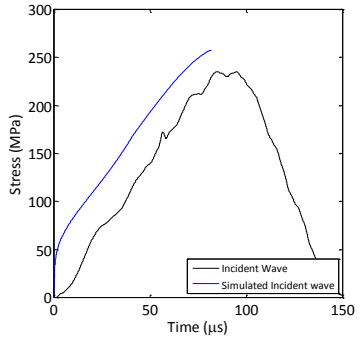

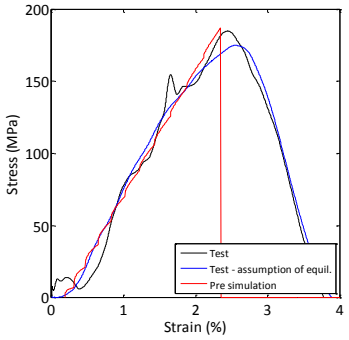

A) Incident wave with simulation from pulse shaper program *B) Stress strain curves*

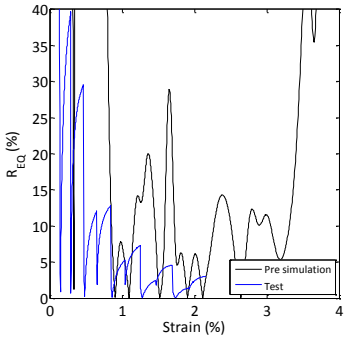

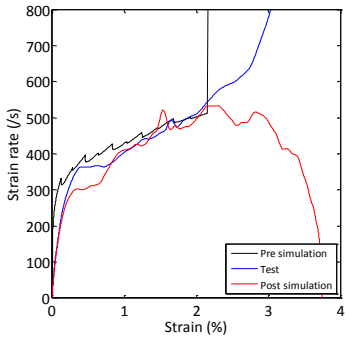

C) Stress Equilibrium *D) Strain rate as function of specimen strain*

Figure 6.15 Pre and post simulation of the test "High strain rate" in section 6.6

The coupling of the pulse-shaper simulation tool with the GW model creates a powerful tool to design and validate incident waves. For example, first the pre-simulated pulse is created based on the specimen design created with the design algorithm presented earlier. The Incident wave can then be generated in the SHPB without the specimen, and the measured wave can be fed through the GW model to simulate the response before an actual specimen is tested. This can help to reduce the trial and error, which would be used to find an acceptable set-up.

6.9 Summary

A generalized wave mechanics model (GW model) was derived that describes the response of an elastic specimen, dynamically loaded and situated between two elastic bodies. The model does not assume bars with the same mechanical impedance and further the model do not have assumptions of constant strain rate or stress equilibrium in the specimen. The model is then suitable to exploit the strain rate and stress equilibrium of a test set-up.

The model was exploited to show that a linear rising pulse is the only shape that balances a requirement of both constant strain rate and dynamic stress equilibrium. Next, the model was used to calculate the number of wave transits to both dynamic equilibrium and constant strain rate for *any* combination of machnical impedance of the specimen and bars. Further, the theoretical maximum strain rate is independent of the specimen length and is instead controlled by the impedance mismatches. Based on the algorithm to determine the equilibrium conditions, a design algorithm was derived that calculated the maximum achievable strain rate for any combination of specimen gage length and cross sectional area. The calculated setup satisfied both stress

equilibrium and constant strain rate at the same time. The GW model was implemented into a simulation tool, which coupled simulation of Incident waves with post processing of the simulated test. Together, the derived algorithms give a powerful tool to design tests in the SHPB and reduce the trial and errors towards a successful set-up.

7 An alternative momentum trap for the Split Hopkinson Pressure Bar

The Split Hopkinson Pressure Bar test rig is used for testing materials at high strain rates and reveal their behaviour under dynamic loadings. The loading rate is controlled by shaping of the Incident wave and the materials response is calculated from the Incident, Reflected and Transmitted wave. However, the reflected wave goes forth and back in the Incident bar and loads the specimen multiple times if the Transmitted bar does not move sufficient. This is the case in most tests as the duration and amplitude of the Incident wave is designed to fracture the specimen, which results in Reflected wave with longer duration and higher amplitude than the Transmitted wave. These repeated loadings are unwanted if the fracture load has to be coupled with a post analysis of the specimen, in for example a microscope.
To avoid the repeated loading the Incident bar has to be stopped after the first loading. The setup for this is called momentum traps. Two types of momentum traps are found in literature. The first setup was proposed by Nasser et al. [74] and is shown in Figure 7.1 The principle works with an tube fitted around the Incident bar and an added flange to the Incident bar. A reaction mass rests against the incident tube and restricts motion of the tube in the opposite end of the striker bar impact end. The incident tube has the same length as the striker bar. A compressive wave was generated in both the striker bar and the Incident bar upon impact. The wave in the tube travelled to the reaction mass where it reflected as compressive again, since the reaction mass acted as a stiff barrier. This compressive wave cames back to the flange when the tensile wave in the striker bar reached the interface and unloaded the Incident bar. The compressive wave in the tube then reflected off the flange and created a tensile wave in Incident bar. Thus, the incident compressive wave was followed by a tensile wave, which reversed the movement of the Incident bar/specimen interface after the Incident wave.

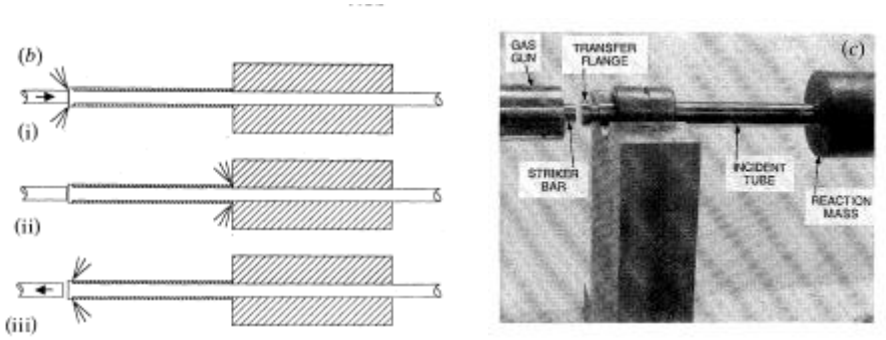

A) Principle of the momentum trap *B) Picture of setup.*

Figure 7.1 Momentum trap by Nemat Nasser [74]

The second type of momentum trap was proposed by Song [83]. It consists of a flange attached to the impact end of the Incident bar and a reaction mass mounted around the Incident bar. The distance between the flange and the reaction mass is set according to

$$D_I = \int_0^{\tau} C_I \varepsilon_I(t) dt \tag{7.1}$$

C_I is the elastic wave speed in the Incident bar and $\varepsilon_i(t)$ is the incident wave. When the flange reach the reaction mass the incident cannot move further and repeated loading is avoided. Figure 7.2 shows a schematic drawing of the concept.

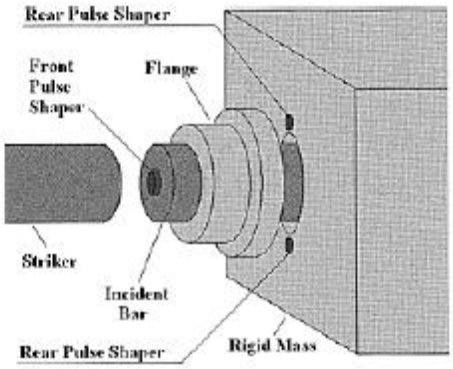

Figure 7.2 Momentum trap proposed by Song [83]

Pro and cons for the two methods has been listed in Table 7.1.

Table 7.1Comparison of momentum traps

	Pros	Cons
Nasser et al.	• Work without precision pre-setting a distance in the setup	• Incident tube must have same length as the striker bar. • Does not allow for controlled unloading of the specimen. • The tube take some of the amplitude of the incident wave and decrease the performance of the setup. • Requires special bearing for supporting the tube and the Incident bar has to rest in the tube. • Addition of reaction mass.
Song et al.	• Work for all sizes striker bars without exchanging any other parts • Allow for shaping of the unloading phase	• Require precise distance setup • Requires incident pulses to be created with high repeatability. • Addition of reaction mass.

The method by Song et al. requires less modification to the SHPB rig, but demands the displacement of the Incident wave to be known precisely. Repeatability may be hard to obtain as small variations in the gas gun pressure etc. creates different displacements from test to test under the same settings. The method by Nasser et al. does not have this restriction, but the setup make changes to striker bar length cumbersome as the tube length had to match the striker bar length. Further, the tube reduces the momentum introduced in the system and the momentum transferred to the specimen.

7.1 New method of momentum trapping

The distance between the bars was analysed to determine if multiple loading of the specimen did occur for a given setup. The interface/bar interface displacements during the first loading is calculated from the interface velocities as

$$D_a = \int_0^t C_I(\varepsilon_I(\tau) - \varepsilon_R(\tau))d\tau \tag{7.2}$$

$$D_b = \int_0^t C_T\big(\varepsilon_T(\tau)\big)d\tau \tag{7.3}$$

τ is the duration of the Incident wave. The final distance between the bars after the first loading then become

$$D_{final} = L_s - (D_a - D_b) \tag{7.4}$$

After the Incident wave has compressed the specimen, the wave becomes the reflected wave, which reverbed inside the Incident bar, and the Transmitted wave reverbed inside the Transmitter bar. For simplicity it is assumed the bar ends is completely free after the specimen is broken. Thus the reflection of the reflected wave becomes

$$\varepsilon_{R_{reflected}} = -\varepsilon_{I_{reflected}} \tag{7.5}$$

Then for each time the reflected wave passed interface (a) the interface moves the distance

$$D_{a(n_1)} = 2\int_0^t C_I\left(\varepsilon_{I_{reflected}}(\tau)\right)d\tau \tag{7.6}$$

And accordingly for interface (b)

$$D_{b(n_2)} = -2\int_0^t C_T\big(\varepsilon_{T_{Transmitted}}(\tau)\big)d\tau \tag{7.7}$$

The number of reverberation in the Incident bar is $n_1$with a period of

$$t_{I0} = \frac{2L_I}{C_I} \tag{7.8}$$

For the Transmitter bar with reverberation number n_2 the period is

$$t_{T0} = \frac{2L_T}{C_T} \tag{7.9}$$

The total displacement of interface (a) as

$$D_{atotal}(t) = D_a + n_1 D_{a(n_1)} + 2\int_{t-n_1\cdot t_{I0}}^t C_I\left(\varepsilon_{I_{reflected}}(\tau)\right)d\tau, \quad n_1 = \left\lfloor\frac{t}{t_{I0}}\right\rfloor \tag{7.10}$$

For interface (b) the total displacement is

$$D_{btotal}(t) = D_b + n_2 D_{a(n_1)} + 2\int_{t-n_2\cdot t_{T0}}^t C_T\left(\varepsilon_{I_{reflected}}(\tau)\right)d\tau, \quad n_2 = \left\lfloor\frac{t}{t_{T0}}\right\rfloor \tag{7.11}$$

By evaluating equations (7.10) and (7.11) for a certain time it could be observed if the distance between the bars became smaller than the minimum distance obtained during the compression of the specimen. If this was the case, the specimen was subjected to multiple loadings. Figure 7.3B and C shows an example of the use of equations (7.10) and (7.11). The relative interface displacement is calculated as $(D_{atotal}(t) - D_{btotal}(t)) - (D_a - D_b)$. Thus, Figure 7.3C gives the relative motion of the interfaces after the first loading.

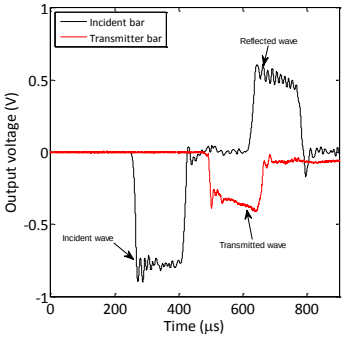

A) Examples of waves. The reflected and transmitted wave reverbs around in the Incident bar and Transmitter bar respectively.

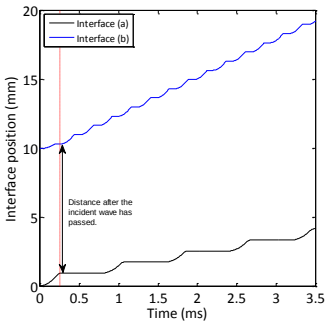

*B) Plot of the interface position for a setup **without** multiple loading of the specimen.*

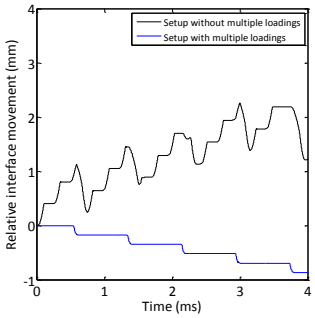

C) Relative interface movement. Values below zero means the interfaces approaches each other.

Figure 7.3 Interface motion and evaluation if multiple loading had happen.

Table 7.2 Details for setups in Figure 7.3C.

Setup	Specimen details	Incident bar	Transmitter bar	Striker bar
Setup with multiple loading	15x15x15mm (W x H x Ls)	Stainless steel D = 25mm L = 2001mm E = 191GPa P = 7741kg	Stainless steel D = 25mm L = 2000mm E = 191GPa P = 7741kg	D = 25mm L_{ST} = 100mm V_0 = 15.7m/s
Setup without multiple loading	12x12x10mm (W x H x Ls)	Stainless steel L = 2001mm E = 191GPa P = 7741kg	Aluminium L = 617 mm E = 73.5GPa P = 2809 kg	D = 25mm L_{ST} = 150mm V_0 = 19m/s

The setup with negative values of relative interface movement compressed the specimen further than the initial loading. The exact numbers in Figure 7.3C here are not correct, as they were calculated without the specimen between the bars after the initial loading. If the specimen are present, the Reflected wave would lose energy every time the specimen was hit, while the Transmitted wave would gain energy. Thus, the plot in Figure 7.3C only indicates if multiple loading occurs or not.

Due to the short loading time, even for multiple loading, the specimen doesn't have time to accelerate downward, by the gravity, between the bars. If the bar diameter is 25mm and the specimen would have to move 20mm or more to be completely free of the bars. Using constant acceleration, this would take 64ms and within 64ms, the Incident bar would hit the specimen more than 128 times according to the timescale in Figure 7.3C.

As indicated in Figure 7.3 an alternative way to avoid the specimen to be loaded multiple times is to ensure the Transmitter bar moves faster away from the specimen than the Incident bar approaches it after specimen failure. The displacement of the bar interfaces is controlled by the displacement of the Reflected and Transmitted wave, and the frequency at which the wave reached the interface. This frequency is controlled by the Transmitter bar length and the wave velocity of the bar. Multiple loading can be avoided by designing the Transmitter bar to move faster away from the specimen, by adjusting the displacement of the reverbing wave and the reverberation frequency. Thus, by exchanging the Transmitter bar, to a bar of suitable length and material, single loading of the specimen can be achieved.

In the SHPB setup described in chapter 6 the Transmitter bar were original a 2mtr steel bar, but was exchanged to an aluminium bar to check the findings here, and the GW model was used to

simulate Transmitter bars made from from different materials. Details are given in Table 7.3

Table 7.3 Details for SHPB setup with modified Transmitter bar

Part	Details
Specimen	12 x 12 x 10 mm E_s = 10GPa ρs =1953 kg/m^3
Incident bar	D_I = 25mm L_I = 2001mm E_I = 191GPa ρ_I = 7741kg/m^3
Transmitter bar (To be validated)	D_T = 25mm L_T = 617mm E_T = 73.5GPa ρ_T = 2809kg/m^3

The Incident waves were identical to those presented in Figure 6.12 and is presented as low, medium and high strain rate. The new Transmitter bar was made from aluminium and shortened to 617mm in length and was exchanged for a stainless steel bar similar to the Incident bar described in Table 7.3. In principle, the Transmitter bar could be varied arbitrarily in size and material. However, in reality the material choice is limited so the bar material alternatives was narrowed down to an aluminium, a steel and a magnesium bar. Their diameters were locked to the diameter of the Incident bar while the length could be varied as needed. The "low strain rate" Incident wave was used to compare the materials. The GW model was set up with the steel Incident bar and the Transmitted bar made from one of the materials to choose between. The Reflected and Transmitted waves were calculated and equations (7.10) and (7.11) were combined to calculate the relative distance between the bars after the first loading to failure. The calculations were carried out for lengths between 0.1 and 3mtr of the Transmitter bar. If the relative distance was found to be negative within 10 reverberations of the Reflected wave in the Incident bar, then the design was found non useable. The choice of Transmitted bar influenced the obtainable strain rate and for each material, the maximum strain rate was calculated.

The wavelength of the transmitted wave were also considered as short lengths of the Transmitter bar increases the risk of overlapping waves at the strain gage. The wavelength was calculated by multiplying the duration of the simulated Transmitted wave with the wave velocity of the bar material. Table 7.4 present the findings of the simulations. The reflection coefficients B1 and B2, and the maximum strain rate and the corresponding stress rate in the Incident bar are also included.

Table 7.4 Simulation results

Table header	Aluminium	Stainless steel	Magnesium
E (GPa)	73.5	191	45
ρ (kg/m^3)	2809	7741	1738
B1 (Reflection coefficient – Specimen to Incident bar)	0.932	0.932	0.932
B2 (Reflection coefficient – Specimen to Transmitter bar)	0.827	0.932	0.734
Max strain rate (/s)	219	121	303
Max stress rate (MPa/μs)	1.17	0.37	2.44
Calculated wave length (mm)	670	590	1020
Maximum bar length (mm)	1200	400	2000
Loading to specimen failure	Yes	Yes	No

The simulation results in Table 7.4 shows that the stainless steel material requires a Transmitter bar of maximum 0.4m to allow the bar to move away quickly enough. This is problematic as the strain gage always should be placed 10 times the bar diameter away from the specimen end [18, 71]. The bar iss 25mm in diameter so it leaves 150mm bar behind the strain gage and a maximum

wavelength of 300mm to avoid the wave overlapping at the strain gage. The calculated wavelength for the Transmitted wave is 590mm so the wave will overlaps itself at the strain gage with a Transmitter bar length of 400mm. Further, the maximum strain rate calculated for stress equilibrium and constant strain rate at specimen fracture, is low due to a high impedance mismatch, which requires many wave reverberations to ensure constant strain rate according to Figure 6.10.

The magnesium bar gives a maximum length of 2mtr. Since magnesium is less stiff than steel, it will deform more for the same load and move faster away than a steel bar of the same length. However, the magnesium bar is not able to load the specimen up to fracture. The specimen would simply push the bar away before fracture according to the simulation. The aluminium material provided the compromise between the steel and magnesium options. The maximum bar length is calculated to 1,2mtr and a wavelength to 670mm and an inability to fracture the specimen. Thus, aluminium is validated as the material choice for the bar. The maximum bar length were then calculated for the other Incident waves in Figure 6.12. The "medium rate" allowed a maximum length of 800mm and the "high rate" allowed a maximum length of 600mm. Thus, the 617mm aluminium bar is on the low end regarding the length. Data for tests performed with the bar with all the Incident waves from Figure 6.12 were used for check if repeating loading has occurred. The displacement of the Reflected and Incident wave were calculated from equations (7.6) and (7.7), and the relative interface movement were calculated from equations (7.10) and (7.11). The calculations are plotted in Figure 7.4 and they show that the "low rate" and "medium rate" tests did not have repeated loading whereas the "high rate" had a small degree of repeated loading (Relative interface movement below 0mm at a few times).

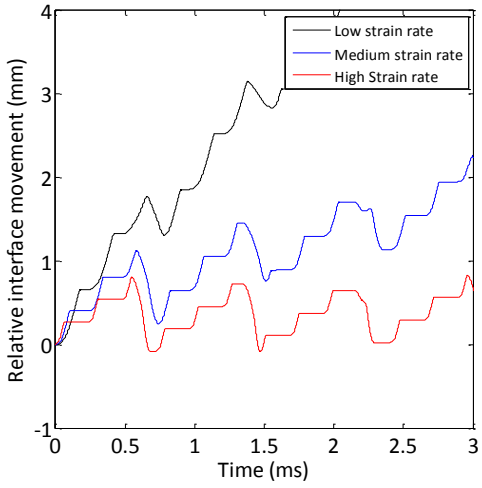

Figure 7.4 Relative interface movement for different specimen strain rates

7.2 Summary

An alternative momentum trap method for the compressional SHPB was presented. The method

works by using a short and light Transmitter bar, such that it moves faster than the Incident bar after specimen fracture. This ensures no further compression occurs on the specimen. A design example was given in the form of a validity check of an already installed version of the method. The design example included the necessary equations to calculate if the specimen experienced repeated loading, and it was described how the GW model from chapter 6 were used to simulate the design example. This proposed momentum trap method was simpler to apply as it only requires an exchange of the Transmitter bar. However, the length and choice of bar material must be selected with respect to the specimen to test, and the Incident waves to be applied. The bar will be limited to these settings as a change in the Incident wave may change the ratio of the Incident bar and Transmitter bar movement. A bar design is then designed to a given setup, and do not work universal for all selections of Incident waves and specimen size and material.

8 Through Thickness strain rate sensitivity of Eglass/Epoxy and Eglass/Lpet UD composite

This chapter present an investigation of the through thickness strain rate behaviour of two fibre-reinforced polymers (FRP). An Eglass/Epoxy (Thermoset matrix) and an Eglass/Lpet (Thermoplastic matrix) FRP is compression tested from 150 to 400/s with the SHPB described in chapter 5. The results was used as validation cases for the model presented in chapter 6, and as input data for the RESIST project mentioned in the preface.

8.1 Materials

Material specifications for the Eglass/Lpet and Eglass/Epoxy materials are shown in Table 8.1. Specimens were cut with a diamond saw and milled to final dimensions of 12x12x10mm (width x lenght x thickness). Examples of the specimens are shown in Figure 8.1. Department of Wind Energy (DTU) tested the materials under static condition and all result noted as "static" comes from [62, 63]. In the static case the specimen size was 20 x 20 x 40 mm (width x length x thickness) for stiffness measurements and 25 x 25 x 40mm (w x h x t) with a waist cross section of 16 x 16mm (w x h), The latter was used for strength testing only.

Table 8.1 Material details

Property	Eglass/Epoxy	Eglass/LPET
Panel size	200x200x21,9mm	250x250x22mm
Fabrics	Non crimp fabric SAERTEX S14EU990-00940-T1300-499000 With 950g/m^2	E-glass 1200 tex 4588 WG2-LPET-1000-UD With 1050g/m^2
Area weight	43,4kg/m^2	
Layup	$[0°]_{36}$	$[0°]_{44}$
Matrix	Araldite LY 564 Epoxy with Aradur 917 harder and DY 070 accelerator	LPET
Production method	Vacuum Infusion	Vacuum consolidation

A) Specimens for high strain rate testing

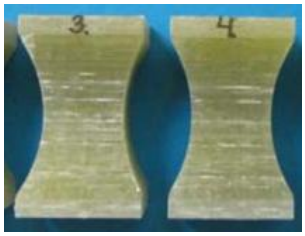

B) Specimens for quasi-static test of strength [62, 63].

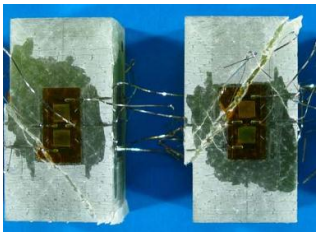

C) Specimens for quasi-static test of the elastic modulus. [62, 63].

Figure 8.1 Test specimens

8.2 Test setup

The Split Hopkinson Pressure Bar at University of Southampton was used for tests at high strain rates. The test rig is described in chapters 5, 6, and 7, and the test rig is shown in Figure 8.2 together with typical waves from a test. The test rig is equipped with a stainless steel Incident bar and a stainless steel Transmitter bar, both 2mtr long, however the Transmitter bar is changed to a 0.617mtr long aluminium bar to ensure single loading of the specimens according to chapter 7.

A) The Split Hopkinson Pressure Bar

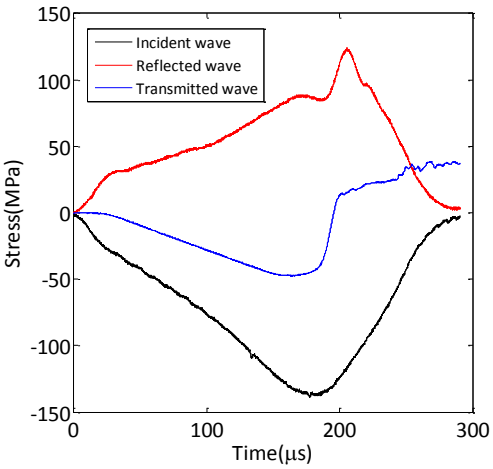

B) Typical recorded waves from a test

Figure 8.2 The Split Hopkinson Pressure Bar

Pulse shaping with copper discs as described in chapter 5 was used to enable test at different strain rates. Originally, the pulse shaping was done with a rounding of the impact end of the Incident bar, however this was insufficient to produce the required Incident waves. The pulse shaper code described in chapter 5 and the GW model described in chapter 6 was used to design three Incident waves to achieve three strain rates. Examples of the waves are given in Figure 8.3B, and The strain gage position is the distance between the strain gage on the bar and the specimen.
Table 8.3 gives details of set-up. Figure 8.3 also shows waves from the two pulse shaping methods. The bar calibration method described in chapter 5 and details of the bars are provided in table 8.2.

Table 8.2 Bar data

Parameter	Incident bar	Transmitter bar	Striker bar
Material	Stainless steel	Alu 7075 T651	Stainless steel
Length (mm)	2001	617	100/150mm
Strain gage position (mm)	1021	276	-
E (GPa)	191	73.4	191
Density ρ (kg/m^3)	7741	2809	7741
Wave speed C (m/s)	4978	5112	4978

The strain gage position is the distance between the strain gage on the bar and the specimen.

Table 8.3 Pulse shaper setup

	Low Strain rate	Medium strain rate	High Strain rate
Material	Copper	Copper	Copper
Pulse shaper dimension (Diameter * Thickness)	8.73mm x 2mm	9.53mm x 2mm	11.41mm x 2mm
Strikerbar length (mm)	150	150	100
Impact velocity (m/s)	13	19	24

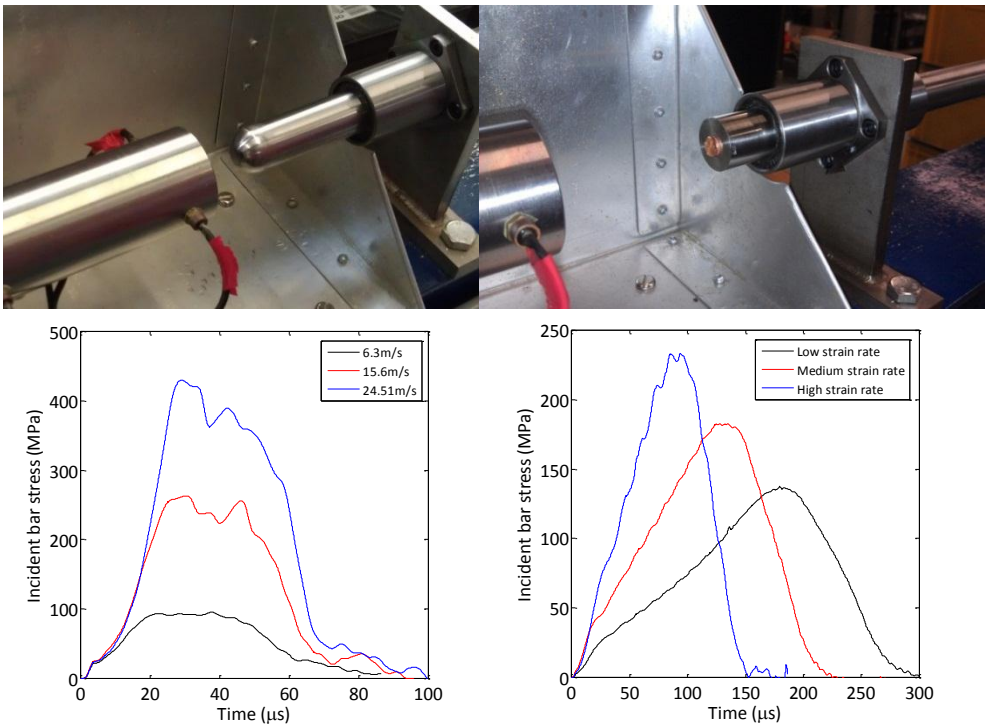

A) Rounded bar pulse shaping *B) Copper disc pulse shaping*

Figure 8.3 Incident waves from the Rounded bar pulse shaping method and the Copper dics method

The test rig were equipped with a gas gun able to achieve striker bar velocities up to 30m/s. The velocity was measured with a light gage mounted in the muzzle of the gas gun. The bars were equipped with two strain gages each. The strain gages had a gage length of 2mm and were placed opposite to each other, and connected in bending compensation mode as shown in Figure 8.4B.

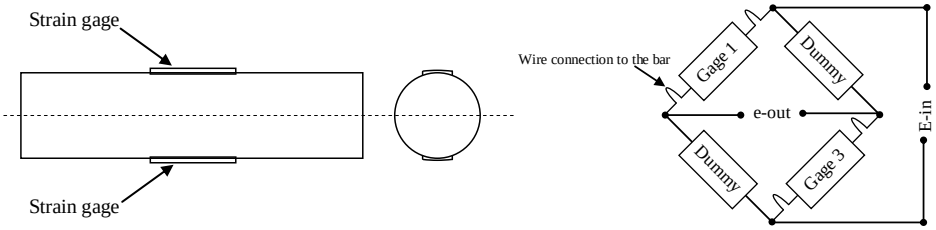

A) Gage position on bar *B) Wheatstone bridge setup*

Figure 8.4 Strain gage setup on the bars

The strain gages were conditioned with a FYLDE HT379TA strain gage amplifier with a slew rate of 8V/µs. The setup was shunt calibrated before performing a test. A four channel Picoscope 4427 scope was used for collecting data from the Incident and Transmitter bar and the light gage, at a sampling rate of 20 MHz.
The collected data were post processed in a custom-made MatLab program to produce a stress-strain curve and a strain rate curve for each test. The time synchronisation method described in chapter 5 was used to synchronise the waves before calculating the stress strain curve. Since the bars were unequal, the "modern" formulas, equations (8.1), were used for calculating stress and strain.

$$\begin{aligned}\sigma(a,t) &= \frac{A_I E_I}{A_s}\big(\varepsilon_I(t) + \varepsilon_R(t)\big)\\ \sigma(b,t) &= \frac{A_T E_T}{A_s}\big(\varepsilon_T(t)\big)\\ \varepsilon(t) &= \frac{1}{L_s}\int_0^t C_I\big(\varepsilon_I(\tau) - \varepsilon_R(\tau)\big) - C_T\varepsilon_T(\tau)\,d\tau\end{aligned} \tag{8.1}$$

Five specimens were tested for each strain rate and for each material, such that in total 30 tests were conducted. The specimen dimensions were kept constant for all loading rates and were the same for both the Eglass/Epoxy and Eglass/Lpet material.

8.3 Results

The failure stress and failure strain, and elastic modulus were calculated from the stress-strain curve. The maximum stress defined the failure stress and the corresponding strain defined the failure strain. The elastic modulus was calculated in the interval 1 – 1.8% strain. Strain rates were defined as the average strain rate in the strain interval from 1 – 2% strain. The three strain rate levels were named "Low", "Medium" and "High". Typical profiles are shown in Figure 8.6A and the obtained strain rates is shown in Figure 8.5B. Figure 8.6 shows the repeatability of the strain rate profiles. The examination of the setup in chapter 6 proposed that constant strain could not be reached with the high stress rate in the Incident wave for the given specimen/bar combination. The medium and low strain rate showed a more stable evolution in strain rate. However, the low strain rate showed a distinctive bend in the strain rate. Figure 8.6 shows it was present for all specimens and of the two materials. The Eglass/Epoxy developed a higher strain before the acceleration in strain rate compared to the Eglass/Lpet.

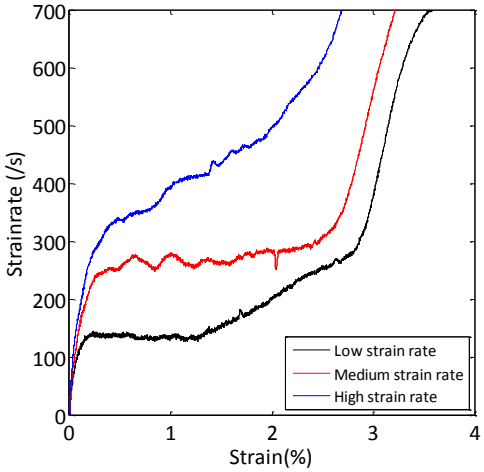

A) Strain rate vs. strain.

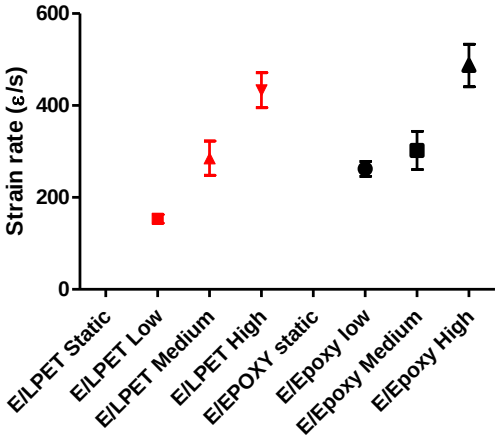

B) Strain rates shown with 95% confidence interval.

Figure 8.5 Strain rates

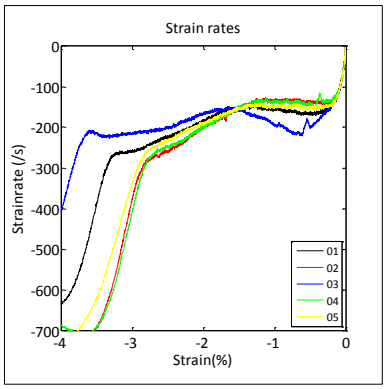

A) Eglass/Lpet – low strain rate

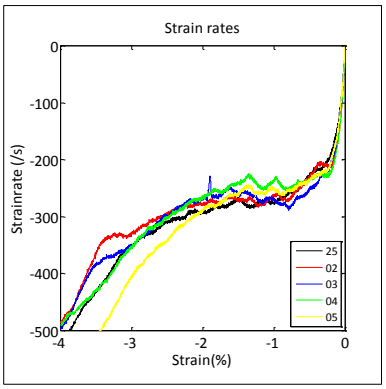

B) Eglass/Epoxy – low strain rate

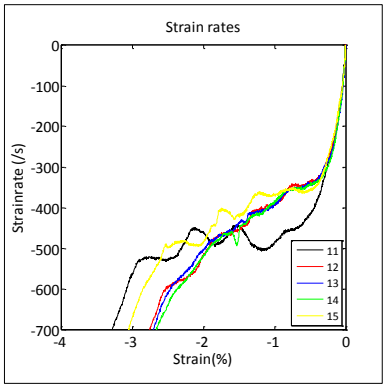

C) Eglass/Lpet – high strain rates

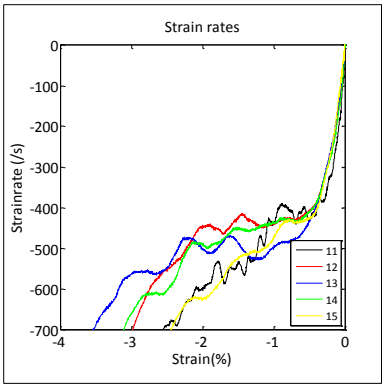

D) Eglass/Epoxy – low strain rates

Figure 8.6 Strain rate vs. strain curves

Figure 8.7 shows stress strain curves for the low and high strain rate of the Eglass/Lpet material. The high strain rate curves were affected by the noisy incident waves. The pulse shaper design

with a diameter of 11.4mm for this group was on the high limit according to the finding in chapter 5. The fact that the curves in Figure 8.7B shows unloading stages, reveals that the quality of the generated Incident waves was doubtful.

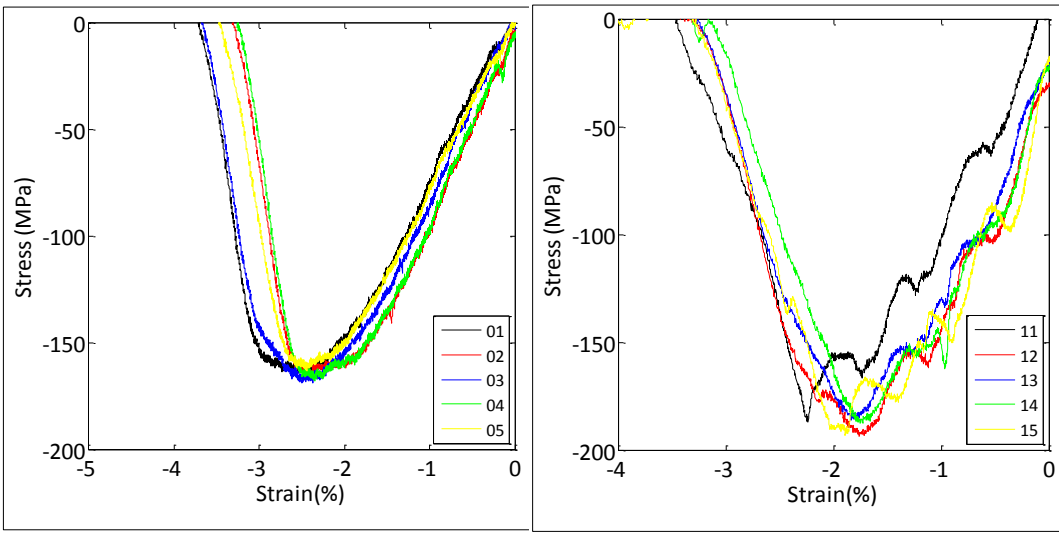

A) Eglass/Lpet at low strain rate *B) Eglass/Lpet at high strain rate*

Figure 8.7 Examples of stress strain curves.

Table 8.5 shows the calculated mean value and 95% confidence interval in parentheses for the failure stress, the failure strain, the E modulus, and the average obtained strain rate.

Table 8.4 Eglass/Lpet – TT Compression

			Nominal strain rate		
Property	**Unit**	**Static**	**1/s**	**150/s**	**400/s**
Failure Stress (X_{33}^t)	MPa	120.4 (81.1)	166 (2)	170 (14)	189 (4)
Failure Strain (XS_{33}^t)	%	1.64 (0.12)	2.40 (0.06)	2.20 (0.3)	1.90 (0.25)
Elastic modulus (E_{33}^t)	GPa	11.1 (0.1)	8.7 (0.6)	7.1 (1.1)	9.0 (0.7)
Obtained strain rate	/s		154 (7)	285 (37)	433 (38)

Table 8.5 Eglass/Epoxy – TT Compression

			Nominal strain rate		
Property	**Unit**	**Static**	**1/s**	**150/s**	**400/s**
Failure Stress (X_{11}^t)	MPa	186 (15)	183 (10)	193 (11)	203 (12)
Failure Strain (XS_{11}^t)	%	1.84 (0.23)	2.73 (0.15)	2.58 (0.41)	2.63 (0.55)
Elastic modulus (E_{33}^c)	GPa	16.0 (0.7)	8.7 (0.9)	9.6 (1.0)	8.4 (2.6)
Obtained strain rate	/s		262 (16)	302 (2)	487 (46)

Figure 8.8 shows the mean values plotted with their confidence interval. Eglass/Lpet showed first an increase in failure strain and then a drop with increasing strain rate. This indicated a change in failure mechanism with strain rate. Eglass/Epoxy showed an increase in failure strain from quasi static to the lowest strain rate and then a stable level. Both materials experienced an increase in failure stress with strain rate with the highest increase for the Eglass/Lpet. The Eglass/Lpet also showed a higher increase in failure stress from quasi-static strain rate to the lower strain compared to the Eglass/Epoxy.

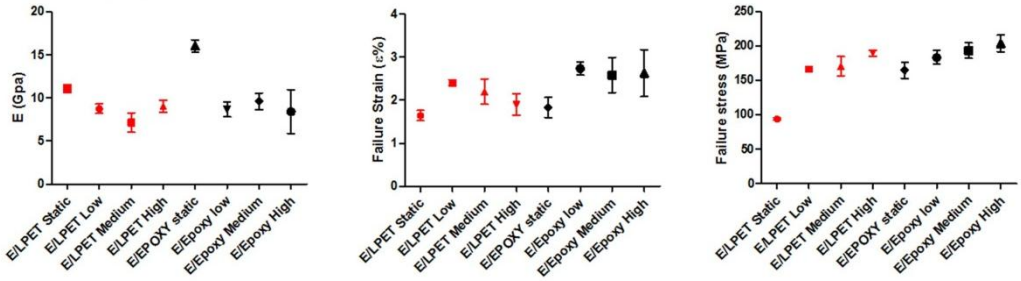

Figure 8.8 Graphical representation of the results with confidence intervals

For both materials the elastic modulus decreased with increasing strain rate. Figure 8.9 shows stress-strain curves of Eglass/Lpet obtained in the SHPB, and under quasi-static conditions. 90° inplane compression tests was also carried out under quasi static conditions and for a UD lay-up, the 90° direction should be the same as the through thickness direction. There is slight difference in elastic modulus between the SHPB test and the quasi-static tests. Most of the decrease in the E modulus comes from the difference in strain interval used for calculating the elastic modulus. In the quasi-static test, the range 0.05-025% was used, whereas 1-1.8% was used for the SHPB tests. The data below 1% strain were acquired in a non-equilibrium state.

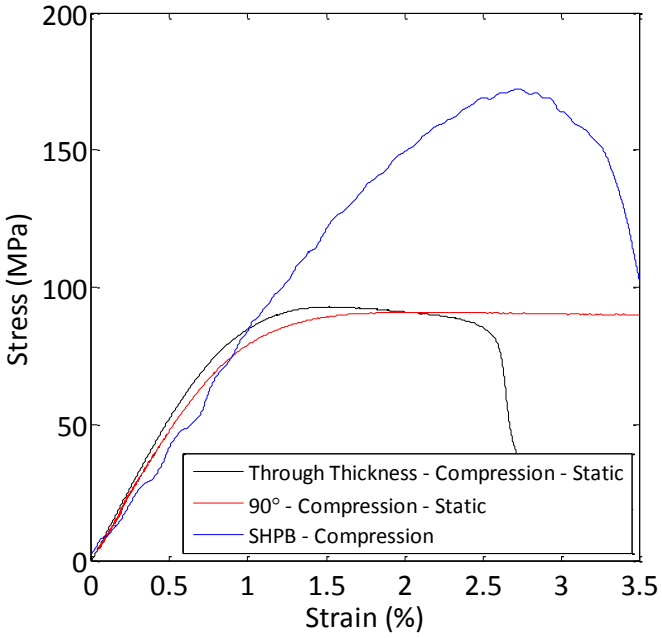

Figure 8.9 Stress-strain curves for Eglass/Epoxy

Figure 8.10 shows photographs of the specimens after test. Despite the difference in geometry of the quasi-static and the SHPB specimens, they possessed the similar crack patterns. The Eglass/Lpet specimens seemed to possess more brittle behaviour at the higher strain rates with smaller cracks. This finding was in agreement with the stress-strain curves, where a more brittle behaviour was seen with increasing strain rate.

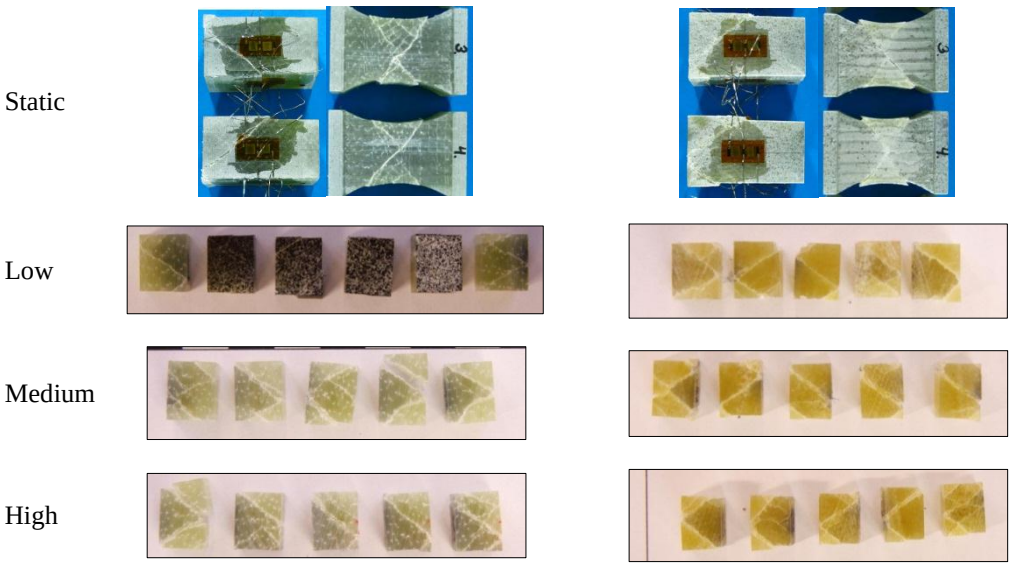

A) Eglass/Epoxy *B) Eglass/LPET*

Figure 8.10 Post-test photographs of the specimens. Photographs of the static specimen were taken from [62, 63].

8.4 Digital Image Correlation Check

Four tests of Eglass/Epoxy at low strain rate were conducted with a Vision Research V1610 high-speed camera to monitor the SHPB test. A speckle pattern was painted on the surface of the specimen and the Digital Image Correlation software ARAMIS 2D from GOM [99] was used to determine the strain field on the surface. The strain measurements were taken as an average of the facets within the red square in Figure 8.11A. The DIC strain measure was used with the stress measure from the SHPB to generate stress strain curves. Comparisons of the elastic modulus are shown in Table 8.6 and the stress strain curves are shown in Figure 8.11B. A paired T test was conducted with the hypothesis, that the means were equal. The P value was found to be P = 0.49, so the mean level were not significantly different. The DIC measurement then verified the use of the "modern" post processing equations.

Table 8.6 Estimated elastic modulus

Specimen	SHPB analysis E modulus (GPa)	DIC Analysis E modulus (GPa)
01	7.54	7.83
02	9.34	9.83
03	9.66	8.85
04	8.65	7.33

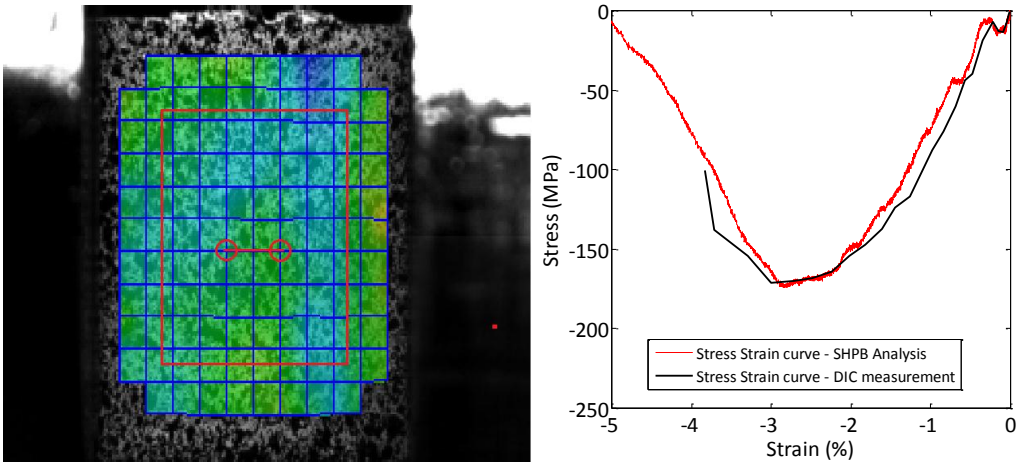

A) Extraction of strain data. *B) Comparison of stress strain curves.*

Figure 8.11 DIC data post processing.

Figure 8.12 shows the how the major strain concentrates in a small region in the specimen for an Eglass/Epoxy. The concentration developed already at 133MPa which corresponded to a average major strain of 1.5%. This was the point where the strain rate increased from a stable level in the low strain rate test, so the DIC measurement suggested that the reason for the bi linear evolution in strain rate was due failure progression in the specimen.

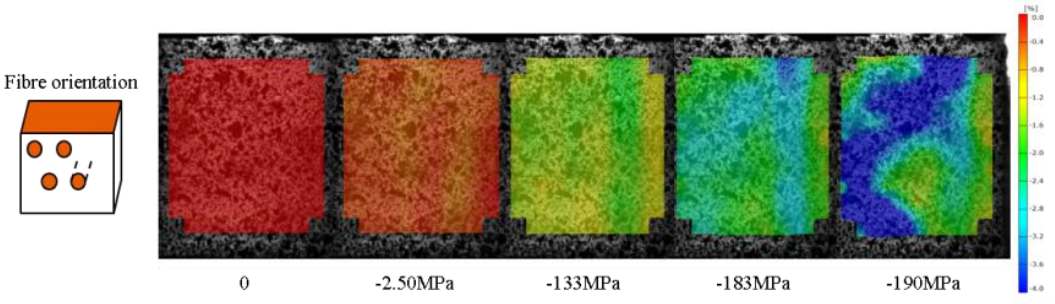

Figure 8.12 Example of how the major strain evolves from an uniaxial state into a state with strain concentration upon failure. At -133MPa it was seen that the strain started to concentrate at the right side at the Transmitter bar.

8.4.1 Microscope investigation

Some specimens were post analysed by capturing scanning electron images of the fracture surfaces. No differences were found between specimens tested at different strain rates. However, there was a significant different is fracture surfaces. Figure 8.13 shows that the Eglass/Lpet had a more ductile behaviour in terms of less splitting of the matrix compared to the Eglass/Epoxy, which has little adherence of epoxy to the fibers. This is contradictory to the behaviour in the failure strain plot where the Eglass/Epoxy had higher strain to failure for all strain rates. The momentum trap installed in the test rig ensured that fracture surface was created with a single loading.

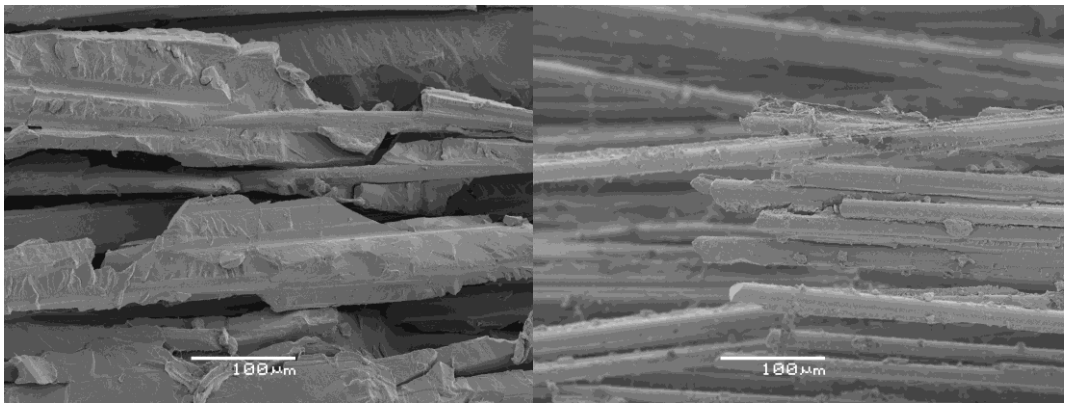

A) Eglass/Lpet *B) Eglass/Epoxy*

Figure 8.13 Scanning electron microscope images.

8.5 Summary

A thermoset (Eglass/Epoxy) and thermoplastic (Eglass/LPET) fibre reinforced material was tested for strain rate sensitivity in the thickness direction for a UD layup in a Split Hopkinson Pressure Bar. The strain rates ranged from quasi static to 400/s.

The failure stress of Eglass/LPET showed a higher sensitivity to strain rate than Eglass/Epoxy. For failure strain, the Eglass/Lpet showed an increase from quasi-static strain to 150/s and then a slowly decreasing tendency with increasing strain rate. This behaviour indicates a shift in failure mode inside the material.

For both materials, the elastic modulus was found to decrease with increasing strain rate.

DIC measurements suggested that the bilinear evolution in the strain rate was due to failure progression in the specimen.

9 Summary and Conclusion

The high strain rate characterisation of FRP materials present the experimenter with a new set of challenges in obtaining valid data. These challenges were addressed in this work.
Chapter 1 introduced the concept of wave motion in solids, and the wave equation was used to introduce the stress equilibrium process in a solid. Theoretical maximum impact velocities were presented to show that the impact velocity could not be endlessly increased to increase the strain rate. The approach also indicated that the applied deformation history should be controlled and adapted to the test material to reach a homogenous stress state in the specimen before failure. The high-speed servo-hydraulic test machine and the Split Hopkinson Pressure Bar are used for high strain testing of FRP materials. They complement each other in their accessible strain rates as they represented two distinct ways of introducing the deformation into the specimen. The methods were widely used for testing metallic materials, but accepted testing standards may not be directly transferrable to testing FRP materials. A literature survey indicated contradictory results that possibly arise from challenges with the testing methods. The remaining work was devoted to re-examining the high-speed servo-hydraulic test machine and the Split Hopkinson Pressure Bar in terms of testing linear elastic FRP materials.
Chapter 2 presented a model to simulate the influence of the load train of a high-speed servo-hydraulic test machine on the stress and deformation state in the test specimen. It was found that:

- A linear elastic specimen cannot be deformed with a constant velocity in a high-speed servo-hydraulic test machine due to inertial damping in the load train and open loop control of the piston rod velocity.
- The specimen deformation rate was controlled by the mass of the moving grip.
- Load ringing occurred as an effect of high acceleration of the system and the amplitude is determined by the acceleration of the system. The strategy with a built-in load cell could not easily be realised for polymeric fibre composites as the measurement relies on a complete linear response as well as the ability to vary the cross section of the specimen.
- The non-rigid connection between specimen and piston rod in the conventional slack adapter led to oscillations in the velocity. The frequency of the oscillations was low such that the specimen would fail within the first period of the oscilations.
- The rigid connection created with the Fast Jaw system and combined with the fast gripping mechanism, lead to oscillations in the load cell before fracture of the specimen.
- A time lack between strain and stress was observed in the simulations at higher impact velocities, which would influence the estimation of the E modulus.
- Trapped air in a conventional slack adapter could cause high loading on the specimen before high deformation velocities were reached. This could cause weak specimens to fracture before a high strain rate was reached.
- As far as specimen fabrication and load ringing are concerned, a conventional slack adapter design may be preferable for testing elastic materials, whereas the Fast Jaw system using the developed techniques is more suitable for testing metallic materials.

Chapter 3 presented the design and construction of a high-speed servo-hydraulic test machine

- The design process illustrated the added complexity and cost added to the test machine to reach higher deformation velocities.
- The grips and slack adapter were custom designed for the machine.
- The final machine was able to obtain piston rod velocities in excess of 25m/s.

Chapter 4 presented material tests carried out on the test machine described in chapter 3.

- An Eglass/Epoxy, an Eglass/Lpet and Carbon/PA6 material were tested at three impact velocities and in three specimen configurations. In total more than 120 tests were carried out. The layups were UD 0°, UD 90° and Quattro axial.
- It was not possible to obtain constant strain rates for any of the tests.
- It was not possible to test the 90° specimens at high strain rate in tension as they fractured before they were accelerated to higher deformation velocities.
- The general tendency was an increase in failure stress and failure strain.
- The Elastic modulus and Poisson's ratio were in general unaffected by the increased strain rate.

The test series presented certain difficulties, as it was not possible to obtain constant strain rates for any of the tests. The model in chapter 2 was developed during the post-processing of the data and the model supported the observed tendency, namely that a constant strain rate was not possible. The model indicated the reason to be the inertial damping in the load train and the inability of the system to maintain the impact velocity. Chapters 2 and 4 thus support each other in the conclusion that it may be difficult to obtain constant strain rates in the high-speed servo-hydraulic test machine. Furthermore, it may also be problematic to obtain even modest deformation velocities for materials with low strain-to-failure.

Chapter 5 presented a description of the compressional Split Hopkinson Pressure Bar

- It was found that the dominant pulse shaping method was limited by frictional properties. The method thus possesses a limit in the stress rate that can be applied to the test specimen.
- The importance of accurate calibration of the test rig was emphasized and a simple new method for calibrating the wave velocity was presented.

Chapter 6 presented a wave mechanics model (GW model) to estimate the specimen behaviour in the SHPB test rig.

- The model was derived without assumptions of either constant strain rate or stress equilibrium and had restrictions on the choice of bars.
- The literature had shown that the linear rising Incident wave would promote stress equilibrium and constant strain rate. The model was used to predict the number of wave transits in the specimen to achieve both stress equilibrium and constant strain rate for all possible combinations of bars for a linear rising Incident wave. The findings provide useful information for selecting bars and set-up. For example to model showed that a high impedance mismatch at the Transmitter bar would facilitate stress equilibrium, but extend the time to constant strain rate, unless the Incident bar had a low impedance mismatch to the specimen.
- The model was implemented into a design algorithm to design specimens for the SHPB test rig. It was possible to estimate the maximum strain rate for a given specimen size and the associated maximum stress rate in the Incident pulse.
- It could be concluded that only linear rising Incident waves would satisfy both a stress equilibrium state and a constant strain rate at the same time.

- The requirement of a linear rising pulse means the acceleration of the Incident bar must be constant and not the velocity of the Incident bar. A constant velocity in the Incident bar would result in a decreasing strain rate in the specimen throughout the test.

Chapter 7 presented a new momentum trap for the SHPB test rig.

- The method works by modifying the Transmitter bar such that it would move faster away from the specimen than the Incident bar would approach the specimen.
- The consequences for stress equilibrium and strain could be assessed with the model in chapter 6.
- The method is easy to implement, but was restricted to the specimen set-up for which it was designed.
- The method was verified with both high-speed videos and the model from chapter 6.

Chapter 8 presented a set of compression tests in thickness direction of the materials in chapter 4

- The pulse shaping method presented in chapter 5 was used to create smooth rising Incident waves for three strain rates.
- The momentum trap method described in chapter 7 was used to ensure single loading of the specimens.
- Strain measures were compared with DIC measurements. They agreed and validated the set-up and the post-processing of the data.
- The model in chapter 6 showed that the test fastest test were fracturing the specimen before a constant strain rate was obtained. The measured data provided the same information and helped validate the model in chapter 6.
- An increase was seen in the failure stress for both the Eglass/Epoxy and the Eglass/Lpet.
- For the failure strain, there was a significant drop at the highest strain rate for the Eglass/Lpet, whereas this drop was not seen with the Eglass/Epoxy.
- to high strain rates

9.1 Perspective

When the findings are combined, the high-speed servo-hydraulic test machine is clearly less suitable for high strain rate testing of FRP materials if an constant strain rate is desired. The set-up with grips and slack adapter was found troublesome. In addition, the inertia forces proved to be particularly difficult to handle. This is problematic because the high-speed servo-hydraulic test machine could close the gap, in accessible strain rates, between quasi-static rates and the lower strain rate limit of the SHPB. The SHPB was found to have the potential to achieve both constant strain rates, and stress equilibrium. However, challenges exist in controlling the Incident waves, which is the key to successful testing in the SHPB test rig. The developed model of the specimen response would also be applicable for a tensile set-up, which would be the natural place to continue this work. The tensile set-up has some extra challenges such as fixing the specimens to the bars. Grips could corrupt the reflection point and would require the strain to be measured directly on the specimen, for example with DIC. This also proved to be successful in this work.

Rasmus Normann Wilken Eriksen. March 2014.

List of figures

List of tables

Appendix A High speed imaging for material testing

In high strain rate testing the test event may happen so fast that it is impossible to obtain any qualitative information about the material test by observing the test or recording the event with a standard camera at a standard frame rate (20-30fps). High-speed cameras can be employed to obtain qualitative information from the event by capturing images at several thousand images per second. The qualitative information can be used to assess the test in conjunction with load and strain data and look for failure mechanism etc. The images can be turned into quantitative information by using the images for Digital Image Correlation (DIC) and support or replace the deformation and strain measurements. DIC is a well-known non-contact measurement technique, which has been describe in great details in literature [100-102], further the use of high speed imagining and DIC has also been described be several authors [103-106].
High speed cameras can be divided into 3 distinct types of cameras, the rotating mirror multiple sensor camera, the single sensor and in situ storage single sensor cameras, but for DIC only the two latter are interesting as the rotating mirrors causes many problems for DIC algorithms [107]. Examples of state of the art single sensor cameras are given in Figure 9.1 along with their maximum frame rate at maximum resolution.

A) Photron SA Z. Single sensor camera. 1024x1024px at max 20000 FPS.

B) Specialised Imaging – Kirana single sensor in situ storage camera. 924x768px at max 5000000 FPS.

Figure 9.1 State of the art single sensor cameras

The main difference between the two types of cameras is that the single sensor camera will have reduced resolution at higher frame rate than the maximum frame rate at maximum resolution. The bottleneck is the data transfer rate from the sensor to the ring buffer memory. The single sensor in situ camera comes around the transfer bottleneck by having built in ring buffer memory in the sensor itself so the resolution can be kept high at even very high frame rates. The drawback is a limited ring buffer memory. The Kirana camera can only store 180 images in its sensor memory whereas the Photron SA Z can store several hundred thousand of images in its external RAM memory. For FRP materials where the strain to fracture is low the few images may be enough to cover the test event, however the triggering of the camera becomes challenging as For example the recording time for the Kirana is 36µs at 5000000FPS.
In a situation of selecting a high speed camera for both qualitative and quantities image capturing a lot of technical parameters must be selected as a compromise where the most important.

- Resolution
- Frame rate (FR)
- Recording time

- Magnification in px/mm (M)
- Field of view (FOV)
- Shutter time (SS)

Frame rate, resolution, recording time and shutter time are pure camera properties whereas FOV and M is a function of the physical setup with respect to the test subject.
The easiest parameter to select is the shutter time as is always should be minimised to minimise blur in the images and in most circumstances the shutter time must be less than 1/FR and not 1/FR which is the maximum shutter time. However the shutter time can be restricted by the available light sources and the expected blur for the setup should always be evaluated. The maximum blur in a scene can be calculated as a function of the maximum velocity (V) in the scene and the FOV and M as

$$mb = SS * V * M \tag{9.1}$$

For single sensor cameras the resolution is limited at higher frame rates due to the transfer bottleneck and this will also affect the magnification. For qualitative measurement a feature should be occupied by at least two pixels [108] but for materials test of especially FRP's at least 64 -128 pixels should cover the shortest distance of the FOC to get a minimum overview of the fracture process. The FOV is adjusted on the base of the resolution by the choice of lens and working distance (Distance between specimen and sensor) such that the entire specimen is within the FOV and covered by the required amount of pixels. The magnification is then the product of the selected/available resolution to the cover the specimen.
The recording length should be long enough to cover the entire deformation process and for single sensor cameras this is no problem as normally are equipped with several gigabyte of ring buffer memory, but attention must be paid to the recording length of single sensor in situ cameras. The duration of the specimen deformation can be estimated from the failure strain and the strain rate, but it must be taken into account that the strain rate is not constant during the test and in most circumstances are lower than predicted for the test setup.
For qualitative imaging there exist guidelines for selecting frame rates where For example simple statements as a minimum of 10 images must be capture of the event [108] and required frame rate can be calculated if the deformation duration is known. For quantitative measurement with the images set of guidelines for selecting frame rate and recording duration can be derived based on the properties of the accuracy of the non-contact measurement method. In many cases the selection for frame rate and recording length may also determine the type of camera. Any measurement method is limited by its noise floor For example how small a quantity can be measured which with a reasonable certainty can be regarded as not being noise from the measurement method itself. In a tensile test of a test specimen one end of the specimen will be clamped and the other will be moving and thus there will be a velocity field over the specimen range from zero velocity at the clamped end to maximum velocity at the moving end. The moving end will also experience the largest displacement meaning that in terms of displacement the signal and signal to noise ratio will be much larger at the moving end. Thus each end of the specimen will set different requirements for measurement method if displacement is used as base; however the strain field is uniform over the entire specimen and will have the same signal to noise ratio over the entire specimen. The noise floor in DIC strain measurements is determined by a long range of parameters, which to some degree can be controlled in the lab, however in the end the noise floor will have a certain level and this level can be used to determine a set of requirement for the high speed cameras used to capture images for DIC. For the commercial DIC system Aramis the general strain resolution (ε_{RES}) is about 0.01% for a good setup. If the fracture strain (ε_f) in a UD loading situation of a material is known then recording length in frames which covers the deformation event can be determined. The strain change from frame to frame should not be less than the noise floor else the

event is oversampled. Thus the feasible number of images (NoI) becomes

$$NoI = \frac{\varepsilon_f}{\varepsilon_{RES}} \tag{9.2}$$

The number of images is plotted in Figure 9.2as function of the failure strain for different DIC noise floor levels. The time to fracture (T) for an average strain rate $\dot{\varepsilon}$ yields

$$T = \frac{\varepsilon_f}{\dot{\varepsilon}} \tag{9.3}$$

The required frame rate to obtain a feasible number of images up too fracture then becomes

$$fps = \frac{NoI}{T} = \frac{\varepsilon_f}{\varepsilon_{RES}} \frac{\dot{\varepsilon}}{\varepsilon_f} = \frac{\dot{\varepsilon}}{\varepsilon_{RES}} \tag{9.4}$$

The required frame rate is then only a function of the DIC noise floor. Thus the camera frame rate and camera recording length can be selected as function of the inter frame strain increment which should be set to or higher than the DIC noise floor. It should be noted that a higher resolution will allow the user to use a higher facet size and step size without scarifying spatial resolution and a reduced noise floor can be achieved. Thus the inter frame strain increment can be chosen to a lower value and the effect is that high resolution camera will require higher frame rate and recording length. Figure 9.2 shows graphs for selecting recording length and frame rate as function of average strain rate and resolution of the DIC measurements. An example of selection could be than a material with a technical fracture strain of 3% should be tested at an average strain rate of 1000 /s with DIC resolution/inter frame strain increment of 0.02%. This would call for a recording length of about 150 images and a frame rate of about 5e6 fps. There should be left room enough for a lower strain rate with respect to the recording length so the experimenter ensures that there are captured images for the entire deformation process. This selection also indicates that the single sensor camera have more than enough memory capacity, but they will lack frame rate (and resolution). The single sensor in situ cameras will have sufficient frame rate but only suitable for FRP testing with very accurate triggering.

The last but also in many cases the most important parameter is the price. In many cases the experimenter cannot just select a camera with the correct specifications, but must use what is available. These guidelines can be used backward to estimate the strain increment per frame from a frame rate and recording length.

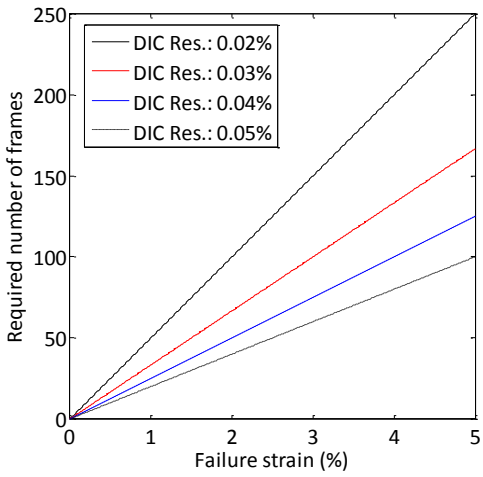

A) Minimum feasible number of images for different failure strain and DIC noise floor

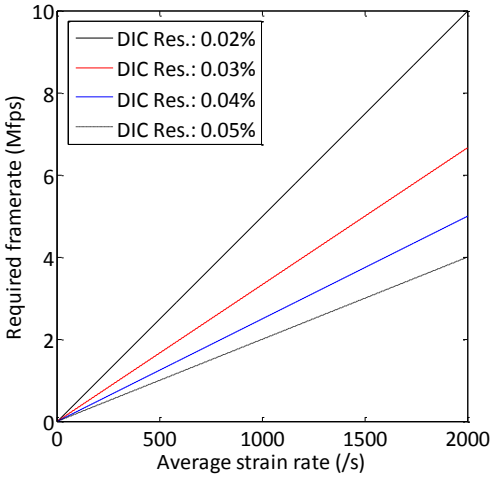

B) Required frame rate as function of the average strain rate over the specimen.

Figure 9.2 Recording length and frame rate as function of the DIC noise floor. The DIC noise floor can also be seen as a selected average strain increment over the specimen between each image. The user can select that there should be x% strain increase between each image and this will set up the requirement for the camera.

Appendix B Useful conversion 1D wave theory

- σ_I is the incident stress pulse
- σ_R is the reflected stress pulse
- σ_T is the transmitted stress pulse

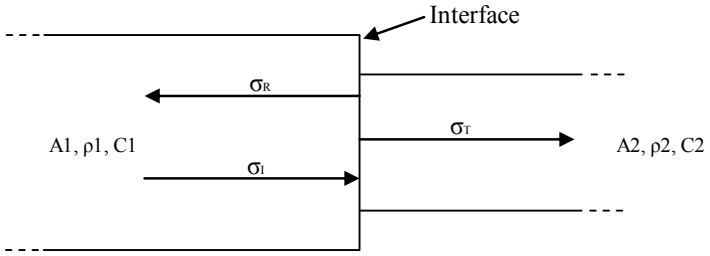

Figure 9.3 Interface between two slender bars

The transmission and reflection coefficients can be calculated from equation (9.5) and (9.6) and the equations are plotted in Figure 9.4.

$$\frac{\sigma_T}{\sigma_I} = \frac{2A_1\rho_2C_2}{A_1\rho_1C_1 + A_2\rho_2C_2} \tag{9.5}$$

$$\frac{\sigma_R}{\sigma_I} = \frac{A_1\rho_1C_1 - A_2\rho_2C_2}{A_2\rho_2C_2 + A_1\rho_1C_1} \tag{9.6}$$

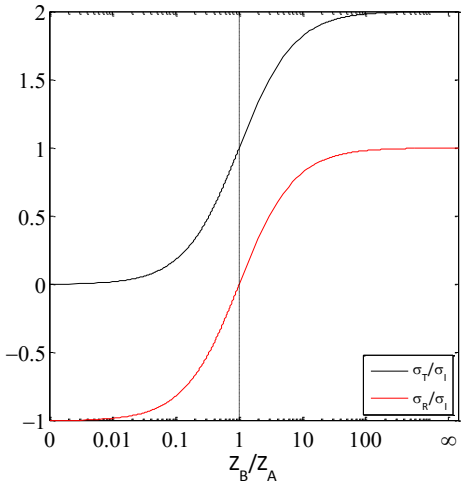

A) Variation of the mechanical impedance

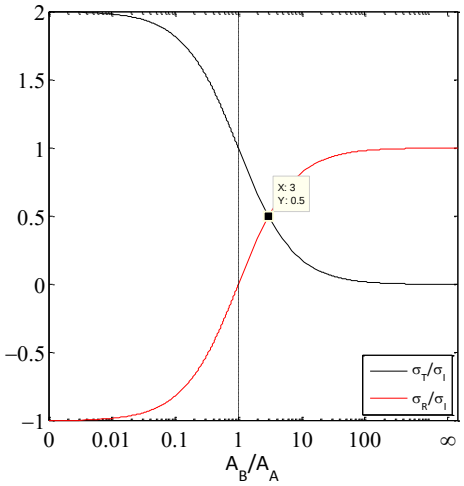

B) Variation of the cross sectional area when the $Z_A=Z_B$

Figure 9.4 Reflection and transmission coefficients as functions the relative mechanical impedance and the relative cross sectional area.

Appendix C Simulation of choked flow

A relationship P(x,t) is sough for compressible air where P is the pressure in an air chamber and x is the displacement of a piston rod which changes the volume of the air chamber. T is time of the process. The air chamber is ventilated and air will escape from the chamber as P changes. The situation is sketched in Figure 9.5 where the pistonrod initial is in rest and then moves forward with velocity *v*. The pressure in the air chamber is P1 and the ambient pressure is P2 while the volume of the chamber is V.

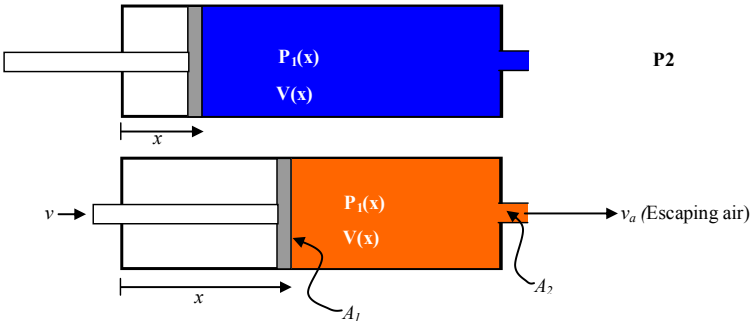

Figure 9.5 Sketch of cylinder with a piston which moves forward at a velocity v. As the piston moves forward the air is compressed and forced out of the opening.

The initial state of the air in the cylinder is given by the ideal gas equation for x = 0

$$P_1 V = nRT \tag{9.7}$$

With n as the amount of mol air calculated from air mass (m) and the molar mass (M)

$$n = \frac{m}{M} \tag{9.8}$$

R is the gas constant and T is air temperature. As the piston rod moves forward the air will be compressed and escape out of any available holes. The discharge rate of mass/s which leaves the cylinder with constant velocity and density can be calculated from [109]

$$\dot{m} = \rho v_a A \tag{9.9}$$

However the escape velocity depends on the pressure ratio P_2/P_1 and the density of the air. When $P_2/P_1 < 0.528$ the air has reached sonic velocity at the outlet and the air velocity cannot be increased further; However the density of the escaping air will increase at this condition with increasing P1 and the mass rate will increase without an increase in air velocity. This condition is called a "choked flow" as the air velocity is choked. The choked condition is obtained at a pressure ratio $P2/P_1 = 0.528$. The hole(s) in the air chamber can be assumed to behave as an orifice and assuming an adiabatic compression of the air, the instantaneous mass discharge rate for an orifice can be calculated from

$$\dot{m} = A\sqrt{2P_1\rho_0\left(\frac{\gamma}{\gamma+1}\right)\left[\left(\frac{P_2}{P_1}\right)^{\frac{2}{\gamma}} - \left(\frac{P_2}{P_1}\right)^{\frac{\gamma+1}{\gamma}}\right]} \tag{9.10}$$

ρ_0 is the air density at initial pressure before the process is started and λ is the heat capacity ratio of air. The instantaneous mass discharge rate for the orifice choked condition is calculated from

$$\dot{m} = A\sqrt{\gamma P_1\rho_0\left(\frac{2}{\gamma+1}\right)^{\frac{\gamma+1}{\gamma-1}}} \tag{9.11}$$

In the case the where air is flowing *out* of the chamber the pressure ratio P_2/P_1 will always be less than 1, however a condition with a $P_2/P_1<1$ can be obtained in two ways. The first way is by maintaining the ambient pressure P_2 while P_1 is increased. This corresponds to a compression of the air in the cylinder with constant ambient pressure. The second way is to maintain P_1 and lower P_2 towards vacuum. These two conditions create very different variation in the mass flow rate with the pressure ratio as the choked flow only depends on P_1. Figure 9.6 shows the two conditions;

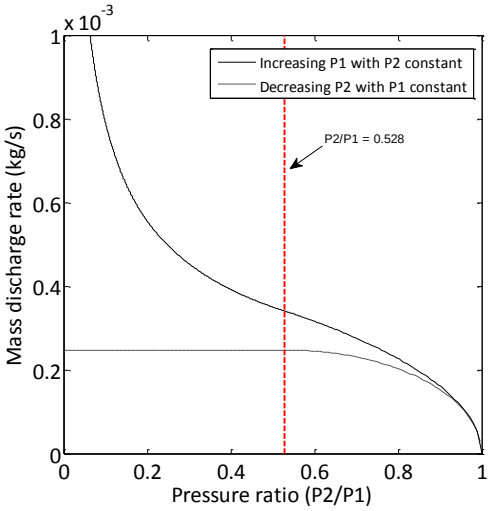

Figure 9.6Mass discharge rate calculated from equation (9.9) and (9.10) respectivily as function of the pressure ratio. Increasing P1 with P2 constant is the situation with the cylinder compression the air. Decreasing P2 with P1 constant is the situation where the ambient pressure is lowered and the cylinder pressure is kept constant.

The condition with P_2 going towards vacuum will reach stagnation in the mass flow in the choked condition whereas the condition with increasing P_1 will have continuous and accelerating mass flow as the pressure ratio is lowered.

A slack adapter placed in lab conditions corresponds to the condition with increasing P_1 as the slack adapter moves and P_2 is the constant as the volume in the lab is so big that the air mass forced out of the slack adapter will not affect the pressure in the lab.

The relationship $P_1(x)$ is established by consider the changing volume of the chamber with x. If the air in the chamber and surroundings are at the same pressure there will be no net flow in and out of the chamber and the initial mass of air can be calculated from

$$m_i = \frac{P_i V_i M}{RT} \tag{9.12}$$

As the piston moves forward the volume the air can occupy is decreased and P_1 will increase as P and V are inversely proportional according to

$$P = \frac{mRT}{MV} \tag{9.13}$$

However at the moment P_1 increases there will be a net flow of air out of the chamber and the flow is calculated from either equation (9.10) and (9.11) dependent on the pressure ratio P_2/P_1 so the chamber pressure cannot solely be calculated from equation (9.7) as the air mass is not constant. Since the air mass and pressure is related to each other, the chamber pressure must be solved in an iterative way. The algorithm for solving P(x,t) is

- Step 0: Calculate initial air mass from equation (9.12) for t = 0 and x = 0.
- Step 1: Increment t (dt) and x (dx) according to the velocity profile of the piston rod and calculate the new volume V.
- Step 2: Calculate a new pressure P_1 from equation (9.13) assuming no change in air mass
- Step 3: Calculate the pressure ratio P_2/P_1 and calculate the mass flow rate from either equation (9.10) or (9.11) dependent if P_2/P_1 is higher or lower than 0.528.
- Step 4: Update the air mass with $m = m - \dot{m}dt$
- Step 5: Update the pressure P_1 from equation (9.13) with the update mass.

Step 1 to 5 is repeated until the piston rod is at rest. It is an underlying assumption that $\dot{m}$ is constant during dx and dt.
Figure 9.7A shows the effect of varying the increment size for the x while the time increment is adjusted so the velocity is constant and the same for all three increments. The increment should be kept down at around 1mm to maintain a smooth approximation. Figure 9.7B shows comparison for the pressure development for a constant piston rod velocity and a linear rising velocity up to that of the constant velocity. The pressure build up with x is higher for the high velocity and the constant velocity gives higher pressure than the corresponding linear rising velocity. This is due to the faster decreased volume compared to the mass flow out of the chamber. A2 smaller outlet area will also result in a faster pressure build, which is seen, directly from equation (9.10) and. (9.11) where the mass flow rate is proportional to the outlet area A2. This developed algorithm can be used to simulate the force from inclusion of air in a slack adapter and investigate the effect of this. The algorithm establish and relationship between the pressure in the air chamber and the time and displacement increments of the piston rod.

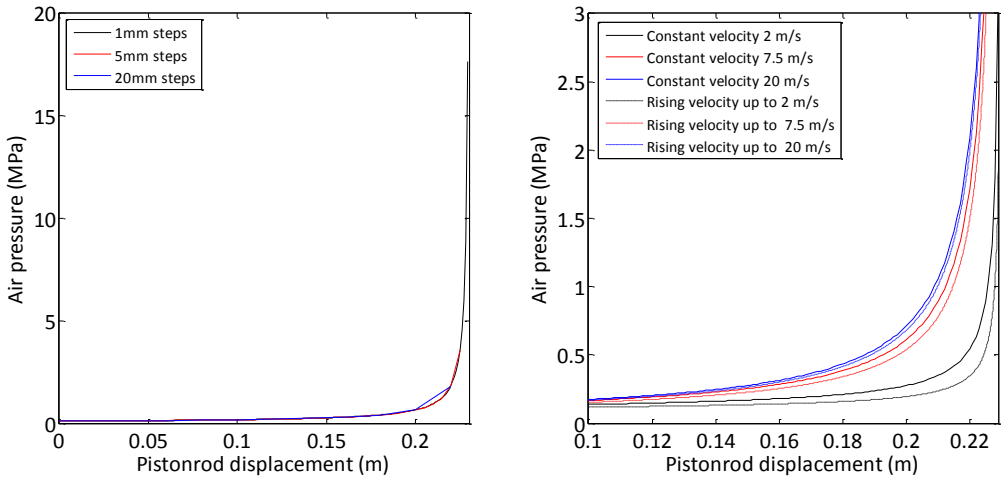

A) Effect of increment in x for constant and equal velocity of the piston rod for all increments sizes.

B) Comparison of constant and linear rising velocity of the piston rod.

*Figure 9.7 Simulations with A1 = 1283mm2, A2 = 18.6mm2, λ=1.4 (Air), M = 0.029kg/mol, R 8.315 j/mol*k, T = 293K (Assuming constant temperature), Chamber length = 0.23m.*

Appendix D MatLab model for elasto plastic material

A model of a simple elasto plastic material is presented here. An elasto plastic material will deload in a non-reversible manner and this has to be represented in the material law. A simple power hardening law is used here for representing an elasto plastic material. The law is given in equation (9.14)

$$Fs = A_s \sigma_y \left(\frac{\varepsilon}{\varepsilon_y}\right)^n \tag{9.14}$$

The non-reversible model is given in Figure 9.9 and the output from the model is given in Figure 9.9. The model which simulates the load train of the high strain rate test machine will make an increment in time, then calculate a new set of displacement and velocities from the previous known acceleration. The acceleration is then updated from the force function which will be evaluated with the new increments in time, displacement and velocity. This is done for each time step until a certain threshold error has been reached. It means strain will be prescribed to the model as function of time and thus this non-reversible material law must work with prescribed strain steps and return the force for each strain increment.

```
% Specimen data
E = 200e9;          % Elastic modulus
L = 1;              % Length
A = 0.003*0.025;    % Cross sectional area (mm)
n = 0.1;            % Hardeing exponent
Sigy    = 400e6;    % Yield strength
% Algoritm variables
Trig1    = 0;               % if yielding have occured
Trig2    = 0;               % if Yield surface has been updated
ZeroC    = 0;               %  Plastic strain
SigMax  = Sigy;
% Deformation vector
dL = (0:0.00001:0.01);
dL = dL+0.00050*sin(6000*dL);
% Direction of next loading step
Dir(1:2) = (dL(2)>0);
% Begin main loop
for i = 2:1000
    epsNom(i) = dL(i)/L;              % Calculate nominal strain of next load step
    if (dL(i)-dL(i-1))>0              % Check for loading direction
        Dir(i) = 1;
    else
        Dir(i) = 0;
    end
    if Dir(i) ~= Dir(i-1);            % Loading direction have changed.
        if Trig1 == 1 && Trig2 == 0;  % Update yield condtions if yield (Trig1) was↙
happening before unloading
            Trig2     = 1;            % Signal that new yield conditions has been↙
updated - avoind reentry
            Trig1     = 0;            % Signal that yielding is not occuring anymore↙
(Don't opdate yield conditions anymore)
            ZeroC     = epsNom(i-1)-SigMax/E;
        end
    end
    if ((epsNom(i)-ZeroC)*E) > SigMax                 % yielding
        SigMax = Sigy*(E*abs(epsNom(i))/(Sigy))^n;    % New Force from continious↙
loading is new sigmax
        F(i)   = SigMax*A;
        Trig1  = 1;                                   % Signal yielding
        Trig2  = 0;                                   % reset unloading trigger
    else  % Elastic
        F(i) = A*E*(epsNom(i)-ZeroC);
    end
end
```

Figure 9.8 Non-reversible model to simulate a elasto-plastic material during a loading profile with unloading stages.

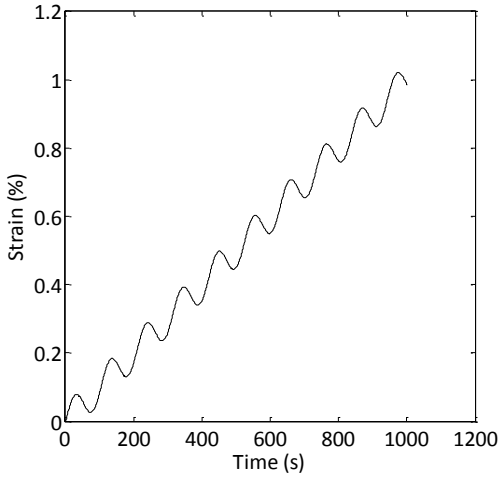

A) Strain profile given to the material model. Notice the unloading parts.

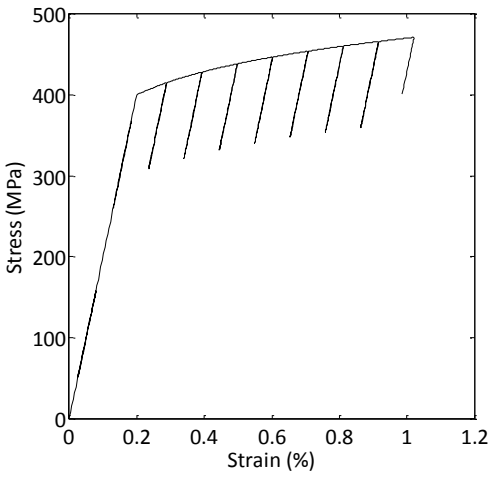

B) Stress strain curve from the model. The "dips" are the unloading stages corresponding to the unloading part shown in A.

Figure 9.9 Strain profile and stress strain curve of the non-reversible material model.

Appendix E Strain gage amplifier

The most demanding case for the strain gage amplifier is the quarter bridge setup (Wheatstone bridge) which provide the least amount of output signal to the amplifier. The output voltage "e" of a quarter bridge setup with amplification "Amp", gage factor "K", supply voltage E and a applied strain ε is given as [110]

$$e = Amp\frac{1}{4}KE\varepsilon \tag{9.15}$$

Especially for polymer composite materials the supply voltage must be kept low to minimise local heating of the specimen when the amplifier is connected before testing the specimen. Due to the transient nature of the test, the effect of heating the specimen during is the test can be neglected, especially for metallic materials as they will suffer from a very high internal heating during the straining of the specimen. For polymer composites the supply voltage should be kept at around 2 volt [111] and this value is used as reference for the next calculations. Exchanging ε with $\dot{\varepsilon}$ in equation (9.15) will yield

$$\dot{e} = Amp\frac{1}{4}KE\dot{\varepsilon} \tag{9.16}$$

the output rate of the quarter bridge setup and shows there is a linear dependency between the strain rate imposed to the strain gage and the output rate of the system. The only unknown factor is the amplification. To maximise the resolution a strain signal should always be amplified to the maximum limit of the DAQ system. In many cases this is ±10 volt. This is used as a reference value. The required amplification will then depend on the maximum strain to measure and the amplification is calculated from

$$Amp = \frac{4e}{EK\varepsilon_{max}} \tag{9.17}$$

This relationship is shown in Figure 9.10A where a maximum strain of 1% will require a amplification of 1000, 5% will required 200 and 10% maximum strain will require 100 in amplification. The output rate is shown as function of strain rate in Figure 9.10B.

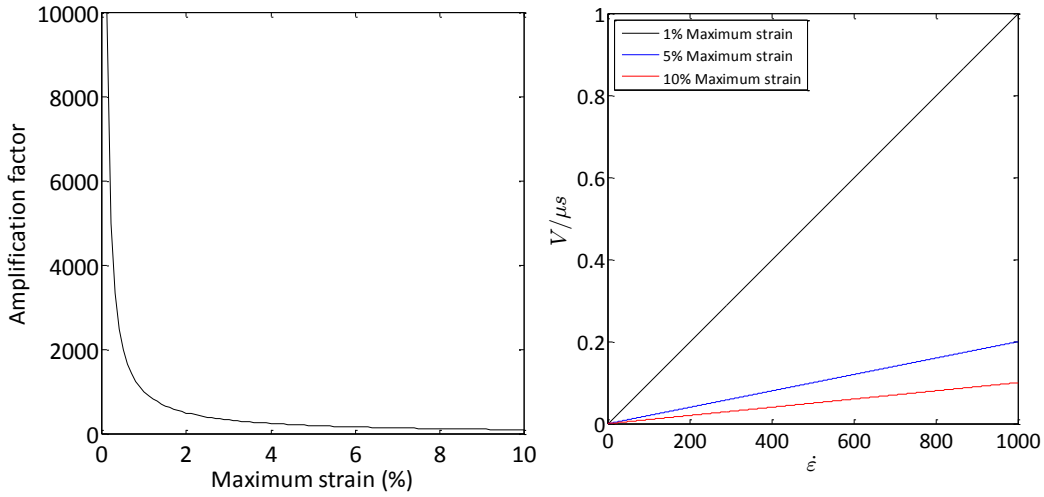

A) Amplification factor as function of maximum strain to measure. Max output voltage e= 10V. Max supply voltage E=2V. Gage factor K = 2.

B) Output rate as function of the strain rate imposed to the system. The selected amplifier must have a slewrate which is above the curves to avoid any damping of the amplified signal

Figure 9.10 Selection curves for high strain rate strain gage amplifiers.

Appendix F Parameters for simulations in Chapter 2

```
%% -- Model parameters for classical slack adapter system

% -- Areas
K.Ap  = 4778/1e6;       % Pistonrod cross sectional area (m2)
K.Ar  = 1200/1e6;       % Pressure area of the rubber damper (m2)
K.As  = 5*15/1e6;       % Slackadapter crosssectional area (m2)
K.Asp = 1*15/1e6;       % Specimen crosssectional area (m2)

% -- Masses
K.M1  = 1.83;           % Mass at node 1
K.M2  = 1.83+0.64;      % Mass at node 2
K.M3  = 0.64+0.104;     % Mass at node 3
K.M4  = 33;             % Mass at node 4 Piston rod

% -- Lengths
K.Lr  = 0.003;          % Rubber damper thickness (m)
K.Ls  = 0.15;           % Slackadapter length (m)
K.Lsp = 0.05;           % Specimen free length (m)
K.Li  = 0.180;          % Free acceleration length in slack adapter
% -- Stiffness
K.Es   = 42e9;          % Slackadapter stiffness (Pa)
K.Klc  = 26e9;          % Loadcell stiffness (N/m)
K.Esp  = 42e9;          % Specimen stiffness (Pa)

% -- Other material constants
K.Vi     = 0;           % Initial velocity of node 1 (m/s)
K.Vn     = 20;          % Rated velocity
K.Pn     = 270*1e5;     % Pressure drop at initial velocity (Pa)
K.C1     = 50e6/2;      % Rubber material constant neo Hookian law (Pa)
K.EpsF   = 0.025;       % Failure strain of specimen
K.SigY   = 800e6;       % Yield stress
K.Epsy   = K.SigY/K.Esp; % Yield strain
K.n      = 0.1;         % Work hardening exponent
K.Steel  = 0;           % Type of specimen 0 = Linear elastic, 1 = Elastic plastic
```

References

1. High Strain Rate Experts Group Recommendations for Dynamic Tensile Testing of Sheet Steels. International Iron and Steel Institute(2005)

2. Carlsson LA, Adams DF, Pipes RB *Experimental characterization of advanced composite materials*. CRC press(2002)

3. Meyers MA *Dynamic behavior of Materials*. John Wiley & Sons, Inc.(1994)

4. Sierakowski RL . *Appl Mech Rev* 50:741-761(1997)

5. Jacob GC, Starbuck JM, Fellers JF, Simunovic S, Boeman RG . *J Appl Polym Sci* 94:296-301(2004)

6. Barré S, Chotard T, Benzeggagh ML . Composites Part A: Applied Science and Manufacturing **27**:1169-1181(1996)

7. Wood PKC, Burkley M Strain Rate Testing of Metallic Materials and their Modelling for use in CAE based Automotive Crash Simulation Tools (Recommendations & Procedures). Warwick University(2008)

8. ISO ISO 26203-1 Metallic Materials - Tensile testing at high strain rates - Part 1: Elastic-bar-type systems (ISO 26203-1:2010). ISO(2010)

9. ISO ISO 26203-2 Metallic Materials - Tensile Testing method at high strain rates - Part2: Servo-Hydraulic and other test systems, 2nd edn. ISO(2011)

10. P. K. C. Wood, C. A. Schley, M. Buckley, J. Smith. (2007)

11. Adrian Riddick (2001)

12. Bardenheider R, Rogers G Dynamic Impact Testing. Instron(2003)

13. R. Bardenheier, G. Rogers . J Phys IV:693(2006)

14. Hamouda AMS, Hashmi MSJ . J Mater Process Technol **77**:327-336(1998)

15. A.R. Bunsell, J. Renard *Fundementals of fibre reinforced composite materials*. IoP(2005)

16. Karl F. Graff *Wave motion in elastic solids*. Dover Publications(1975)

17. Song B, Chen W . Exp Mech **44**:300-312(2004)

18. Chen W, Song B *Split Hopkinson (Kolsky) Bar*. Springer(2011)

19. Yang LM, Shim VPW . Int J Impact Eng **31**:129-150(2005)

20. Frew D, Forrestal M, Chen W . Exp Mech **41**:40-46(2001)

21. Frew D, Forrestal M, Chen W . Exp Mech **42**:93-106(2002)

22. Ravichandran G, Subhash G . J Am Ceram Soc **77**:263-267(1994)

23. Granta Design Limited 5.2.0(2009)

24. Hosur MV, Alexander J, Vaidya UK, Jeelani S . Composite Structures **52**:405-417(2001)

25. Harding J, Welsh LM . J Mater Sci **18**:1810-1826(1983)

26. Eskandari H, Nemes JA . Journal of Composite Materials **34**:260-273(2000)

27. Welsh L, M., Harding J . J.Phys.Colloques **46**:C5-405; C5-414(1985)

28. Wang W, Makarov G, Shenoi RA . Composite Structures **69**:45-54(2005)

29. Zhou Y, Wang Y, Xia Y, Jeelani S . Mater Lett **64**:246-248(2010)

30. Sun B, Liu F, Gu B . Composites Part A: Applied Science and Manufacturing **36**:1477-1485(2005)

31. Chocron Benloulo IS, Rodríguez J, Martínez MA, Sánchez Gálvez V . Int J Impact Eng **19**:135-146(1997)

32. Languerand DL, Zhang H, Murthy NS, Ramesh KT, Sansoz F . Materials Science and Engineering: A **500**:216-224(2009)

33. Koh ACP, Shim VPW, Tan VBC . Int J Impact Eng **37**:324-332(2010)

34. Koh CP, Shim VPW, Tan VBC, Tan BL . Int J Impact Eng **35**:559-568(2008)

35. Tan VBC, Zeng XS, Shim VPW . Int J Impact Eng **35**:1303-1313(2008)

36. Harding J . Composites **24**:323-332(1993)

37. Armenàkas A, Sciammarella C . Exp Mech **13**:433-440; 440(1973)

38. Pardo S, Baptiste D, Décobert F, Fitoussi J, Joannic R . *Composites Sci Technol* 62:579-584(2002)

39. Naik NK, Yernamma P, Thoram NM, Gadipatri R, Kavala VR . Polym Test **29**:14-22(2010)

40. Brown KA, Brooks R, Warrior NA . Composites Sci Technol **70**:272-283(2010)

41. Guden M, Yildirim U, Hall IW . Polym Test **23**:719-725(2004)

42. Akil Ö, Yıldırım U, Güden M, Hall IW . Polym Test **22**:883-887(2003)

43. Eriksen R High speed characterization of composite materials. Master Thesis. Department of Mechanical Engineering, Technical University of Denmark(2010)

44. SAE Standard: J2749 High Strain rate Tensile Testing of PolymersSAE (ed) . SAE(2008)

45. Fitoussi J, Meraghni F, Jendli Z, Hug G, Baptiste D . Composites Science and Technology **65**:2174-2188(2005)

46. Othman R, Guégan P, Challita G, Pasco F, LeBreton D . Int J Impact Eng **36**:460-467(2009)

47. Schoßig M, Bierögel C, Grellmann W, Mecklenburg T . Polymer Testing **27**:893-900(2008)

48. Ochola RO, Marcus K, Nurick GN, Franz T . Composite Structures **63**:455-467(2004)

49. Shokrieh MM, Omidi MJ . Composite Structures **88**:595-601(2009)

50. Moog Inc. D660 Series. Servo-Proportional Control Valves with Integrated Electronics, ISO 4401 Size 05 to 10

51. J.R. Davis *Tensile Testing*. ASTM International(2004)

52. Boyce BL, Dilmore MF . Int J Impact Eng **36**:263-271(2009)

53. Wood P, K.C., Schley C, A., Williams M, Beaumont R, Rusinek A, Mayer U, Pearce A **1**:265-273(2009)

54. Bleck W, Schael I . *Steel Res* 71:173-178(2000)

55. Xiao X . Polymer Testing **27**:164-178(2008)

56. ASTM D3039 Standard test method for Tensile properties of polymer Matrix composite Materials(2008)

57. Fitoussi J, Bocquet M, Meraghni F . Composites Part B: Engineering **45**:1181-1191(2013)

58. Rasmussen PW *Hydraulik ståbi*. Teknisk forlag(1996)

59. Danish Standard DS 412 Code of Practice for the structural use of steel(1999)

60. Kistler Load Washer. In: . http://www.kistler.com/gb_en-gb/13_Productfinder/App.9071A.5/Quartz-Load-Washers-0-...-400-kN.html. Accessed 05/22/09

61. Wang S-, Parvizi-Majidi A . J Mater Sci **27**:5483-5496(1992)

62. Toftegaard H Low strain rate material characterization ofE-glass/LPET(2012)

63. Toftegaard H Low strain rate material characterization of E-glass/epoxy(2012)

64. Toftegaard H, Lystrup A Mechanical properties of C/PA6 UD lamina. Risø DTU(2007)

65. Knudsen H, Comfil D08B - Manufacturing of thermoplastic panels for 1. Round(2011)

66. Hopkinson B . Proceedings of the Royal Society of London.Series A **89**:411-413(1914)

67. Davies RM . Philosophical Transactions of the Royal Society of London.Series A, Mathematical and Physical Sciences **240**:pp. 375-457(1948)

68. Kolsky H . *Proceedings of the Physical Society.Section B* 62:676(1949)

69. Bo Song, Weinong Chen . Latin America Journal of Solids and Structures **2**(2005)

70. Pan Y, Chen W, Song B . Exp Mech **45**:440-446(2005)

71. George T. (Rusty) Gray III (2003) Classic Split-Hopkinson Pressure Bar. In: ASM Handbook, Vol 8, Mechanical testing and Evaluation. ASM International

72. Follansbee PS, Frantz C . J Eng Mater Technol **105**:61-66(1983)

73. Zhang QB, Zhao J . Rock Mech Rock Eng:1-68(2013)

74. Nemat-Nasser S, Isaacs JB, Starrett JE . Proceedings of the Royal Society of London Series A: Mathematical and Physical Sciences **435**:371-391(1991)

75. Koerber H, Camanho PP . Composites Part A: Applied Science and Manufacturing **42**:462-470(2011)

76. Gary G, Mohr D . Exp Mech **53**:713-717(2013)

77. Mohr D, Gary G, Lundberg B . Int J Impact Eng **37**:161-169(2010)

78. Christensen RJ, Swanson SR, Brown WS . Exp Mech **12**:508-513(1972)

79. Baranowski P., Malachowski J., Gieleta R., Damaziak K., Mazurkiewicz L., Kolodziejczyk D. . *Bulletin of the Polish Academy of Sciences: Technical Sciences* 61:459(2013)

80. S Ellwood and L J Griffiths and,D.J.Parry . Journal of Physics E: Scientific Instruments **15**:280(1982)

81. Gerlach R, Sathianathan SK, Siviour C, Petrinic N . Int J Impact Eng **38**:976-980(2011)

82. Song B, Syn C, Grupido C, Chen W, Lu W- . Exp Mech **48**:809-815; 815(2008)

83. Song B, Chen W . Exp Mech **44**:622-627(2004)

84. Koerber H, Xavier J, Camanho PP . Mech Mater **42**:1004-1019(2010)

85. Nishida EE, Foster JT, Briseno PE . Journal of Composite Materials(2012)

86. Naghdabadi R, Ashrafi MJ, Arghavani J . Materials Science and Engineering: A **539**:285-293(2012)

87. Davies EDH, Hunter SC . J Mech Phys Solids **11**:155-179(1963)

88. Follansbee PS (1985) The Hopkinson Bar. In:
Metals handbook, (1985) , vol. 8 edn. American Society for Metals, Metals Park, OH, pp 198

89. Lifshitz JM, Leber H . Int J Impact Eng **15**:723-733(1994)

90. Gama BA, Lopatnikov SL, Gillespie JW, Jr . Appl Mech Rev **57**:223-250(2004)

91. Kaiser AM Thesis: Advancements in the Split Hopkinson Bar Test. Faculty of the Virginia Polytechnic Institute(1998)

92. Tyas A, Watson AJ . Int J Impact Eng **25**:87-101(2001)

93. D.J. Parry, P.R. Dixon, S. Hodson, N. Al-Maliky . Journal De Physique **C8**:107(1994)

94. Foster J . Exp Mech **52**:1559-1563(2012)

95. Chen W, Zhang B, Forrestal M . Exp Mech **39**:81-85; 85(1999)

96. Nemat-Nasser S (2000) Introduction to high strain rate testing, ASM Handbooks; Volume 8: Mechanical testing and Evaluation. In: . ASM Int.

97. George T. (Rusty) Gray III (2002)

98. Forrestal MJ, Wright TW, Chen W . Int J Impact Eng **34**:405-411(2007)

99. GOM Optical Measuring Techniques . In: . http://www.gom.com/metrology-systems/digital-image-correlation.html. Accessed 11/25 2010

100. Orteu J . Optics and Lasers in Engineering **47**:282-291(2009)

101. M. A. Sutton *Image Corrolation for Shape, Motion and Deformation Measurements Basic Concepts, Theory and Applications*. Springer(2009)

102. Chu TC, Ranson WF, Sutton MA . Exp Mech **25**:232-244(1985)

103. Schmidt T, Tyson J, Galanulis K, Revilock D, Matthew M *26th International Congress on High-Speed Photography and Photonics* **5580**:174-185(2004)

104. Tiwari V, Sutton MA, McNeill SR . *Exp Mech* 47:561-579(2007)

105. Siebert T, Becker T, Spiltthof K, Neumann I, Krupka R . Opt Eng **46**:051004(2007)

106. Kirugulige MS, Tippur HV, Denney TS . *Appl Opt* 46:5083-5096(2007)

107. P. L. Reu, T. J. Miller . Journal of Strain Analysis **43**:673(2008)

108. Photron (2008) How to Choose a high speed camera. In: . PHOTRON. http://www.photron.com/content.cfm?n=articles&prodid=2 2009

109. Robert W. Fox (2004) Introduction compressible flow. In: Introduction to Fluid Mechanics, 6th edn. Wiley, pp 594

110. Hoffmann K *An introduction to Measurements using Strain Gages*. Hottinger Baldwin Messtechnik GmbH, Darmstadt(1989)

111. Vishay TN-502 (2007)

DTU Mechanical Engineering
Section of Solid Mechanics
Technical University of Denmark

Nils Koppels Allé, Bld. 404
DK- 2800 Kgs. Lyngby
Denmark
Phone (+45) 4525 4250
Fax (+45) 4593 1475
www.mek.dtu.dk

DCAMM
Danish Center for Applied Mathematics and Mechanics

Nils Koppels Allé, Bld. 404
DK-2800 Kgs. Lyngby
Denmark
Phone (+45) 4525 4250
Fax (+45) 4593 1475
www.dcamm.dk
ISSN: 0903-1685